Studies on Characterization of

Interfacial Properties of Lipid Bilayer Membranes and

Its Application to Their Surface Design

for Cooperative Molecular Interaction

Nozomi Watanabe

MARCH 2019

Studies on Characterization of

Interfacial Properties of Lipid Bilayer Membranes and

Its Application to Their Surface Design

for Cooperative Molecular Interaction

A dissertation submitted to

THE GRADUATE SCHOOL OF ENGINEERING SCIENCE

OSAKA UNIVERSITY

in partial fulfillment of the requirements for the degree of

DOCTOR OF PHILOSOPHY IN ENGINEERING

BY

Nozomi Watanabe

MARCH 2019

PREFACE

This dissertation work was conducted under the supervision of Professor Hiroshi Umakoshi at Division of Chemical Engineering, Graduate School of Engineering Science, Osaka University from 2014 to 2019.

The objective of this thesis is to clarify the mechanism of the molecular interaction that could be cooperatively induced at the lipid membrane. Especially, from the aspects of the cooperative molecular interactions at the membrane surface, the solvatochromic properties of the lipid membrane and the configurations of membrane-constituting molecules were studied by employing the nucleic acids as a model biomacromolecule. Furthermore, the specificity of the interaction created by the self-assembled structure were investigated.

The author hopes that this research would contribute to the design of the lipid membrane for its application to the cooperative interaction of biomacromolecules. The insight obtained in this study is expected to contribute to the regulation of the adsorption phenomena at the hydrophobic-hydrophilic interface.

Nozomi Watanabe

Division of Chemical Engineering
Graduate School of Engineering Science
Osaka University
Toyonaka, Osaka, 560-8531, Japan

Abstract

Functional biomacromolecules are known to form supramolecular assemblies via noncovalent bonds, implying the advantage of the designed surface of the local biointerfaces. Particularly, the surface hydration property plays an essential role to control their functions, while the characterization methodologies have not been established so much. Herein, the cooperative molecular interaction behaviors at the lipid membrane were studied.

In Chapter 1, the functions of lipid membranes were introduced as the representative of the hydrophilic/hydrophobic interface. Studies relating on the hydration at the membrane surface were summarized to investigate key factors working on the intermolecular interaction, and also to find the tips for the design of the membrane platform for interaction on its surface.

In Chapter 2, the local solvent environment at the membrane interface was evaluated using the solvent sensitive fluorescent probe, Laurdan. Based on the solvent model studied in the mixed solvent system, the emission spectra of Laurdan were classified into several components such as nonpolar, polar aprotic, and polar protic solvents. Multiple-components deconvolution analysis was proposed for the qualitative evaluation of local solvent environments.

In Chapter 3, the effect of dynamic and static hydration behaviors around the membrane interface was investigated based on the time-resolved fluorescence spectra of Laurdan. According to the assumption that the dynamic interaction of solvent molecules would lead the fluorescence lifetime shorter, the fluorescence quenching model was established. The static water molecules were assigned to the corresponding relaxation states of the fluorophore. Considering both effects, the number of hydrating water molecules per a lipid molecule was calculated. Obtained results revealed the consistency with the membrane phase transition and phase segregation.

In Chapter 4, the guanidinium-modified membrane was designed aiming for the enhancement of intermolecular interaction by the dehydration of membrane interface. Membranes modified with saturated guanidinium molecules (SG) revealed hydrophobic and ordered properties. On the other hand, lipid membrane modified with zwitterionic guanidinium molecules (MA) showed hydrophilic and disordered properties. SG modified membranes exhibited high affinity with tRNA, a model binding molecules, suggesting the effective design of the guanidinium modification.

In Chapter 5, the adsorption behaviors of nucleic acids at the lipid membrane were systematically studied. Emission spectra of Laurdan showed a dehydration behavior upon a model system of "*strong interaction*", while no dehydration behavior upon a model system of "*weak interaction*". From the analysis of isothermal titration calorimetry, the "*weak interaction*" system showed a molecular selectivity toward poly dC. According to the enthalpy-entropy compensation, the entropy-driven process was indicated in the "*strong interaction*", and the molecular selectivity was expected in the ideal contribution of enthalpy and entropy in the "*weak interaction*" system.

In Chapter 6, the cooperative effects on the configuration of guanidinium-modified lipid membrane and tRNA were investigated. The high affinity of POPC/SG vesicles with tRNA was confirmed by the analysis of apparent surface pK_a, indicating that the inter-lipid interactions of guanidinium support the orientation of lipid head groups, resulting in the acquisition of cationic membrane surface which is necessary for the interaction. The guanidinium modification lead the membrane in dehydrated and ordered states, and the membrane affected nucleobase-specific melting behaviors of tRNA during the membrane phase transition.

In Chapter 7, as a general conclusion of this work, the interaction behaviors induced by self-assembly system were discussed based on the interfacial membrane properties and the hydration, indicating the significance of the sophisticated membrane platform to perform its cooperativity.

Contents

Chapter 1

General Introduction

Structures and functions of biomolecules are fascinating but complex. Fundamental comprehension of biological function and its structure are essential for the industrial application of the biomaterials. In this chapter, some reported works, relating to the general concepts of assembly structure, lipid membrane, and intermolecular interaction were introduced to shed the light on the key concepts in this study.

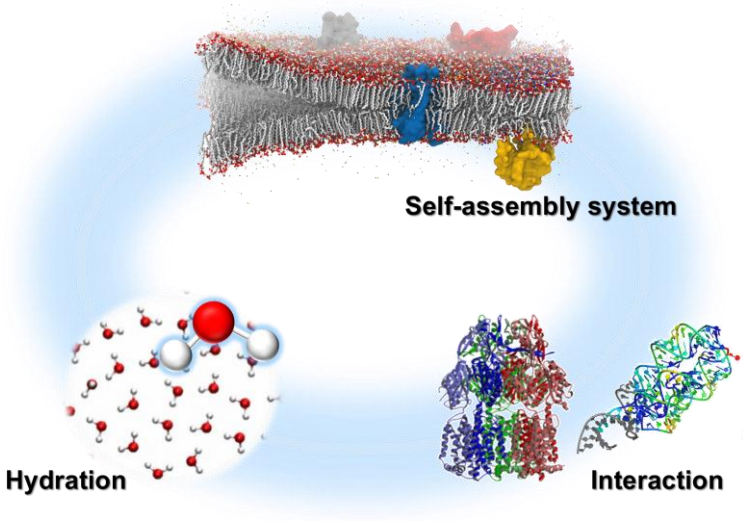

Figure 1-1 Key concepts in this study.

1. Concept of self-assembly system

Self-assembly is the process in which the components in the system spontaneously form the organized structure. There are various types of individual components; for example, the small molecules such as water molecules, the large molecules such as proteins, the visible substances *etc*. These self-assembly processes abundantly exist in the biological system, the biomolecules are interacting in the complex manners to maintain the system with highly functionalized and sophisticated order. Molecular interactions relating to the various bioprocesses can be explained with an important concept known as “molecular recognition”. For example, if the enzymes cannot recognize and bind to the

specific receptor, their functions will not work properly. Thus, it is difficult to maintain the functional physiological systems without the molecular recognition. The assemblies formed by molecular recognitions are called as supramolecular assemblies (Lehn, 1990). Basically, the molecules form a self-assembly structure via non-covalent interactions such as the electrostatic interactions, hydrophobic interactions, hydrogen bonding interactions, and van der Waals interactions, which are derived from the deference of the electric charge density even though its degree could differ depending on the interaction pairs.

Table 1-1 Examples of supramolecular assemblies

	Host/Receptor	**Guest/Ligand**	**Dissociation constant K_D [M]**	**References**
Synthetic host-guest pair	Pillararenes	Basic amino acids	10^{-4}	Li *et al.*, 2013
	β-Cyclodexistrin	Cholesterol	$10^{-3} – 10^{-5}$	López *et al*., 2011
	Cucurbiturils	Basic amino acids	10^{-3}	Urbach *et al.*, 2011
	Molecular tweezers	Lysine- or arginine-containing proteins	$10^{-4} – 10^{-6}$	Schrader *et al*., 2016
Ligand-Receptor pair	Avidin	Biotin	10^{-15}	Israerachvili, 1985
	Antibody	Antigen	$10^{-7} – 10^{-11}$	
	Receptor	Hormone	10^{-9}	
	Enzyme	Substrate	$10^{-3} – 10^{-9}$	
	Transport protein	Hormone	$10^{-6} – 10^{-8}$	
	Lectins	Glycoconjugates	$10^{-3} – 10^{-5}$	

In particular, the most abundant molecules in the physiological condition are the water molecules. Therefore, the electrostatic-driven interactions should be unfavorable in the polar solvent in which the all charge deviations can be cancelled out by the solvation from the solvent molecules. Questions have been raised how and why such sophisticated biosystems can be established and maintained in spite of the unfavorable polar environments for the molecular recognitions. Herein, the "*interface*" is an important concept to clue the questions. In the biological systems, the hydrophobic/hydrophilic

interfaces abundantly exist in the biomolecules, for example, the cell membranes, the base pair in nucleic acids, and proteins and so on. These interfaces are essential for maintaining the structure of biomolecules and for the molecular recognition. The strength of noncovalent interactions can be easily altered by the interfacial environments, not only by the charge distribution of the pair molecules. The research group of Kunitake estimated the binding constants of molecular recognition pair at the air/water interface (Ikeura *et al.*, 1991). They suggested that the hydrogen bonding formed in biomolecular pairs, such as amino acids, nucleic acids, nucleotides and sugars, can be enhanced at the hydrophobic/hydrophilic interface, which indicates that the "molecular recognition" could be promoted at the interface (Kurihara *et al*., 1991a, 1991b; Sasaki *et al*., 1992). Furthermore, they also suggested that the molecular interaction affinity would increase in the side of nonpolar environment at the interface (Ariga *et al.*, 1998). Taken the example of the guanidinium and phosphate as the interaction pair, the binding constant between these two moieties would dramatically increase at the lipid/water interface (Onda *et al*., 1996). From the estimation of the distance dependency to the interaction binding constants, it is revealed that the dielectric constants have significant impact on the binding affinity. If the hydrogen bonding parts were existing in the environment with lower dielectric constants, the binding energy would be high, and vice versa (Sakurai *et al*., 1997). As shown in these examples, the interactions performed at the interface play important role to establish the self-assembled systems (Kunitake, 1992). Besides, each interactions would impact each other by ordering or orientating, and these cooperativity would finally result in the performance of their function (Marcelja *et al.*, 1976).

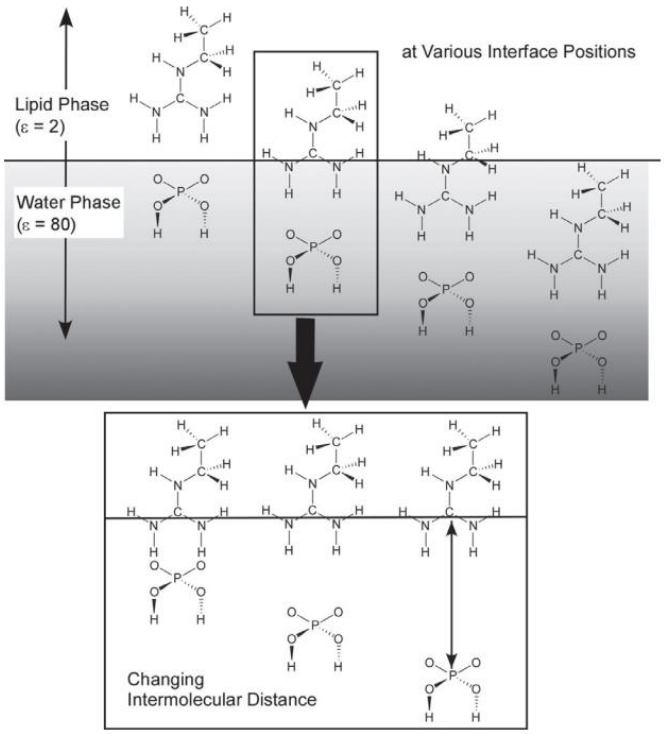

Figure 1-2 The interaction at the lipid/water interface (Sakurai *et al*., 1997).

2. Biological function of the lipid membrane

Plasma membrane bilayers play a fundamental role of regulating cellular function by delineating a membrane wall which divides the intracellular and the extracellular spaces. In addition, each role of the membrane, such as encapsulation, localization of proteins, and molecular permeation across the membrane, can depend on the compositions of their membrane proteins and lipid species (Luckey, 2012) (**Table 1-2**).

Integration of external (or internal) biomolecules into the membrane surface is promoted by several factors: the electrostatic and hydrophobic interactions between those molecules and the membranes are usually dominant (Alberts *et al*., 2014; Jin *et al*., 2008; Villar *et al*., 2016). Furthermore, the water molecules at the interface of lipid membrane can control the activities of biomolecules by modulating the membrane properties, e.g., surface pressure, coordination of hydrogen bonding, and surface charge state (Alarcón *et al*., 2016; Costard *et al*., 2014; Damodaran, 1998; Saito *et al*., 2011; Sparr *et al*., 2001). In regards to the lipid membrane as the hydrophobic/hydrophilic interface, the interactions working on the membrane is not simple. For the typical colloidal system of

rigid particles in water, it is a rare case that more than two forces working between surfaces in liquids out of four main forces: van der Waals, electrostatic, solvation and steric hindrance. In contrast, the forces between the highly mobile amphiphilic surfaces of the fluid lipid membrane and flexible biomolecules could have all types of forces simultaneously. **Figure 1-3** shows the possible forces working on the lipid membranes (Israelachvili, 1985).

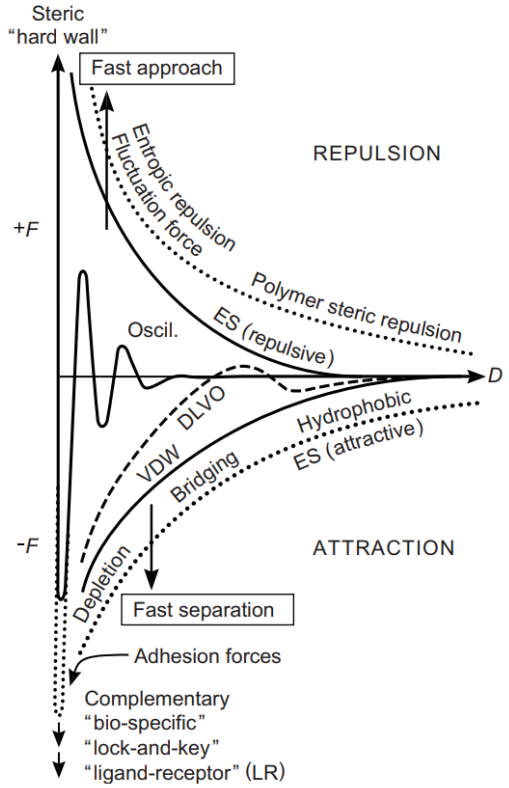

Figure 1-3 General over view of the interaction forces working on the bio interfaces (Israelachvili, 1985).

Table 1-2 Interactions between the lipid membranes and biomolecules

Type of Interactions	Relating Molecules/ Domain	Mechanism	References
Protein Binding	Pleckstrin-homology	• Specificity to Phosphoinositide Ligand of basic amino acids in the β1/β2 loop	Wang *et al.,* 1995 Mayer *et al.,* 1993
	• C2 domain • Annexin	• Binding to the acidic lipid molecules in a Ca^{2+} dependent manner	Davletov *et al*., 1993 Kenis *et al*., 2004
	BAR domain	• Preferable binding to membrane curvature	Koch *et al.,* 2011
Signal transduction	Phosphatidylinositol	• Most acidic phospholipids • Phosphorylated in various types	Yeagle *et al*., 2016
	Raft domain	• Ordered lipid domain rich with sphingomyelin and cholesterol	Simons *et al.,*1997
Protein folding	LacY, PheP, GapP	• Configurational adjustment by phosphatidylethanolamine	Picas *et al*., 2010
Ion channel	Kir, TRP, KCNQ	• Voltage-gating via transmembrane potenial gradient	Hille *et al.,* 2001 Purves *et al.,* 2001
Translocation	SRP + RNA	• Binding of SR receptor to endoplasmic reticulum or plasma membrane	Walter *et al.,* 2000 Costa *et al.,* 2018

In addition, the high fluidity of the lipid membrane could induce the rearrangement of the molecular alignment. Lateral dispersion of the lipid molecules adjust the alignment of molecules or membrane surface in response to external stimuli. For example, the addition of the cationic ions into the lipid membrane solution composed of negatively charged and amphiphilic lipids promotes the segregation of negatively charged lipids, which finally induces the adhesion and fusion of bilayer membrane (Leckband *et al.*, 1993). Lateral dispersion of lipid molecules could also act as a trigger for the molecular interaction. Raft domain, the ordered lipid cluster enriched with sphingomyelins and cholesterols, have been studied for their function to facilitate interactions with proteins and nucleic acids due to its highly ordered and hydrophobic properties (Simons *et al.*, 2010; Simons *et al.*, 1997). As suggested from the examples, the comprehension of the fundamental properties of the lipid membrane surface still needs to be investigated.

3. Recent application of the lipid membrane system

Application of lipid self-assembly systems has been encouraged in various fields (**Table 1-3**). For example, in the medical filed, their potential as the carrier for the drug delivery systems (DDSs) has been extensively studied. Drug molecules or nucleic acid medicines encapsulated in lipid self-assemblies could be released into the target cells, followed by the fusion with cell membranes. Other examples using lipid membranes are the developments of the biosensors. Lipid membranes could maintain the membrane proteins, enzymes, antibodies, and receptors in the preserved physiological condition; in other words, it is possible to mimic the cell condition and its sensitivity in the laboratory-scale experiments. Electrochemical properties of an artificial lipid membrane can be readily recorded with the high sensitivity, and the detector has great variety for the choices of the system by incorporating various bioelements respective to the objectives. Many applications based on lipid membrane-based biosensors have been reported for environmental monitoring and clinical diagnosis (Siontorou *et al.*, 2017).

For the design of this assemblies system, the unclear factors remain because of the flexible structure of the lipid membrane. In the use of the biosensors, the lipid membrane could provide inherent signal amplification. The interaction between the biological elements and analytes affects the membrane dynamics such as the dipole potential of the membrane, the surface charge, the molecular packing and fluidity *etc*. In the drug

discovery or drug delivery, the evaluation of the interactions with the lipid membrane have been the great issue that should be clarified. Since drugs (or delivered assemblies) are designed to target the reaction (active) sites existing in the cell, the interactions with cell membrane must significantly affect drug pharmacokinetics (distribution, accumulation, transport) and drug efficacy (Peetla *et al*., 2009). Therefore, substantial requires exist for the fundamental comprehension regarding to their interactions on the lipid membranes.

Table 1-3 Applications of the lipid membrane

Examples	Target	System	References
Biosensor	Amyloid-β protein	Cholesterol incorporated liposomes	Murakami *et al*., 2016
	Cholesterol	Cholesterol oxidase/ polymerized membrane	Nikoleli *et al.,* 2013
	Cholera toxin	Ganglioside GM1/ liposomes	Chen *et al.,* 2008
	Glucose	Glucose oxidase/ micro peroxidase liposomes	Graça *et al*., 2014
Cell-free protein synthesis	Protein synthesis	Cell extract/ energy source amino acids/ genes/ liposomes	Shimizu *et al*., 2001
Drug delivery	Drug molecules (small molecules, gene molecules etc.)	Liposomes (Cationic liposomes/ polymeric coatings/ modification of receptor etc.)	Siontorou *et al*., 2017
Drug discovery	Elucidation of physiological response	Liposomes (Protein – lipid interaction/ heat response etc.)	Török *et al*., 2014

4. Examples of interaction between lipid membrane and nucleic acid

One of the molecular interactions collecting a number of attention is the interaction between lipid membranes and nucleic acids (**Table 1-4**). As briefly mentioned above, the nucleic acids have been extensively studied as a new drug for the gene therapy, and the design of the drug carrier using lipid-assembly system is the big challenge for the effective delivery. Lipoplexes, the complexes of cationic lipids with nucleic acids, have been successfully used as transfection agents for gene delivery applications, while, the detailed mechanisms of lipid–nucleic acid complexation is unravelling (Aissaoui *et al*., 2002; Patil *et al*., 2005; Wagner, 2004). In another research field, the lipid-nucleic acid interaction has been discussed as a major question in the protocells; how the lipid membrane interact and promote reactions with RNA without any other catalytic molecules (Meierhenrich *et*

al., 2010). Therefore, understanding of the morphology of the molecular organization between lipid membranes and nucleic acids is essential both for optimizing gene delivery efficacy and for the clarification of biological mechanisms.

Various parameters influence on the interaction at the membrane surface; such as the membrane fluidities, phase states, hydrations, and surface potentials. Besides, some molecular factors relating to the nucleic acids also affect the interaction at the membrane; i.e., the hydrophobicity, surface net charge, and folding structures (single- or double-stranded, or folded). In many systems, cationic modifications of the membrane surfaces can be found to induce the strong adsorption targeting the negatively charged nucleic acid molecules (Chesnoy *et al.*, 2000). The adsorption can be controlled with some factors such as the lipid phase state and the ionic strength of solution. High incorporation of the nucleic acids after heating-cooling cycles observed in the lipid membrane which occurs a phase transition during the heating-cooling cycle, suggesting the cooperativity of the hydrophobic interaction between exposed hydrophobic region of the membrane and the nucleic acids, together with the electrostatic interactions (Barreleiro *et al*., 2000; Subramanian *et al*., 2000). Divalent cationic ions (Ca^{2+}, Mg^{2+}, Zn^{2+}, *etc*.) are known to induce the adsorption of nucleic acids. Although the precise mechanism is still unclear, the result that the addition of Zn^{2+} decreased 50% of the hydration shell on the lipid membrane suggests the formation of the cross-bridge among lipid-ion-nucleic acid following the dehydration at the membrane surface (Binder, 2003). Seemingly, the surface charge density is the important factor, but some other studies suggested the cationic modification is not necessarily required. Janas *et al*. observed specific bindings between hair-pin structure ribonucleic acids (RNAs) and 1,2-dioleoyl-*sn*-glycero-3-phosphocholine (DOPC)/cholesterol (4/1) membranes. From their findings, the unstable structures of RNAs, such as the single loop or the exposed hydrophobic part, are also considered to be essential factor for the interaction (Janas *et al*., 2006). Besides, the fatty acid vesicles facilitated the affinity and stabilized the RNA conformation, the self-assembled structure could be rather important for the interaction than the surface charge or ionic conditions (Saha *et al*., 2018). Therefore, the interaction properties should be discussed with the interfacial properties which dominates the interaction field.

Table 1-4 Types of the interactions between lipid membrane and nucleic acids

System	Lipid	Nucleic acid	Interaction behavior	References
Cationic lipid modification	Cationic lipid CTAB	λ-DNA(48.5 kbp), E-Coli DNA(200 bp)	K_a 10^3~10^4 M	Spink *et al.*, 1997
	Cationic lipid (DDAB, DOTAP) in 50% ethanol aqueous solution	tRNA (< 100 nt)	K_a 10^4~10^5 M	Marty *et al.*,2009
Addition of the divalent cation (Ca^{2+}, Mg^{2+}, Zn^{2+})	DPPC	Salmon sperm fragmented DNA (0.5–1 kbp)	Increase of T_m at low Zn^{2+} concentration	Suleymanoglu *et al.*,2004
	DPPC	Calf-thymus DNA	Decrease of lamellar repeat distance in SAXS	McManus *et al.*, 2003
At the liquid-crystalline phase	Zwitterionic lipid DMPE	tRNA (< 100 nt)	Decrease of transition peak temperature width at half ΔC_p maximum (1.6 $\Rightarrow$ 1.3 ℃)	Koiv *et al.*, 1994
Heterogenic phase	Zwitterionic lipid DMPC/ Cationic sphingosine	Calf-thymus DNA	Increase of T_m of cationic lipid phase	Koiv *et al.*, 1994
	Zwitterionic lipid DOPC/Cholesterol	Hairpin structure RNAs (< 120 nt)	K_a <10^2 M	Janas *et al.*, 2006

5. Important role of the hydration water at lipid membrane

Hydration is the most fundamental and essential factor to evaluate the capability of interactions at hydrophobic/hydrophilic interface. Dehydration processes could be one of possible triggers for the molecular aggregation, and the dielectric constants could be the important index of the solvent system to determine the affinity (Laage *et al*., 2017). Specifically, at the lipid membrane surface, the amphiphilic molecular properties of lipid molecules could involve with the behavior of water molecules which act both as steric molecules and as the solvent determinants. Generally, the word "*membrane surface*" indicates the hydrophilic region of the lipid bilayer, which behaves as the interface of interaction with the surrounding solvent water. The "*membrane interface*" indicates the border region between the hydrophilic and the hydrophobic regions of the membrane, that is, the region around the carbonyl group of the lipid molecules. The "*membrane interphase*" could be the region between the membrane surface and the membrane interface as shown in **Figure 1-4** (Disalvo *et al*., 2014).

The hydration state of the lipid membrane cannot be simply defined owing to the various contributing factors, for example, the chemical structure of the lipid head group, packing states of acyl chains, lateral interactions between lipids, *etc*. A typical

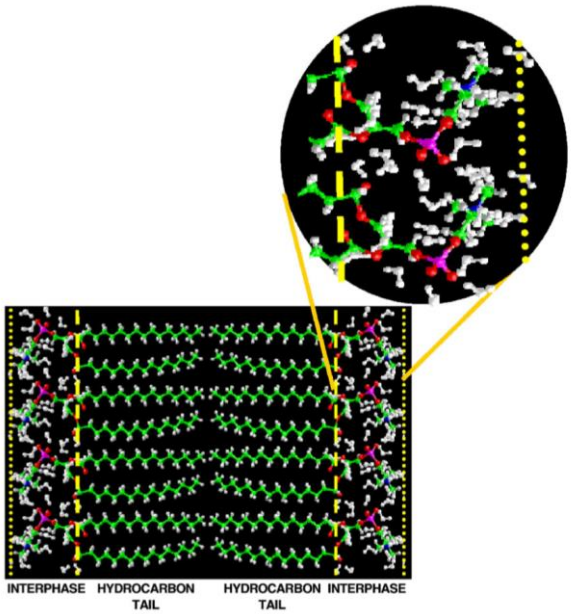

Figure 1-4 Definition of the hydration environments of the lipid bilayer (Disalvo *et al*., 2008).

zwitterionic phospholipid, e.g., diacylglycerophosphocholine (PC) known as lecithin, possesses both negatively charged phosphate group and positively charged choline group. The zwitterionic head groups are strongly hydrated via hydrogen bonds with solvent water. In a phosphate group, the bound water molecules are retained in a tetrahedral structure around the oxygen atoms (Damodaran, 1998; Lopez *et al*., 2004; Mondal *et al*., 2012). The water molecules associated with the positively charged choline group are weakly connected to each other in a clathrate hydration state (Damodaran, 1998; Mondal *et al*., 2012). The hydration property of the membrane can be varied depending on the lipid head group. In consideration of other factors that could influence the hydration behaviors, the simulation study on the associated dynamics has been achieved based on the fact that the hydrogen bonds between the water molecules are strengthened on the lipid membrane that is composed of phosphoethanolamine (PE) lipids (Damodaran, 1998). The PE has a small head group which preferentially provide a flat membrane surface (almost no curvature), thus resulting in the enclosure of lipid molecules. From this point of view, it is considered that the uniformity of the charge characteristics of the surface layer also contribute to the stability of the bonds between the water molecules (Lairion *et al.*, 2009). In general, the hydration layer could be formed on the surface of the lipid membrane and prevent the access of water-soluble molecules, despite the existence of the thin hydration layer which has a thickness of approximately 1 nm (Zwang *et al*., 2010). It is still unclear how such a hydration layer can inhibit the access to external molecules.

The water exchange could be the important concept to consider the activity of hydrated water. Especially, for the analysis of the interaction with peptides in the monolayer system, the "*cut off*" surface pressure is used in which the surface pressure becomes insensitive to the peptide penetration (Disalvo *et al*., 2008; Martini *et al.*, 2007). The "*cut off*" surface pressures for PCs and for PEs are approximately 40 mN/m and 30.6 mN/m, respectively. Considering the surface pressure of the saturated PC monolayer (approximately in the range of 46.6–48.0 mN/m), the surface pressure value of the PC monolayer is relatively lower. From these results, it is suggested that the protein does not penetrate at pressures that are much lower than the pressures at which the head group is filled. This indicates that an extra free energy is required to adsorb the protein, thus suggesting that the thermodynamically active water exceeds that within the hydrated shell. The significantly lower "*cut off*" surface pressure of the PE monolayer indicates the

existence of a smaller amount of thermodynamically active water.

As shown in these examples, the hydration state in the lipid membrane is complicated, and mechanisms of stabilization of each hydration can be varied depending on lipid spiecies. However, it is an interesting task to ascertain whether the membrane properties determine the hydration characteristics, or whether the hydration characteristics determine the membrane properties, and how this works for the interaction with biomolecules. The evaluation of the hydration water behaviors can be dependent on the measurement method in accordance with the characteristics of the target water, therefore, it is important to select the appropriate experimental method for the objective (**Figure 1-5**).

Considering the above discussions, it is important to clarify the mechanism of the interaction occurring at the membrane surface (or interface) based on the aspects of (1) the configurations in the molecular level and (2) the solvatochromic aspects. Regarding (1) about configurational aspect, characterization of the active surface of the lipid

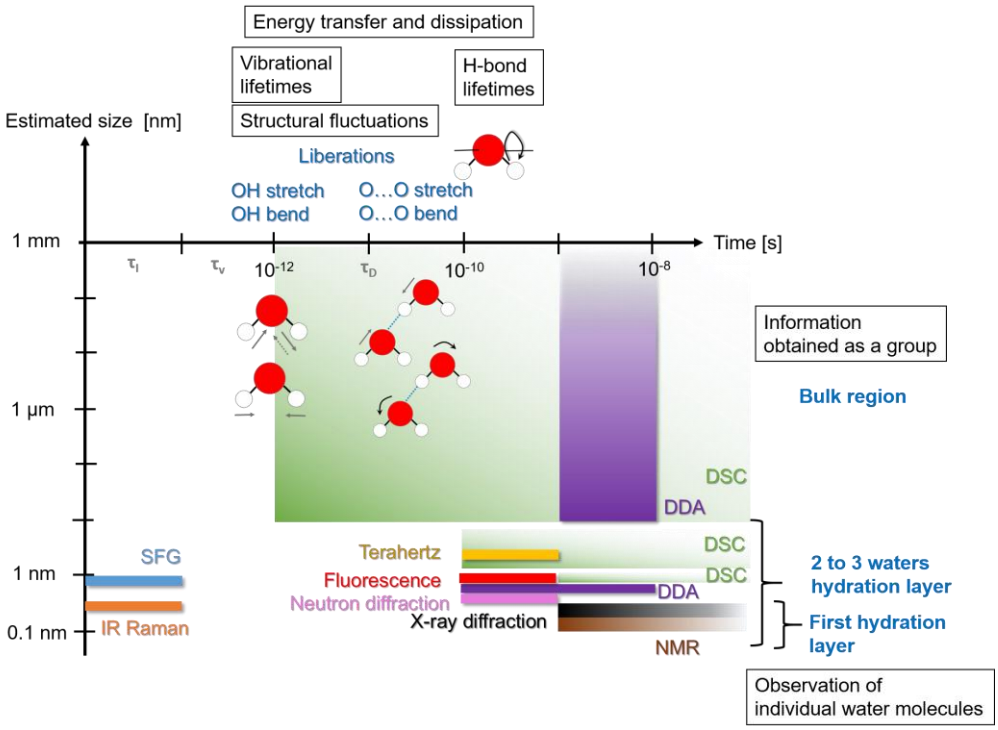

Figure 1-5 Experimental approach for the investigation of water dynamics. The molecular properties of waters were summarized according to the review by Laage *et al* (Laage *et al*., 2017).

membrane would be useful for the development of the highly sensitive biosensors and for the design of the drug carrier. One aspect relating to the clarification of the configurational factors could lead to the suggestion of the specificity of the self-assembly system, in other words, there is the possibility of the self-assembly system to prepare certain structure to accept corresponding molecules by modulating its organization. Though the structure of the assembly system could be explained as the "*membrane fluctuation*", the selectivity generated by the assembled structure could be the interaction which is energetically favorable and/or which is intrinsically accomplished on the membrane surface. This hypothesis may also contribute to the concept of the protocells in biology. In relation to another important aspect (2), the comprehension of the solvatochromic property of the membrane interface is necessary to assess the ability of the interaction. In particular, the biological interface can be explained with the gradient of the water population. The gap between the polar environment side and the nonpolar environment side at the interface could act as the "*active*" gradient, and may provide the interaction force, which cannot be explained only with the concept of the hydrophobic force. The existence of the "*active*" forces working on the gradient of the dielectric constants could give new insight in the interfacial chemistry.

6. Overview of this study

The final purpose of this study is to clarify the mechanism of the molecular interaction that could be cooperatively induced at the lipid membrane and to design the functional interactions based on the interfacial property of lipid membrane. Especially, from the aspects of the cooperative molecular interaction at the membrane surface, solvatochromic properties of the membrane and configurations of membrane-constituting molecules were studied, taking the nucleic acids as the model biomacromolecules. Furthermore, the specificity of the interaction created by the self-assembled structure were investigated. The flame work and the flow chart of the present study are shown in **Figures 1-6** and **1-7**, respectively.

In Chapters 2 and 3, the investigation for the hydration characteristic at the membrane interface were performed. Especially, in Chapter 2, the approach based on the solvatochromism was aimed using a solvent sensitive fluorescence molecule, Laurdan.

The local environment in the vicinity of the lipid molecules can be detected due to the localization of Laurdan into the lipid membrane. The four component-deconvolution method of the steady-state emission of Laurdan was developed to monitor the contributions of multiple types of solvent environments; nonpolar, polar aprotic, and polar protic with low and high dielectric constants. In Chapter 3, the approach based on the kinetics of the hydration behavior was investigated using the time-resolved fluorescence emission spectrum of Laurdan. This method gives the fluorescence lifetimes in a nanosecond scale. Time-based and emission-based information were assigned as the contribution from water groups with the collisional and relaxing properties, respectively. This assumption enabled us to estimate the number of the water molecules hydrating per lipid molecule, which could give the novel knowledge about the physicochemical impact of water molecules to the membrane properties. Based on these results, the regulation of dynamic active water molecules at the membrane interface was assumed to affect interaction, a strategy to modify the membrane interface was proposed focusing on the "hydration" in the following chapters.

In Chapter 4, the guanidinium modified vesicle membranes were designed aiming for the hydrophobic effect on the intermolecular interaction at the lipid membrane. Guanidinum is the moiety that exhibits chaotropic property, hence, the hydrogen bonding formed between water molecules can be disrupted by this molecules. From the analysis of infrared spectroscopy, Raman spectroscopy, and fluorescence of probes, the membrane properties such as the lateral packing, hydrophobicity and intermolecular interactions were higher in the membrane having the guanidinium molecules, stearyl guanidinium (SG), which have a longer acyl chain and a small head group. High affinities with tRNAs were observed in the SG modified membranes.

In Chapter 5, the interaction mechanism on the lipid membrane was investigated. According to the analysis of the Laurdan fluorescence, the differences of the spectra between in the absence and presence of the interaction were observed. This indicates that the dehydration process occurs during the interaction, and the thermodynamics of the interaction can be estimated from the contribution of the dehydration and the binding affinity. Furthermore, the nucleobase selectivity in the adsorption on the lipid membrane was observed, suggesting that the membrane arrangement specific to the certain molecules can be generated in the self-assembly system. This assumption should provide

the significant insight on the comprehension of adsorption behavior.

In Chapter 6, the cooperative effects of guanidinium modification on lipid membrane and the tRNA conformation were investigated. The modification of the cationic guanidinium dramatically increased the binding affinity with tRNA. From the pH response of the fluorescence probe, the large pK_a values were observed in guanidinium modified membrane, suggesting the surface charge density or hydration property can be provided by the intermolecular lipid interactions, and the obtained surface properties have significant impact on the adsorption of tRNA. From the circular dichroic spectroscopy during the phase transition, the specific interaction with tRNA was observed, suggesting the nucleobase selectivity of tRNA by the self-assembled lipid structure.

In Chapter 7, the results obtained in this work are summarized in General Conclusions, and Suggestions for Future Works are described as extension of this thesis.

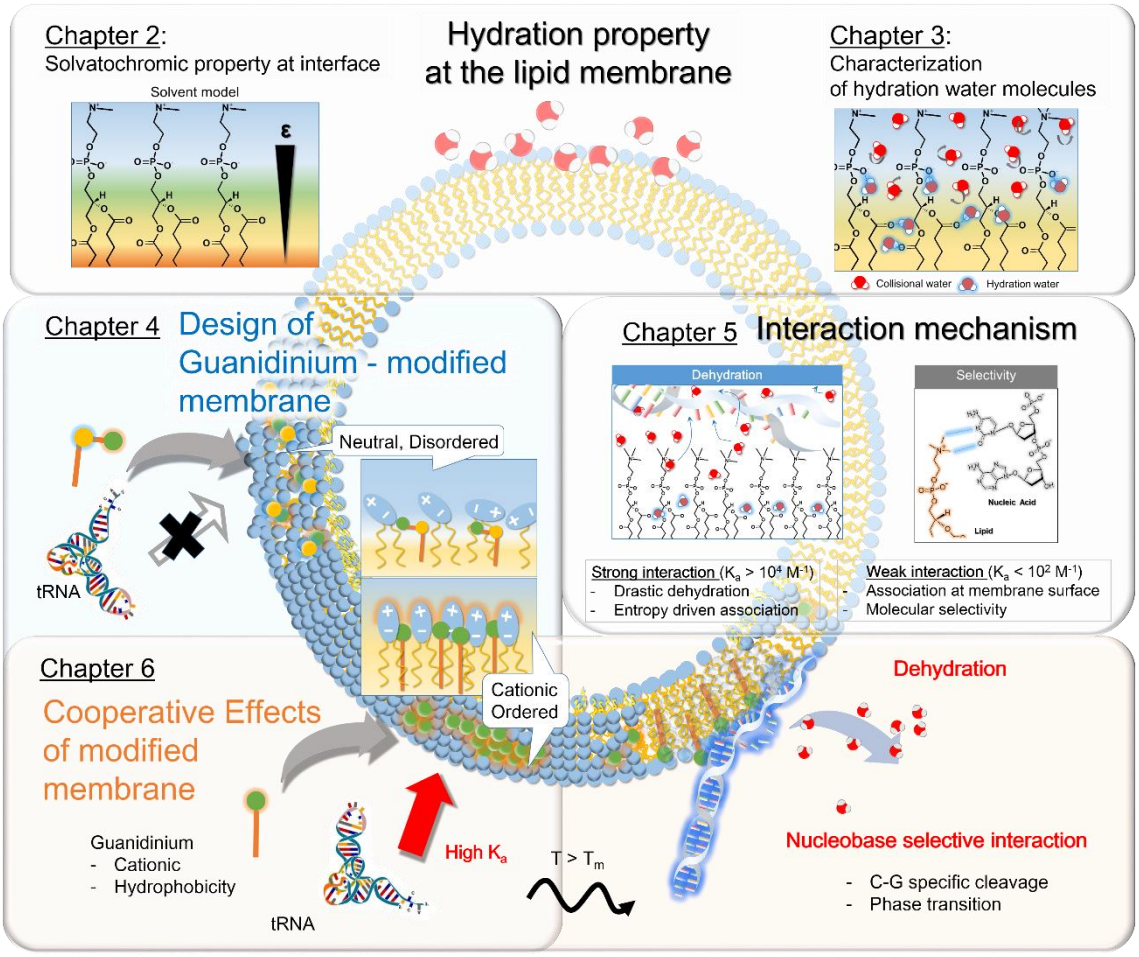

Figure 1-6 Concept of this study.

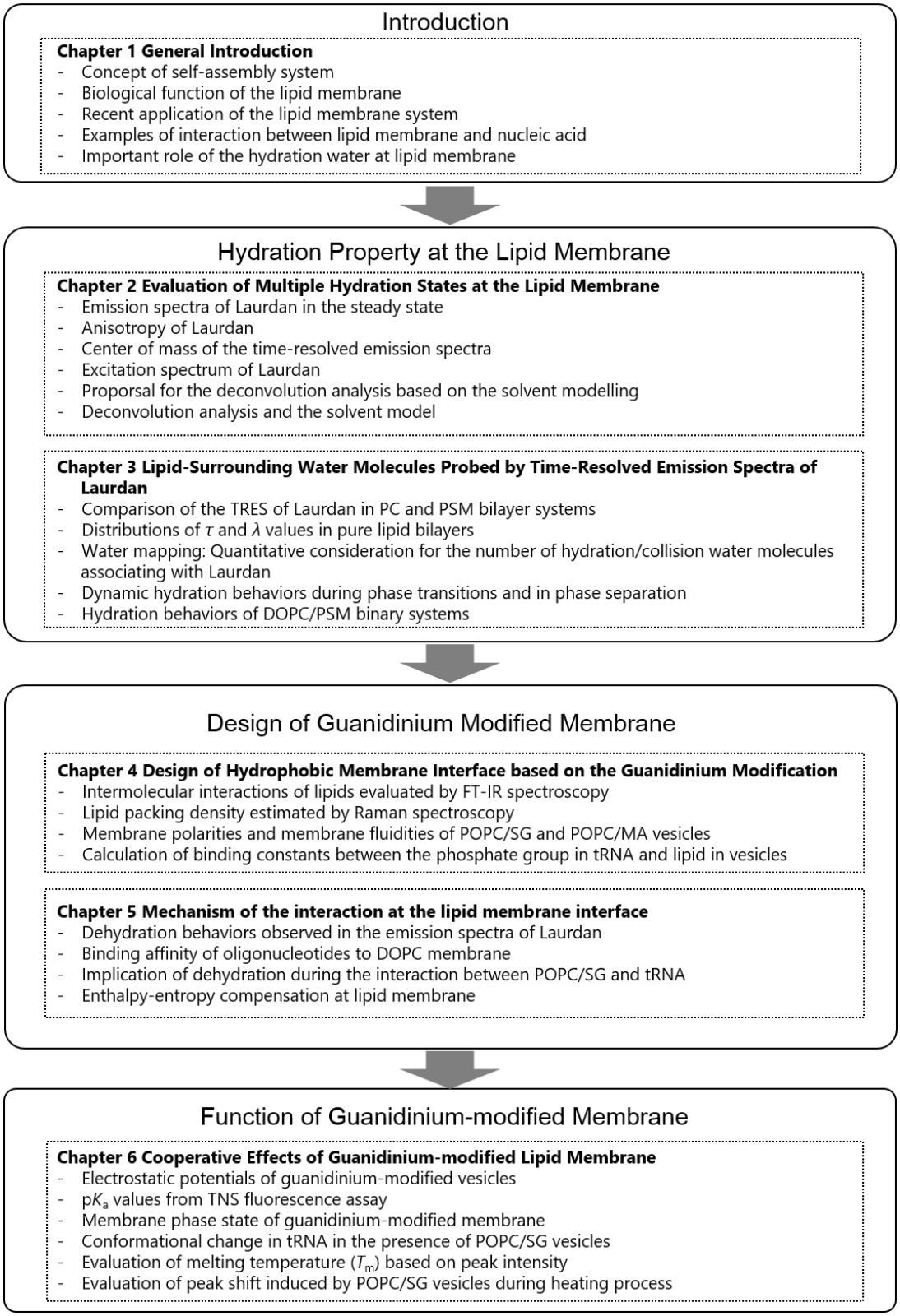

Figure 1-7 Framework of the present study

Chapter 2

Evaluation of Multiple Hydration States at the Lipid Membrane

1. Introduction

The integration of external (or internal) biomolecules into the lipid membrane surface is dominantly promoted by: the electrostatic and hydrophobic interactions between those molecules and the membranes (Alberts *et al*., 2014; Jin *et al*., 2008; Villar *et al*., 2016). Furthermore, the water molecules at the interface of the lipid membrane can control the activities of biomolecules by modulating the surface pressure, coordination of hydrogen bonding, and surface charge state (Alarcón *et al*., 2016; Costard *et al*., 2014; Damodaran, 1998; Saito *et al*., 2011; Sparr *et al.*, 2001). Lipid rafts, usually composed of sphingolipids and cholesterol, have been attracting research attention for many years because of their specific interaction with biomolecules (Barenholz, 2004; Casem, 2016; Lajoie *et al.*, 2010; Simons *et al*., 1997; Slotte, 2016). In the lipid raft, the membrane interface could be maintained in a less hydrated state because of the rigid and ordered alignments of lipid molecules, which results in the tight lipid packing and then excludes the water molecules out from the membrane. Therefore, the membrane polarity in the lipid raft is thought to play an important role in the integration of molecules and in the control of their activity. However, little is known regarding the interfacial hydration state of local raft regions compared to other regions within the same membrane because the observation of heterogenic hydration properties has not been well established.

Sphingolipids are the major lipid species known to be associated with raft domain stability (Ramstedt *et al.*, 1999). They form a strong intermolecular hydrogen bond that facilitates the segregation with high affinity to cholesterol through the hydrogen bonding acceptor (C=O, P=O, 3OH, or 2NH) and donor moieties (3OH or 2NH) (Slotte, 2016; Venable *et al*., 2014). Most of sphingolipids have long, saturated acyl chains, which allows them to be packed tightly (Ramstedt *et al.*, 1999). Even with a subtle

configurational difference of saturated or unsaturated, the physicochemical properties of sphingolipids in bilayers, such as the phase transition temperature (T_m), can vary depending on the acyl chain structure. For example, D-*erythro*-N-palmitoyl-sphingosyl phosphorylcholine (PSM), having a saturated acyl chain and an unsaturated long-chain base, shows a T_m of 41.2 ℃ in the pure bilayer form (Kuikka *et al*., 2001). D-*erythro*-N-palmitoyl-dihydrosphingomyelin (DHPSM), having a saturated long-chain base, shows a T_m of 47.7 ℃ in its bilayer form (Epand, 2003; Nyholm *et al*., 2003a, 2003b). Recent studies have reported differences in their hydrogen-bonding properties (Epand, 2003; Yasuda *et al*., 2016). Dihydro-SM is assumed to have higher affinity for cholesterol than unsaturated SM. It is clear that the molecular environments arranged via hydrogen bonds are specific in sphingomyelin bilayers; therefore, microscopic properties, such as membrane polarity or viscosity between the lipid molecules, should be properly verified.

The fluorescence probe 6-lauroyl-2-dimethylamino naphthalene (Laurdan) has been widely used to evaluate membrane hydration states (Bagatolli *et al*., 1999; De Vequi-Suplicy *et al*., 2006; Parasassi *et al*., 1991). The fluorescence emission of Laurdan is sensitive to the surrounding solvent environment. In the lipid bilayer, the amphipathic structure of Laurdan localizes it at the hydrophobic–hydrophilic interface region. Thus, the obtained information is relevant to the microscopic interfacial properties of the lipid bilayer (Bagatolli *et al*., 1999; Parasassi *et al*., 1998). Through excitation, the fluorophore moiety has a large dipole moment (Parasassi *et al*., 1998; De Vequi-Suplicy *et al*., 2014) and exhibits various emission characteristics relaxed by the surrounding solvent molecules (Bagatolli *et al*., 1999; Parasassi *et al*., 1990, 1997). An analytical method for measuring the microscopic polarity of the membrane has been developed by utilizing the emission properties of Laurdan in the lipid bilayer (Bacalum *et al*., 2013; Harris *et al*., 2002; Malacrida *et al*., 2016; Parasassi *et al*., 1998); for the two-state assumption of membrane phase state (gel phase or liquid phase), the generalized polarization (*GP*) value is widely used (Jay *et al*., 2017; Parasassi *et al*., 1991, 1997). Despite this versatility, further investigation is required to evaluate the detailed hydration states at the lipid bilayer interface, as there are many factors that affect the relaxation states of Laurdan (e.g., hydrogen bonding, lateral lipid density, and lateral heterogeneity) (Jay *et al*., 2017). As example, the broad emission spectra of the Laurdan are obtained in the sphingolipid

bilayer (Bagatolli *et al*., 1999; Massey, 2001; Nyholm *et al*., 2003a); however, from where it originates is unclear, aside from the possibility of intermolecular hydrogen bonds among SM lipids.

In this chapter, the interfacial hydration properties of bilayers prepared from different lipid species were evaluated to determine whether the different configurations, including backbone structure or degree of saturation, would affect the interfacial hydration properties of the bilayers (**Figure 2-1**), especially focusing on how the hydrogen bonding properties of PSM and DHPSM affected the interfacial polarity. The steady-state measurements of the excitation spectra, emission spectra, and the anisotropy of Laurdan were carefully investigated along with the time-resolved emission analysis. Deconvolution of obtained Laurdan fluorescence emission spectra into four components was herewith proposed based on the emission properties of the solvent system. The differences in the microscopic polar environments arranged in each lipid bilayer were discussed in this study based on the "*solvatochromic model*" of Laurdan, where its local surroundings are assigned as a solvent system.

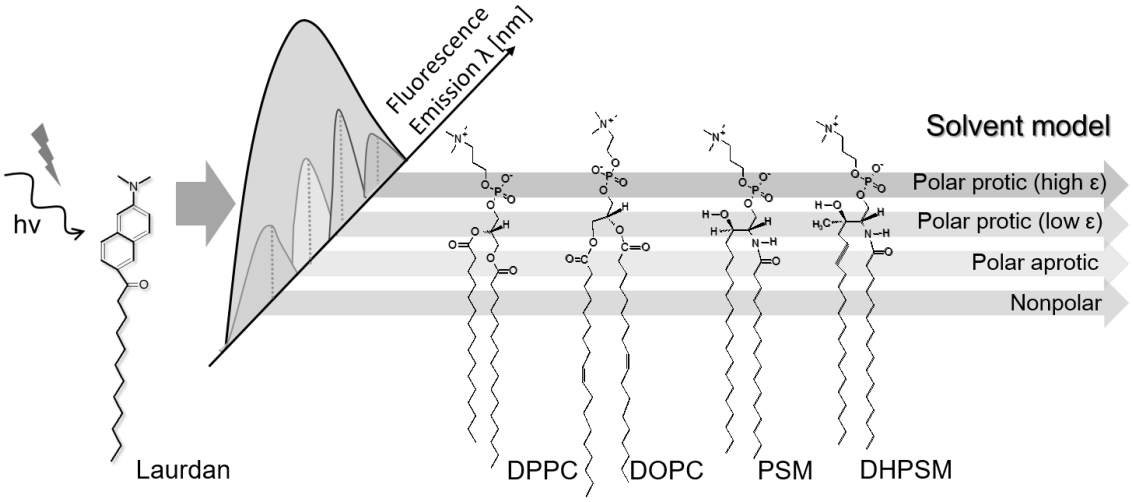

Figure 2-1 Concept in this chapter. Lipid molecules used in this study are 1, 2-dipalmitoyl-*sn*-glycero-3-phosphocholine (DPPC), 1, 2-dioleoyl-*sn*-glycero-3-phosphocholine (DOPC), PSM, and DHPSM. Laurdan is the fluorescence molecule for the assessment of membrane polarity.

2. Materials and Methods

2.1. Materials

All phospholipids (DPPC, and DOPC) and egg yolk SM were purchased from Avanti Polar Lipids (Alabaster, AL, USA). PSM was purified from egg yolk SM, as described previously (Nyholm *et al.*, 2003a). PSM was hydrogenated to yield DHPSM, as previously reported (Ramstedt *et al.*, 1999). The purity of the sphingomyelins was confirmed by mass spectrometry. Laurdan was purchased from Sigma Aldrich (St. Louis, MO, USA). Other chemicals were obtained from FUJIFILM Wako Pure Chemical Corporation (Osaka, Japan) and used without further purification.

2.2. Preparation of the lipid bilayer vesicles

Lipids and fluorescence probes were dissolved in methanol. Appropriate amounts were dispensed into glass tubes, and the solvent was evaporated under a stream of nitrogen gas. The dry lipid films were hydrated in pure water at 65 ℃ (60 min) and sonicated in a sonicator bath (Bransonic 2510; Branson Ultrasonics, CT, USA), for 5 min at 65 ℃. Large unilamellar vesicles (LUVs, 100 nm in diameter) were prepared by extrusion at 65 ℃ (Hope *et al*., 1985). The lipid concentration was measured using the method reported by Rouser *et al* (Rouser *et al*., 1970).

2.3. Fluorescence measurements of Laurdan in steady state

All samples were prepared to adjust the final lipid and Laurdan concentrations to 100 μM and 1 μM, respectively. The concentration of Laurdan was estimated from its absorbance, using the molecular extinction coefficient of 2000 cm^{-1} (Haugland, 1996). Steady-state fluorescence measurements were performed with a QuantaMaster™ (Photon Technologies International, Lawrenceville, NJ, USA). The temperature of the sample cell was monitored and regulated by a Peltier system, and data acquisition was controlled using Felix 32 software. Emission measurements were performed using excitation light at 360 nm, and the emission spectra of Laurdan were collected from 400 to 540 nm.

The generalized polarization value was measured according to a previous report (Parasassi *et al*., 1991) with the following equation:

$$GP = (I_{440} - I_{490}) / (I_{440} + I_{490}) \quad \text{(Eq. 2-1)}$$

where I_{440} is the emission intensity at 440 nm in the emission spectrum of Laurdan in the steady state, and I_{490} is the emission intensity at 490 nm.

The *GP* values decreased with an increase in temperature. Except for DOPC, the values shifted drastically based on the transition temperature. At room temperature, *GP* values become smaller in the order of DPPC > PSM > DHPSM > DOPC, which also corresponds to the order of degree of hydration.

Fluorescence anisotropy, *r*, was calculated from vertically and horizontally polarized emission intensity with the following equation:

$$r = {(I_{\mathrm{VV}} - GI_{\mathrm{VH}})}\Big/{(I_{\mathrm{VV}} + 2GI_{\mathrm{VH}})} \qquad \text{(Eq. 2-2)}$$

$$G = I_{\mathrm{HV}}/I_{\mathrm{HH}} \qquad \text{(Eq. 2-3)}$$

where the orientation of the excitation and emission polarizers were represented as follows, for example, I_{HV} for the intensity horizontally polarized excitation and vertically polarized emission, as defined in a previous report (Lakowicz, 1999). The changes of anisotropy as a function of temperature were continuously measured from 20 ℃ to 70 ℃, and the results were analyzed with the sigmoidal fitting curves, based on Boltzmann equation. The measurement was performed using excitation light at 360 nm, and the emission was measured at 490 nm.

The deconvolution of obtained emission spectra was carried out using PeakFit software (Systat Software, Inc., San Jose, CA, USA). All fitting equations were utilized with the lognormal amplitude function following a previous report (Bacalum *et al*., 2013). The equation for the fitting is as follows:

$$y = a_0 \exp\left(-\frac{1}{2}\left(\frac{\ln\frac{x}{a_1}}{a_2}\right)^2\right) \qquad \text{(Eq. 2-4)}$$

where a_0 is the amplitude, a_1 is the center ($\neq 0$), and a_2 is the width (> 0) of the fitting curve, respectively. From the fitting acquisition, the integrated area and its area ratio [%] were obtained; the integrated area was calculated from the integration of the obtained analytical curve.

2.4. Quenching experiment with 5-DOXYL and TEMPO

Fluorescence quenching experiments were performed to reveal the multiplicity of Laurdan locations in the bilayers. The spin-labeled quenchers 2-(3-carboxypropyl)4,4-dimethyl-2-tridecyl-3-oxazolidinyloxy (5-DOXYL) and 2,2,6,6-Tetramethylpiperidine 1-oxyl free radical (TEMPO) were used as a site-specific quencher and bulk-distributed quencher, respectively. The location of 5-DOXYL is estimated to be 12.15 Å (Abrams and London, 1993; Chattopadhyay and London, 1987), and the fluorescence would be quenched if the Laurdan molecules were located close to the radical molecules. TEMPO is water-soluble and is partitioned favorably into the disordered lipid membrane phase. Therefore, the quenching would be promoted as the TEMPO penetration increase.

2.5. Time-resolved fluorescence measurements

Time-resolved fluorescence measurements were all performed using the FluoTime 200 instrument (PicoQuant, Rudower Chaussee, Berlin, Germany). The sample temperature was controlled by a Peltier system, and data acquisition was performed with the PicoHarp system. The samples were excited with a 378-nm diode laser, and the emission was measured from 400 to 540 nm in 10-nm steps (14 acquisitions). The time resolution was 64 picoseconds. A decay curve was produced after 150 seconds of acquisition time. Data were analyzed using FluoFit Pro software. After integration of all decay curves, the TRES were extracted every 1.6 nanoseconds after excitation (from 7.168 ns to 48.768 ns, in 28 spectra), and the center of spectral mass (λ_c) was calculated according to a previous report as follows (Mohana-Borges *et al*., 1999):

$$\lambda_c = \sum \lambda_i F_i / \sum F_i \qquad \text{(Eq. 2-5)}$$

where F_i is the fluorescence emitted at the emission wavelength λ_i.

3. Results and Discussion

3.1. Emission spectra of Laurdan in the steady state

The fluorescence emission spectra of Laurdan were measured in the bilayers composed of DPPC, DOPC, PSM, and DHPSM. As shown in **Figure 2-2 (a)**, the Laurdan in the DPPC bilayer (T_m: 41.2 ℃) showed a sharp peak at around 440 nm, which was consistent with the reported Laurdan peak position in the gel phase bilayer (Parasassi *et al.*, 1991). The Laurdan spectrum in the DOPC bilayer showed a broader and red-shifted peak at approximately 490 nm, which was derived from the Laurdan in the liquid-crystalline phase. For the PSM and DHPSM bilayers, broader peaks were observed as compared with the spectrum in the DPPC bilayer. These findings are similar to previous results (Nyholm *et al*., 2003a), whereas narrower and blue-shifted peaks were observed in this study because of the lower experimental temperature (at 20 ℃).

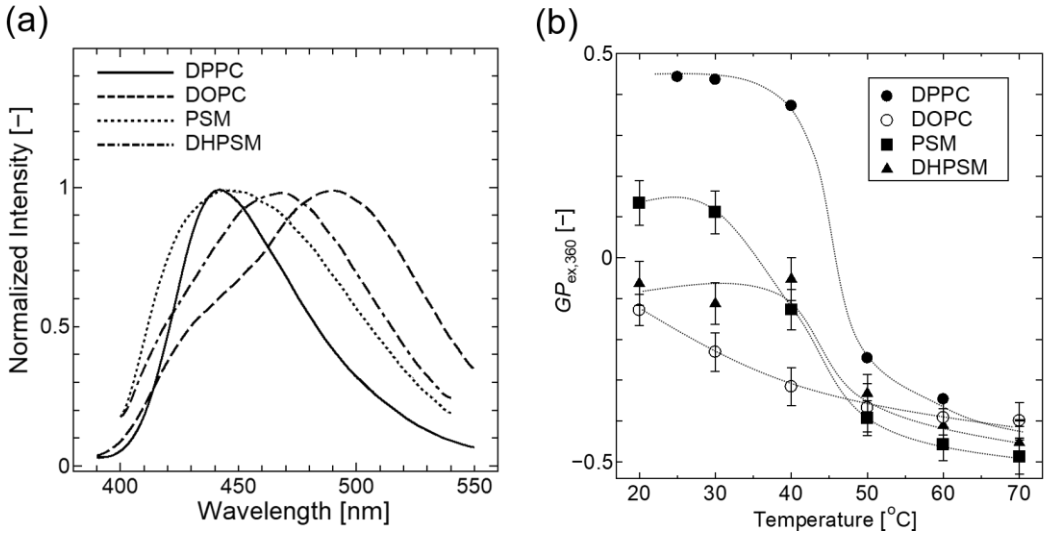

Figure 2-2 (a) Fluorescence emission spectra of Laurdan in DPPC (solid), DOPC (dash), PSM (dot), and DHPSM (dot 2-dash) bilayers at 20 ℃. The excitation wavelength was 360 nm. All spectra were normalized with the strongest peak intensity. **(b)** Transition of *GP* values in the DPPC, DOPC, PSM, and DHPSM bilayers as a function of temperature. Each lipid is depicted in the color described in the legends. The *GP* value is defined as described in Eq. 2-1. The average value was plotted from the *GP* values calculated from the three emission spectra shown in the graph **(a)**. Error bars represent SEM.

The phase transition temperatures of PSM and DHPSM in the bilayers were 41.2 ℃ and 47.7 ℃, respectively (Kuikka *et al*., 2001). In the point that these lipid bilayers have a high T_m, it is expected that the membrane properties of PSM and DHPSM bilayers could be similar and resemble that of the DPPC bilayer. However, broader peaks at 440 nm in PSM and at 460 nm in DHPSM were observed. Furthermore, the spectrum in the DHPSM bilayer was more red-shifted than in the PSM bilayer and seemed to be considerably similar to that in the DOPC bilayer. These results suggest that the Laurdan in SM bilayers would be in multiple hydration states, and it may be highly hydrated in the DHPSM bilayer. Conventional *GP* analysis was also attempted (**Figure 2-2 (b)**). The *GP* values of the SM bilayers below the T_m were relatively low, in the order of DOPC < DHPSM < PSM < DPPC, which implies that the order of hydrophobicity does not correspond to the rigidity expected from the T_m.

3.2. Anisotropy of Laurdan

Rotational mobility of Laurdan was investigated from the steady-state anisotropy (**Figure 2-3**). The anisotropy values decrease during phase transition wherein the rotational mobility or molecular freedom increase. In the DPPC bilayer, a drastic shift in the anisotropy was observed at T_m (= 41 ℃). Since the DOPC bilayer is in a fluid and disordered state, there was only a slight decrease. The PSM and DHPSM bilayers showed modestly shifted anisotropy values compared to the shift observed in the DPPC bilayer systems. Further, at temperatures below T_m, the anisotropy values in SM bilayers were slightly lower than in the DPPC bilayer. These results indicate that there are some configurational factors in SM bilayers, for example, the high saturation of hydration or hydrogen bonding, and that restrict Laurdan to have modest transition of rotational motions as the temperature increases.

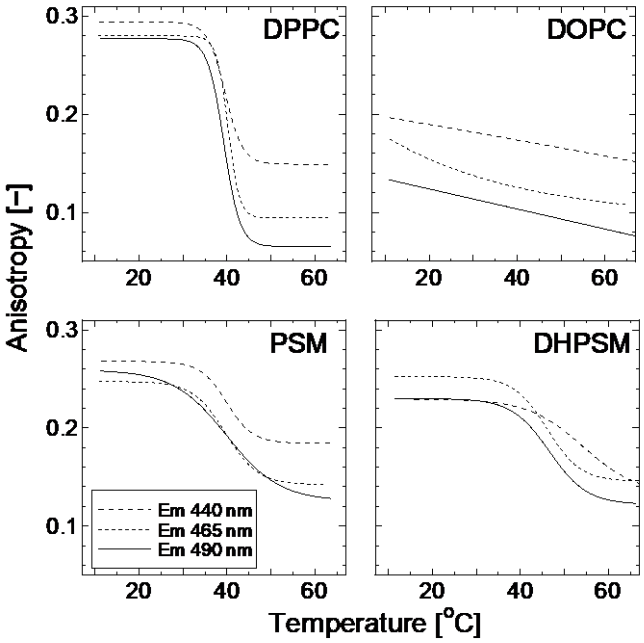

Figure 2-3 Anisotropy transitions of Laurdan in DPPC, DOPC, PSM, and DHPSM bilayers as a function of temperature. The excitation wavelength was 360 nm, and the emission wavelength was at 440 nm (dashed line), 465 nm (dotted line), and 490 nm (solid line). Anisotropy was calculated using the Eq. 2-2 and 2-3. The sigmoidal fitting curve was illustrated using the Boltzmann equation.

The anisotropy transition was dependent on the emission wavelength, and at shorter emission wavelengths, a modest shift was observed in the results of the DPPC bilayer. Anisotropy dependencies on the emission wavelength can be explained by the existence of individual molecular species that have different emission properties. For the phase transition of DHPSM bilayers, the anisotropies with the longer emission wavelengths (465 and 490 nm) shifted at a lower temperature than that at a shorter emission wavelength (440 nm), suggesting that Laurdan molecules with longer wavelength emissions have high mobility or heat sensitivity. The results shown in **Figures 2-4** indicate the fluorescence quenching by the radical reagents (5-DOXYL stearic acid (lipophilic) and 2,2,6,6-tetramethylpiperidine 1-oxyl (TEMPO, water soluble)) located at the interfacial region. The significant quenching in the longer wavelength range was observed in SM bilayers, which implies that the Laurdan molecules with red emission are locating in the shallower region of the interface. This also supports the idea of various locations of Laurdan with corresponding polarities.

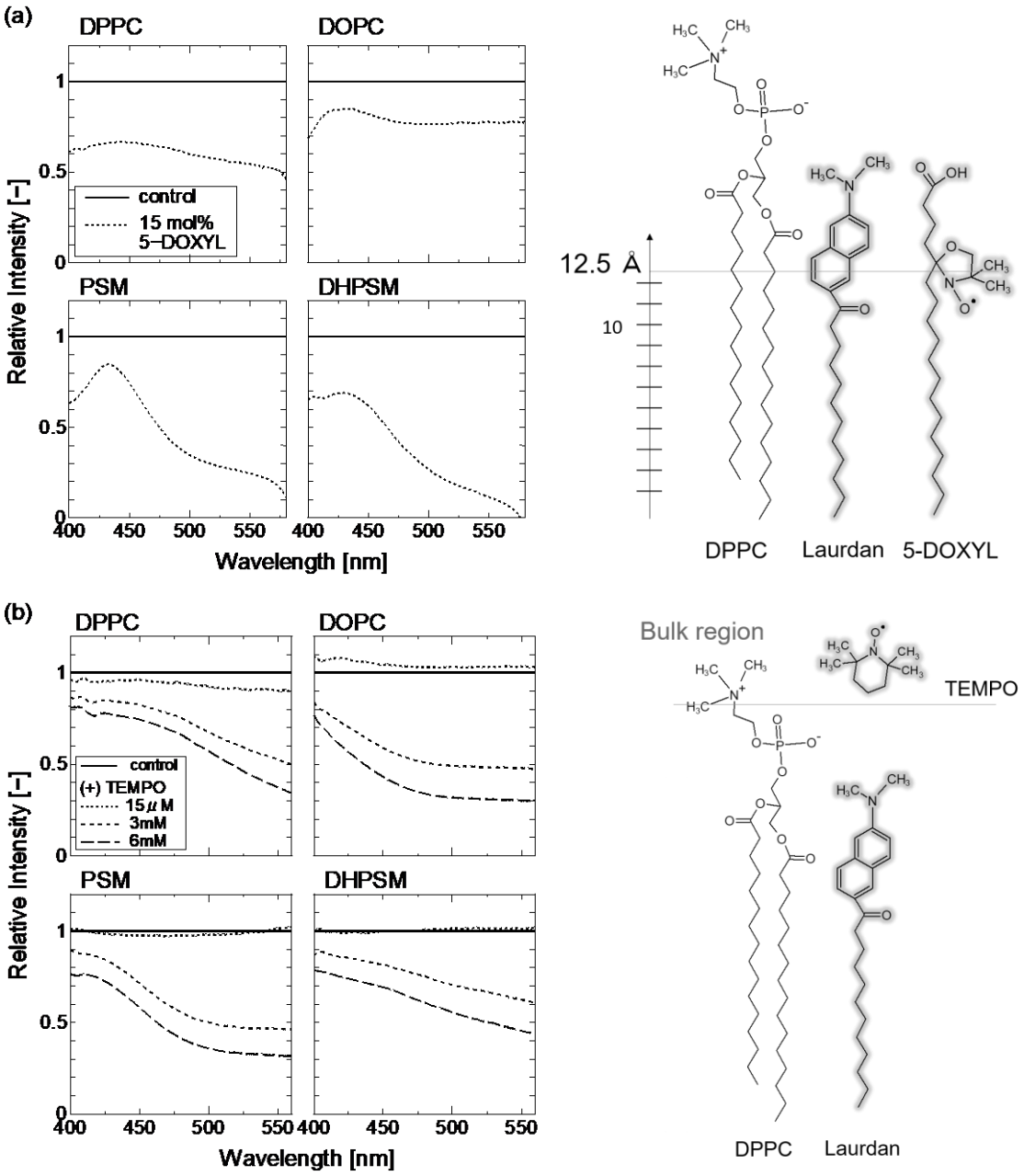

Figure 2-4 (a) Relative emission intensity of Laurdan in the presence of quencher, 5-DOXYL, shown as a spectrum. The solid lines represent the emission spectra of Laurdan as a control, and the dotted lines represent the relative intensities between the spectra obtained in the presence of 15 mol% of 5-DOXYL. **(b)** Relative emission intensity of Laurdan in the presence of quencher, TEMPO, shown as a spectrum. The solid lines represent the emission spectra of Laurdan as a control, and the dotted lines represent the relative intensities between the spectra obtained in the presence of TEMPO. All experiments were performed with a 100 μM lipid concentration and 3 mol% of Laurdan, respectively. The emission spectra were obtained with excitation at 360 nm at 20 ℃. All spectra acquisitions were repeated three times.

3.3. Center of mass of the time-resolved emission spectra

The center of mass of the time-resolved emission spectrum of Laurdan was calculated for the DPPC, DOPC, PSM, and DHPSM bilayers (**Figure 2-5**). In general, slow dipolar relaxation around the excited state of the probe makes fluorophores emitting earlier with higher energy (shorter wavelength), while fast dipolar relaxation leads a loss of energy due to environmental relaxation (higher wavelength). For the DPPC bilayer below T_m, a small shift of the center of mass was observed with decay time, which confirms the gel phase as reported is consistent with previously (Harris *et al.*, 2002; Parasassi *et al.*, 1993). This transition can be explained as the representative fluorescence properties of Laurdan in the gel phase, as observed from the shorter emission wavelength and longer fluorescence lifetime. The center of mass in the DOPC bilayer shifted to a larger emission wavelength and returned to a shorter wavelength because the dynamic solvent relaxation in the liquid-crystalline phase resulted in a red-shifted emission and a short lifetime. With regard to the temperature effect found in the DOPC bilayer, a progressive red shift and shorter decay time were observed at high temperature, indicating that significant solvent relaxation from the surrounding hydrated waters lead the lifetime of Laurdan shorter. Similar tendencies were also observed in DPPC bilayers at temperatures above T_m.

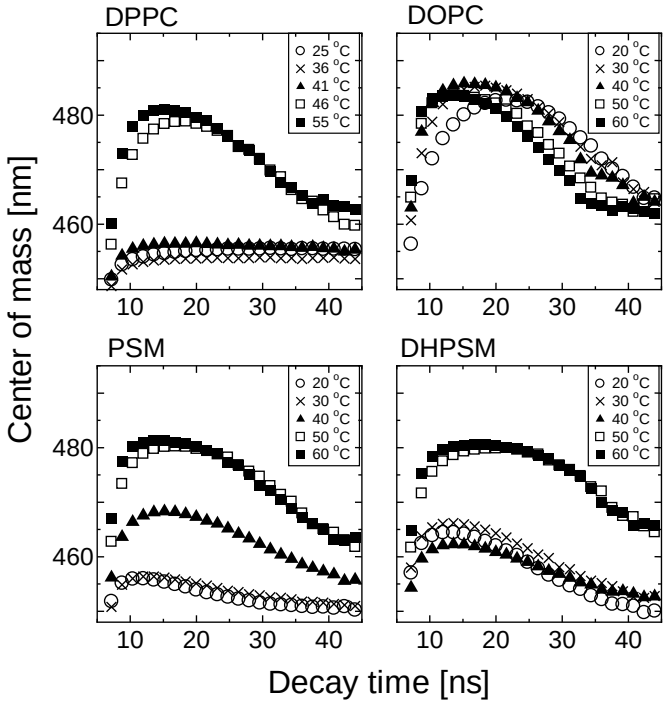

Figure 2-5 The center of mass of the time-resolved spectra of Laurdan for each bilayer at different temperature as shown in each legend. The excitation wavelength for the diode laser was 378 nm. The value of the center of mass was calculated using Eq. 2-5. Each data points were extracted every 7.168 ns.

A unique feature of sphingolipids was that the center of mass shifted to a large wavelength with a shorter decay time. This result is similar to the property observed in the liquid-crystalline phase, although the degree of red-shifting was modest compared to that in the DOPC bilayer. This suggests that there are specific molecular arrangements among SM lipids that enable Laurdan to be relaxed. Further, the transition of the center of mass in the DHPSM bilayer at a low temperature was more red-shifted compared with those in the PSM bilayers, indicating the highly hydrated property of the DHPSM bilayer. Considering the biphasic time distributions of center of mass values in DOPC and sphingomyelin bilayers, there could be at least two populations of fluorophores emitting at the shorter wavelengths: one with short lifetimes and one with long lifetimes.

3.4. Excitation spectrum of Laurdan

Figure 2-6 shows the excitation spectra of Laurdan in each lipid bilayer for the emission wavelengths 435 nm and 470 nm. According to a previous report, the specific intermolecular interactions between Laurdan and the surrounding molecules can be determined from excitation spectra (Bagatolli *et al*., 1999). The emission wavelength dependencies at 435 nm and 470 nm were significant for both SM bilayers. Greater blue-edge excitation intensity was found in the DOPC bilayer and SM bilayers. The excitation peaks with shorter wavelength could indicate energetically unfavorable states of Laurdan species, for example one in the fluid membrane wherein the quantum yield of Laurdan is relatively low (Bagatolli *et al*., 1999; Viard *et al*., 1997). In addition, the Laurdan in nonpolar (low ε) and aprotic solvent emits rather weak fluorescence (Józefowicz *et al*., 2005). Therefore, it seems that a portion of the Laurdan molecules in the DOPC and SM bilayers are energetically unfavorable because of high fluidity or low ε. The excitation spectra for the emission wavelength of 470 nm showed a decreased blue-edge intensity, revealing the different locations of Laurdan molecules depending on the emission wavelength. This increased red-band intensity in the excitation spectrum implies the presence of relaxation. The spectra in the DHPSM bilayer had relatively larger red-edge intensities than in the PSM bilayer, suggesting that the intermolecular interaction between Laurdan and the solvent molecules is greater in the DHPSM bilayer.

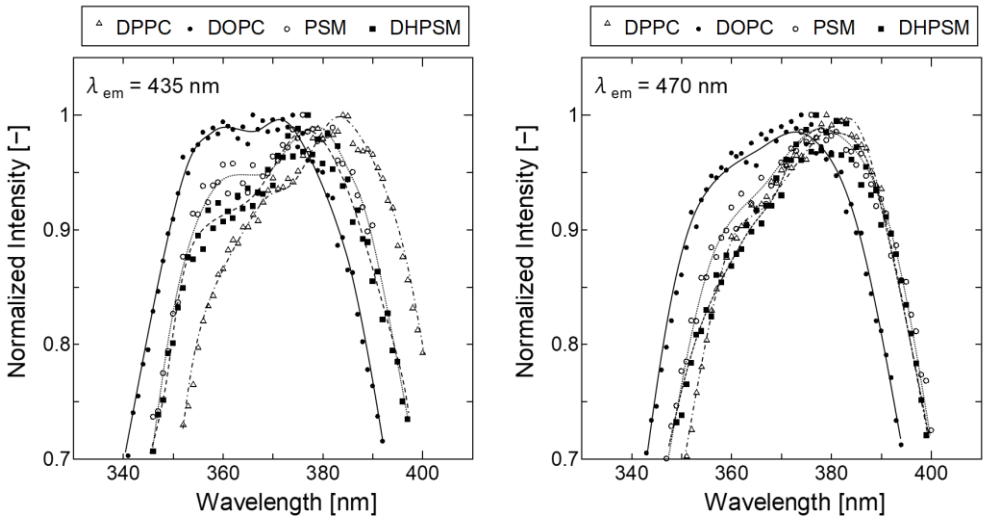

Figure 2-6 Laurdan excitation spectra of pure lipid bilayers at emission wavelength (λ_{em} = 435 nm, 470 nm) in 20℃. The symbols indicate the type of lipid bilayer: DPPC (open triangle), DOPC (closed circle), PSM (open circle), and DHPSM (closed square). All spectra were normalized with the strongest peak intensity. The spectral differences are found in our experiments compared with previous report are considered to originate from the difference of purity of the lipids (between extracted sphingomyelin and purified sphingomyelin).

The emission ratio spectra based on the different excitation wavelengths are shown in **Figure 2-7**. When the fluorescence molecules are excited with longer wavelengths, the intensity of the blue-edge emission decreases since the photo selection occurs for molecules that are already relaxed and energetically favorable (Bagatolli *et al*., 1999). The emission spectra obtained with red excitation for the DOPC and DHPSM bilayers showed lower intensities of blue-edge emission at 25 ℃, indicating that relaxation is taking place. In the DPPC, PSM, and DHPSM bilayers, spectra with blue excitation (Ex = 340 nm) showed greater intensity in the blue-edge emission above T_m (60 ℃), which implies there are still energetically un-relaxed molecules after the phase transition. These results indicate the unique heterogeneity of Laurdan in the DHPSM bilayer, which can sense both hydrophilic and hydrophobic environments.

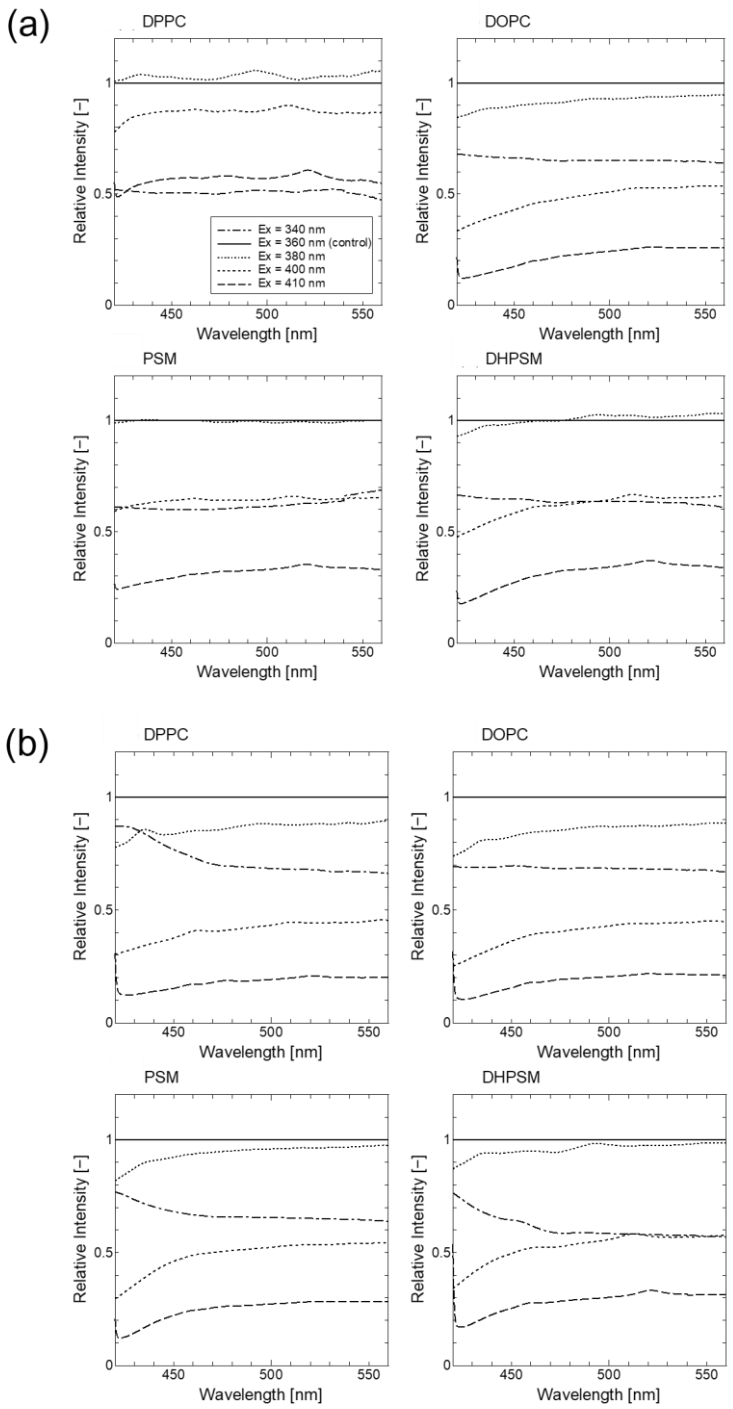

Figure 2-7 Ratio spectra between steady-state Laurdan emission spectra excited at the various excitation wavelengths. **(a)** The results obtained at 25 ℃. **(b)** The results at 60 ℃, respectively. All spectra were calculated with the spectra excited at 360 nm as a control. The arbitrary excitation wavelengths are shown in the legend. The concentrations were 100 μM of lipids and 1 mol % of Laurdan, respectively. All spectra acquisitions were repeated three times.

3.5. Proposal for the deconvolution analysis based on the solvent modelling

Analysis of the Laurdan fluorescence is a useful tool for characterizing membrane interfaces. However, it is difficult to interpret its complex molecular environment. In this chapter, the fluorescence properties were observed according to the emission wavelengths; for example, a modest shift in the anisotropy at a shorter emission wavelength (**Figure 2-3**), a short lifetime at long emission wavelength (**Figure 2-5**), and a large red-edge intensity of the excitation spectra at a longer emission wavelength (**Figure 2-6**). In particular, the properties of Laurdan in SM bilayers revealed the complexities for the interpretation, as suggested by the broad and decomposable emission peak (**Figure 2-2**), the significant quenching in the red-edge emission (**Figure 2-4**), the unique red-shift of the center of mass (**Figure 2-5**), and the emission dependence on the excitation spectra (**Figure 2-6**). This complexity is caused by a variety of excited states and the diversity of the probe's surroundings (microscopic viscosity, hydration degree, and so on) (Jay *et al*., 2017; Parasassi *et al*., 1997). Because of this complexity, common *GP* analysis often encounters discrepancies in terms of the selection of blue and red peaks (Jay *et al.*, 2017). Moreover, deconvolution analysis with the double component cannot precisely account for the molecular situation (Bacalum *et al*., 2013).

Here, the multiple deconvolution analysis based on the solvent system will be proposed to examine the local solvent environment at the membrane interface based on the correlation between the Laurdan emission peaks and the dielectric constants of the solvents. Since the local dielectric constant values of the bilayer membrane drastically shifted from ε = 10 to 70, the solvent property in the bilayer should be studied carefully (Cevc, 1990). The local solvent characteristic could be explained by separately considering molecular environments as featured solvent systems, such as nonpolar (ε < 5), polar aprotic, polar protic (low ε), and polar protic (high ε) systems. The characterization of polar protic solvent can be divided into low and high ε in order to explain the protic effect of both the water molecules penetrating the hydrophobic region of the membrane and the abundance of water molecules in the polar region. Based upon this assumption, a series of solvent mixtures were selected to represent the molecular environments, such as the hexane–acetone system (ε: 1.89 ~ 20.7) for the effect of the C=O group, the hexane–ethanol (ε: 1.89 ~ 24.5) for the protic effect in the hydrophobic

region, and ethanol–water (ε: 24.5 ~ 80.1) for the water-abundant region.

The deconvolution method will be explained in the next section. As the emission range of the Laurdan spectra in the lipid bilayer is broad enough to cover the entire range, it is possible to assign these four solvent systems to the multiple deconvolution curves as shown in the concept illustration (**Figure 2-8**).

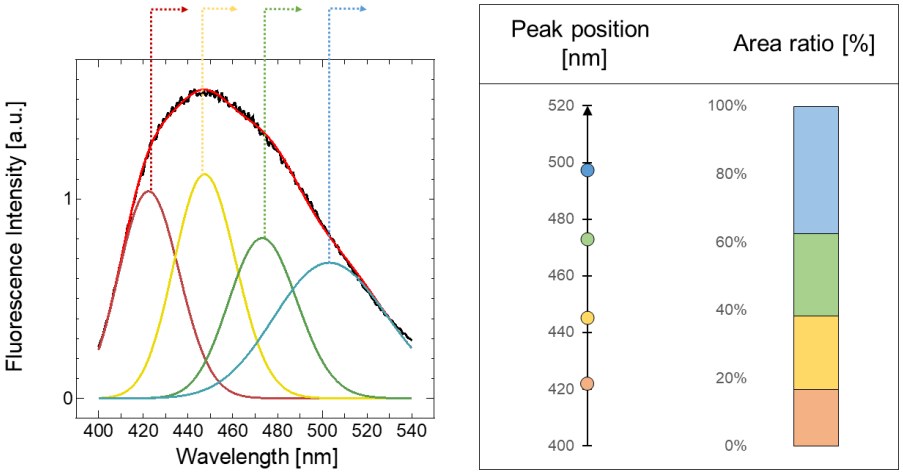

Figure 2-8 Concepts of deconvolution of Emission spectra of Laurdan. From the four deconvolution curves, peak positions of each curve and the integrated area ratios to the whole spectral area were calculated. The peak positions and the integrated area percentages obtained for each bilayer were pictured in the corresponding color with the deconvolution spectra.

3.6. Deconvolution analysis and the solvent model

Fitting parameters were carefully selected based on the considerations related to mixed solvent systems. First, a deconvolution analysis was performed as follows:

1. The second-derivative approach was performed to get the candidate peaks.
2. The deconvolution was performed using the asymmetric fitting equation following a previous report (Bacalum *et al.*, 2013).
3. Peaks with its relative peak areas less than 3 % were regarded as making no contributions to the entire spectrum and were eliminated.
4. Some candidate peaks were selected from those with the highest R^2 values.

Consequently, the fitting parameters for the solvent systems were obtained empirically, such as the number of components in the solvent system, the peak positions,

and the full width at half maximum (FWHM). The dielectric constants of each solvent system were measured using a dielectric probe kit (Model 85070C and a PNA-L Network Analyzer Model N5230C from Agilent Technologies, Santa Clara, CA, USA).

The deconvolution in the mixed system of hexane-acetone, hexane-ethanol, and ethanol–water were calculated with two fitting components. A comparison of the R^2 values of the single and second component deconvolutions are shown in **Figure 2-9**. According to the higher R^2 values of deconvolutions with two components, the results obtained with two-component deconvolution fitting were discussed. The peak position and the FWHM of each component are summarized in **Figure 2-10**. Each point corresponds to the plot shown in **Figure 2-11**.

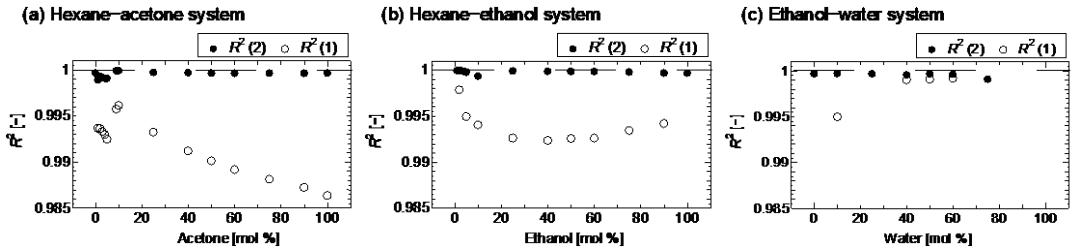

Figure 2-9 Comparison of the R^2 values in the **(a)** hexane-acetone system, **(b)** hexane-ethanol system, and **(c)** ethanol–water system. The R^2 values deconvoluted with two components and single components are represented as R^2 (2) and R^2 (1), as shown in the legend, respectively.

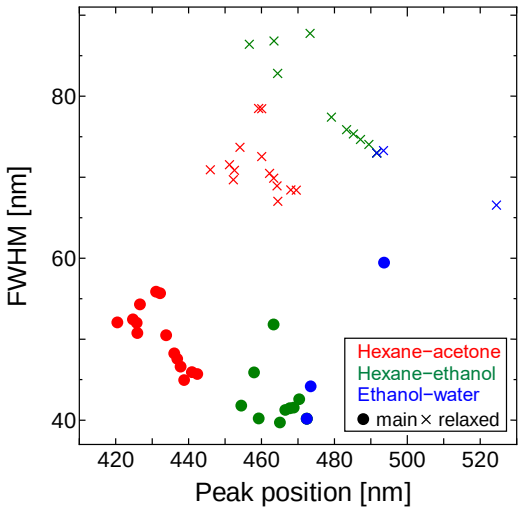

Figure 2-10 Summary of the correlation between peak position and FWHM for each deconvoluted peak. Red: hexane–acetone system; green: hexane–ethanol system; blue: ethanol–water system. The main deconvolution components are represented by filled circles, and the relaxed components were marked with crosses. Each point corresponds to the plot shown in **Figure 2-11**.

The correlation between the emission peak and the dielectric constants and emission peak positions were red-shifted in the following order: hexane–acetone system, hexane–ethanol system, and ethanol–water system (**Figure 2-11**). The shifts of peak position as a function of the dielectric constant indicated similar dependencies in any solvent system. The peak positions were stable with a wide range of dielectric constants. The two components found in a solvent system showed different FWHM values, and the one component with larger FWHM had a longer emission wavelength compared with another component (**Figure 2-10**). This broad and red-shifted component could be found even at a very low dielectric constant ($\varepsilon < 5$), indicating that this component was in a relaxed state not only because of the solvent but also due to undefined environmental factors, such as heat, collision, and reorientation. Laurdan and Prodan have two excitation states in a homogeneous solvent system, as suggested by the existence of two lifetimes (Lakowicz *et al*., 1982a, 1982b; Rowe *et al*., 2008). Hence, the deconvolution with two components in a solvent system is consistent with previous finding (De Vequi-Suplicy *et al*., 2015).

The deconvolution of Laurdan spectra in the lipid bilayer was performed using the same procedure for solvent systems explained previously (**Figure 2-13**). In the ε region corresponding to the membrane interface, the correlations of the peak positions were observed; less than 440 nm for the nonpolar solvent, 440 ~ 460 nm for the polar aprotic, 460 ~ 480 nm for the polar protic with low ε, and greater than 480 nm for the polar protic with high ε, respectively. The values of peak position and FWHM observed in the solvent system serve as reference boundaries for the peak positions ($420 < \lambda < 540$ nm) and FWHM ($30 <$ FWHM < 90 nm), respectively (**Scheme 2-1**). FWHM values for the deconvolution results in lipid bilayers are shown in **Figure 2-12**. These results suggest that the deconvoluted components of Laurdan spectra in lipid bilayers can be assigned to those in solvent systems.

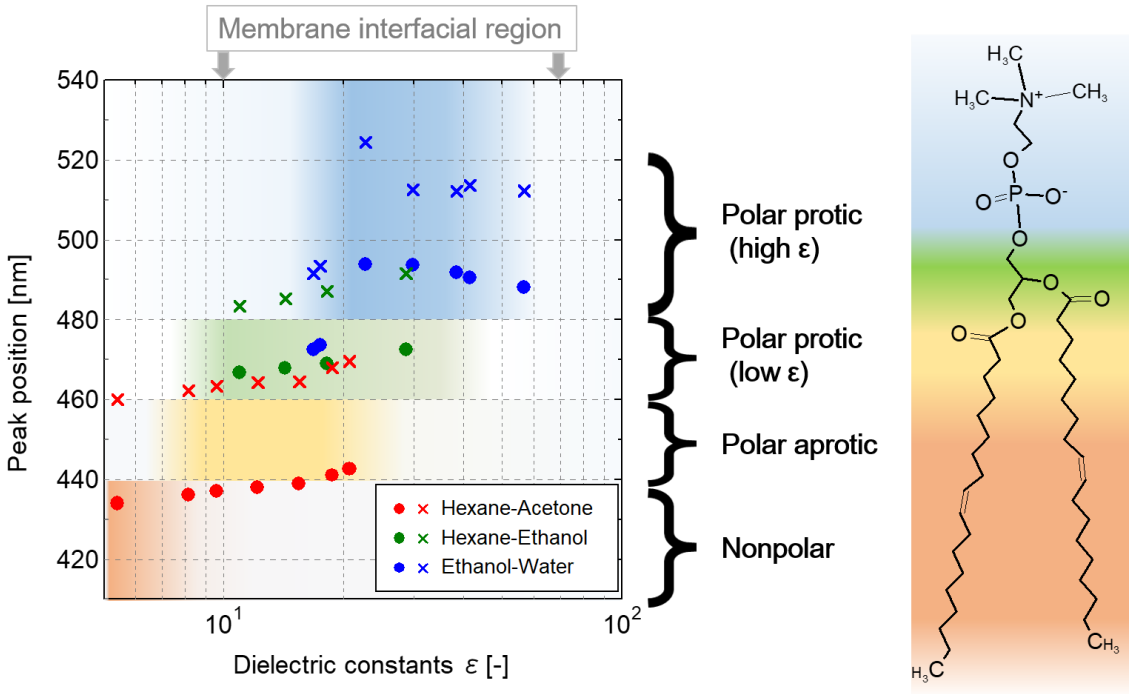

Figure 2-11 The correlation between the dielectric constants and the deconvoluted peak position. Red: hexane–acetone system; green: hexane–ethanol system; blue: ethanol–water system. The main deconvolution components are represented by filled circles, and the relaxed components are marked with crosses. The dielectric constants were measured using a dielectric probe kit. The interfacial region of the membrane was colored in the corresponding ε values (ε; 10 ~ 70), as reported previously (Cevc, 1990). The right figure represents the corresponding location of the dielectric constants for DOPC according to the schematic diagram for egg PC (Coster *et al.*, 1996).

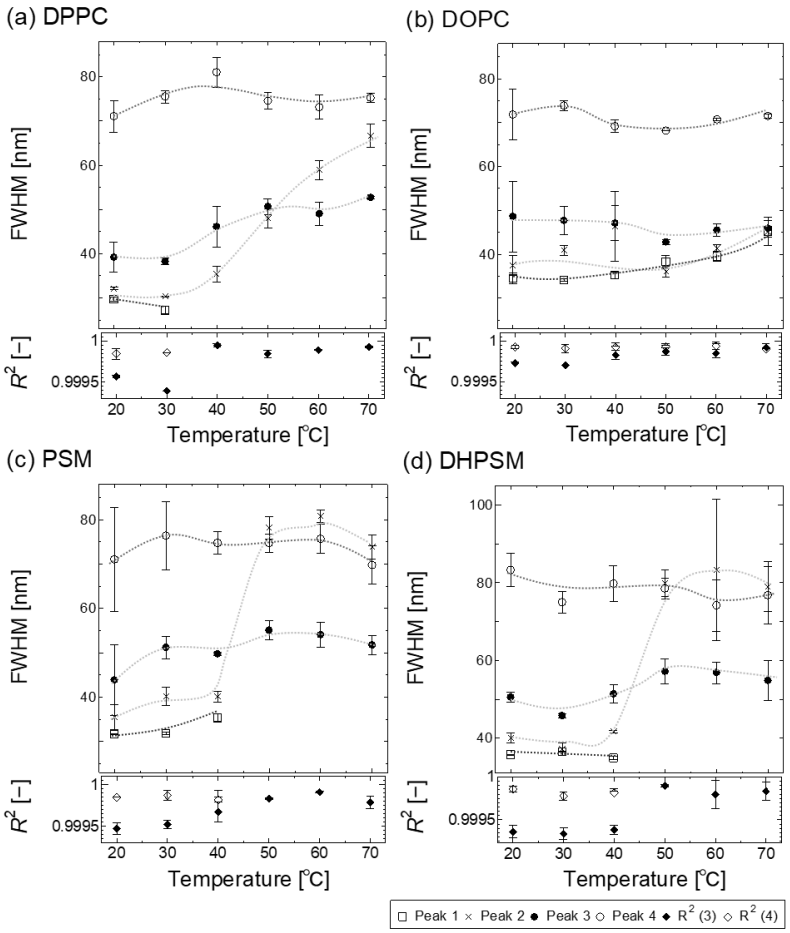

Figure 2-12 FWHM of deconvolution results in lipid bilayers: **(a)** DPPC, **(b)** DOPC, **(c)** PSM, and **(d)** DHPSM. Each peak corresponds to the components of the nonpolar (Peak 1, open square), the polar aprotic (Peak 2, cross), the polar protic with low ε (Peak 3, filled circle), and the polar protic with high ε (Peak 4, open circle), respectively. The R^2 values are shown in each bottom panel. Solid diamonds represent R^2 values analyzed with three deconvolution curves, and open diamonds represent those analyzed with four curves, respectively. Error bars represent SEM.

The number of components was changed from four to three when the R^2 value of the deconvolution with three components reached the value of the deconvolution with four components in the trial. Moreover, the amplitude of the first component located at the shorter wavelength was small to negligible. Most of the obtained spectra showed that the value of the asymmetry at half-maximum was approximately 1, which indicates that most of the deconvolution spectra were nearly symmetrical. Whole procedure for the deconvolution analysis is summarized in **Scheme 2-1**.

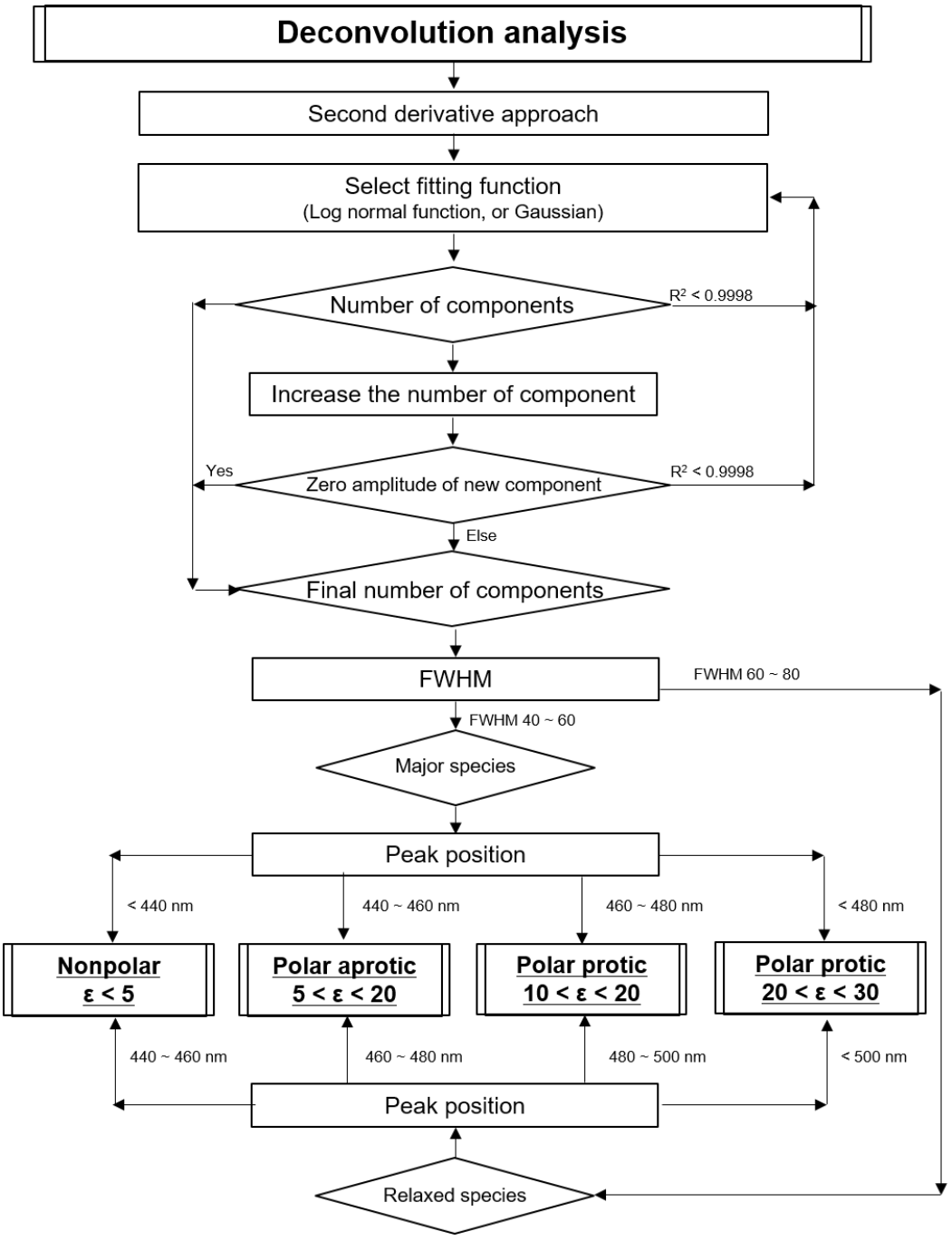

Scheme 2-1 Deconvolution analysis procedure.

3.6.1. Implication of deconvolution results in lipid bilayer

Figure 2-13 shows the peak positions and the area ratios obtained from the four deconvolution curves. Based on the solvent models, they can be classified into four groups. In the DPPC, PSM, and DHPSM bilayers, the most blue-shifted peak at approximately 420 nm disappeared during the phase transition. This peak originates from Laurdan existing in the nonpolar region (i.e., a tightly packed alignment or hydrogen bond interactions could prevent the solvation into fluorophores). Interestingly, in the loosely packed bilayers (such as DOPC bilayers), Laurdan also had a peak at 420 nm throughout the whole temperature range. This result seems contradictory. However, the Laurdan in the DOPC bilayer had a short lifetime (~ 2 ns) at an emission of 420 nm, suggesting that the blue-shifted components in DOPC bilayers are observable but they are energetically unfavorable because of collisional effects. As shown in the result of center of mass (**Figure 2-5**), DOPC and SM bilayers indicated at least two populations of fluorophores emitting at the shorter wavelengths with short and long lifetimes. In dynamic solvent environment, the quantum yield of Laurdan is relatively low, which means some of excited Laurdan could be immediately brought back to the ground state through the non-radiative pathway (Lakowicz, *et al.,* 1999). Compared with other bilayers, lower anisotropy values at blue-shifted region (at 440 nm) in DOPC bilayers were shown, which also suggests different fluorescence nature with high molecular motility in DOPC bilayers (**Figure 2-3**). Low viscosity makes the fluorescence lifetime shorter (Viard, *et al.,* 1997). Therefore, the blue-edge emission in DOPC bilayer are considered to be significant with short lifetime components in high mobility, on the other hand, the blue-edge mission in SM bilayers are expected to be significant with long lifetime component with high viscosity in nonpolar environment in the tightly-packed membrane state. The peak component with the largest emission peak (at around 500 nm) was corresponded to the polar protic solvent model with the highest ε value (**Figure 2-11**). In the solvent systems, the presence of more than 60% of water (over $\varepsilon \sim 30$) decreased the emission intensity while the blue-edge excitation increased. This means that Laurdan molecules experience unfavorable energy states in a high polar environment. Studies using theoretical calculation and an electrostatic force microscope reported dielectric constants around the polar region of $\varepsilon \sim 30$ (Coster *et al*., 1996; Gramse *et al*., 2013). Therefore, the local

environment with the highest ε value detected by Laurdan, was approximately 30, suggesting that Laurdan could be located in the shallower polar region of the membrane.

Compared with the deconvolution peaks in the DPPC bilayer, those in the PSM and DHPSM bilayers resulted in more red-shifted peaks similar to the result in the DOPC bilayer. In the DPPC bilayer, a shift in the peak position during the phase transition was observed; however, in the SM bilayers, the red-shifts were minor. These results indicate that the Laurdan molecules in SM bilayers could be distributed heterogeneously; one could be positioned in a significantly hydrated polar protic region similar to that in a DOPC bilayer, and the other could be placed in a less hydrated nonpolar region than that in a DPPC bilayer. The existence of the nonpolar components in SM bilayers was also confirmed by the increase in the blue-edge intensity of the excitation spectra at an emission of 435 nm (**Figure 2-6**).

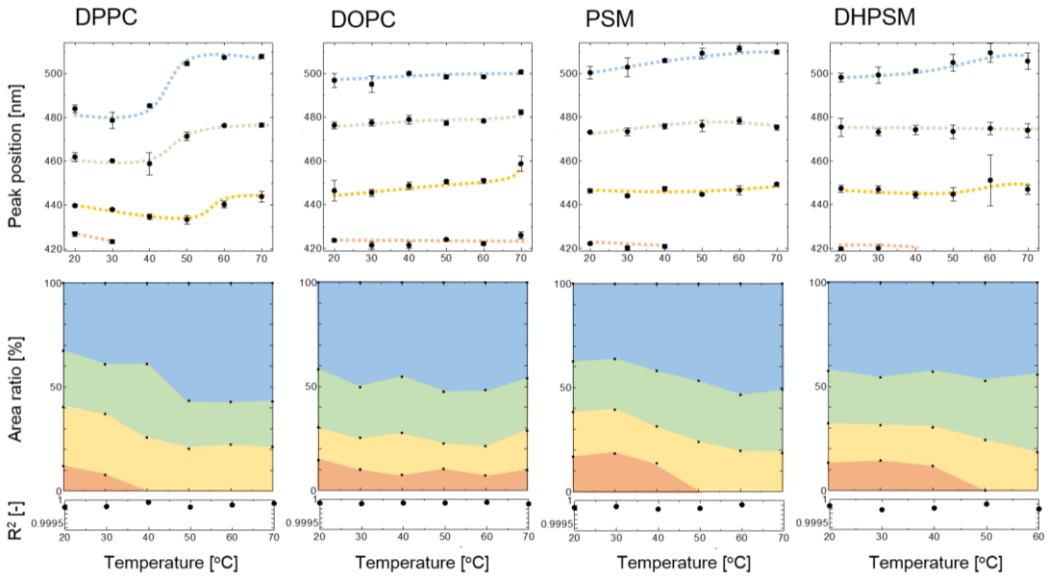

Figure 2-13 (*upper*) The peak positions of each deconvolution curve as a function of temperature, in DPPC, DOPC, PSM, and DHPSM bilayers. **(*lower*)** The transition of area ratios of each deconvolution curve as a function of temperature, in DPPC, DOPC, PSM, and DHPSM bilayers.

3.6.2. Hydrogen bonding network and interfacial hydration states in SMs

According to previous studies of PSM and DHPSM bilayers, DHPSM bilayers have stronger intermolecular hydrogen networks than PSM, which could be one of the possible reasons explaining the differences in their physicochemical properties in the bilayers, as mentioned previously ($T_{m,\ PSM}$; 41.2 ℃ < $T_{m,\ DHPSM}$; 47.7 ℃) (Ferguson-Yankey *et al*., 2000; Talbott *et al*., 2000). The immiscibility of the dihydro-stearoyl-SM and DOPC bilayers was attributed to strong intermolecular hydrogen bonding in dihydro-SM (Kinoshita *et al*., 2014). Therefore, the structure of the DHPSM bilayer is assumed to be highly ordered and less hydrated than that of the PSM bilayer. However, our results revealed highly hydrated properties for the DHPSM bilayer (**Figures 2-2**, **2-5**, **2-6**, and **2-7** as well as the predominant existence of nonpolar components in the PSM bilayer (**Figures 2-2**, **2-4**, **2-6**, and **2-13**), which appears to be contradictory to the expectations according to the previous observations (Ferguson-Yankey *et al*., 2000; Kinoshita *et al*., 2014; Talbott *et al*., 2000).

Yasuda *et al*. have suggested that DHPSM has a more flexible head group compared to PSM based on the quantum chemistry approach (Yasuda *et al*., 2016). They found that the properties of the 3OH group of DHPSM was different than that of PSM because the *trans* double bond in PSM could restrict the rotational motion of the C–C bond when the 3OH group is present. The intramolecular hydrogen bond between the 3OH group and phosphate oxygen is stronger in the PSM than in the DHPSM bilayer, as previously reported (Talbott *et al*., 2000). The restriction of the 3OH group in PSM influences strong intramolecular hydrogen bonds, and the flexible 3OH group in DHPSM has more opportunities to form hydrogen bonds with other functional groups. PSM has a kinked structure because of the strong intramolecular hydrogen bonds, which prevents PSM molecules from coming close to each other. Hence, the 2NH group of DHPSM exhibits stronger intermolecular interaction via the lipid–water–lipid link than in PSM (Talbott *et al*., 2000). As shown by the TEMPO-quenching experiments (**Figure 2-5**), DHPSM bilayers had more resistance to quenching compared with the PSM bilayer. This indicates that the strong intermolecular interaction in the DHPSM bilayer prevents the penetration of large molecules, such as the quencher molecules.

Thus, it is assumed that DHPSM has enhanced possibilities to form hydrogen bonds,

which can stabilize the water molecules around the interfacial region of the lipid bilayer. Based on the previous findings, the water exposure of lipids increases in the following order: PSM < DPPC < DHPSM, as measured from the fluorescence lifetime values of dansyl-PE under the collisional quenching effect of D_2O (Nyholm *et al*., 2003a). This also explains the highly dielectric environment at the interface of the DHPSM bilayer and the low accessibility of water into the PSM bilayer.

3.6.3. Plausible model of hydration properties in PC and SM bilayers.

A brief model of the membrane hydration and different populations of Laurdan below T_m is illustrated in **Figure 2-14**. Laurdan has different solvent properties depending on the emission wavelength. Based on our findings, it is expected that Laurdan with longer emission wavelengths is located in a shallower position in the bilayer membrane. The red-edge emission components in the SM bilayers indicate a polar protic environment. It seems that the specific properties of sphingolipids have hydrogen acceptor and donor impacts on hydration behavior. Highly hydrated states were observed especially in the DHPSM bilayer. The ability of the DHPSM bilayer to retain water molecules is due to the strong intermolecular hydrogen bonds via water bridges. The kinked structure of PSM makes it difficult for intermolecular hydrogen bonds to form with water molecules compared with DHPSM, which also explains the greater number of nonpolar components in the PSM bilayer. Generally, the dipole moment of the lipid head group derived from the zwitterionic part of the PC head group is aligned almost in parallel to the horizontal direction of the bilayer (Büldt *et al*., 1979; Gally *et al*., 1975; Griffin *et al*., 1978). It is therefore expected that the Laurdan in the DPPC bilayer will be located in a deeper place in the gel phase membrane. However, a blue-edge excitation spectrum at 435 nm was not found in DPPC (**Figure 2-5**), suggesting that it has a lesser nonpolar component compared to the SM bilayers. In the DOPC bilayers, the blue-edge emission component could be unfavorable with short lifetime due to surrounding high collisional effects. The long lifetime component at the blue-edge emission in DOPC bilayer is also existence, hence, both short and long lifetime species are illustrated. In sphingomyelin molecules, the contribution of long lifetime was significant compared with short lifetime at the blue-edge emission, thus, the long lifetime species was illustrated as the nonpolar component.

Their hydrogen bond donor/acceptor groups could allow the Laurdan incorporated into much deeper place without solvent waters, resulted in the deconvolution peak components of 420 nm (nonpolar environment). Such a hydrophobic environment in sphingolipids may attribute to a high affinity for hydrophobic cholesterol molecules. Though these are plausible models, the unique approach in this study provides novel insights into the multiple membrane polarity of SM bilayers, which leads us to a deeper understanding of intermolecular lipid interactions and membrane surface hydration.

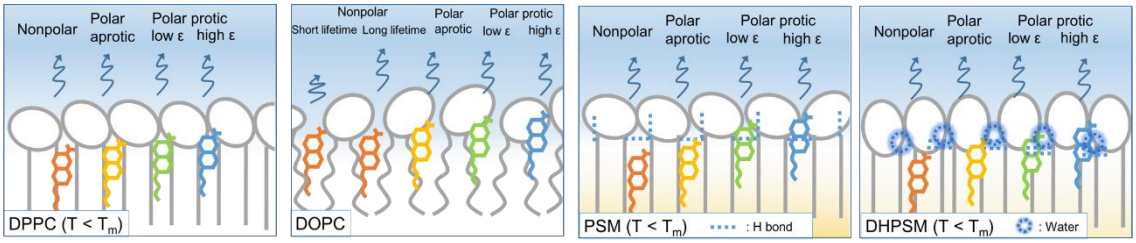

Figure 2-14 Hydration and the molecular model relation between lipid and Laurdan in DPPC, DOPC, PSM, and DHPSM bilayers. Lipids are illustrated in the color of gray. The colors of the Laurdan are illustrated with the corresponding color in **Figure 2-13**; orange for the nonpolar, yellow for the polar aprotic, green for the polar protic with low ε, blue for the polar protic with high ε.

4. Summary

The emission properties of a solvent-sensitive fluorescence probe, Laurdan, were evaluated in lipid bilayer systems composed of the sphingolipids (PSM and DHPSM) and the glycerophospholipids (DPPC and DOPC). The fluorescence properties of Laurdan in sphingolipids indicated multiple excited states according to the results obtained from the emission spectra, fluorescence anisotropy, and the center-of-mass spectra during the decay time. Deconvolution of the Laurdan emission spectra into four components based on the solvent model enabled us to identify the varieties of hydration and the configurational states derived from intermolecular hydrogen bonding in sphingolipids. Sphingolipids showed specific, interfacial hydration properties stemming from their intra- and intermolecular hydrogen bonds. Particularly, the Laurdan in DHPSM revealed more hydrated properties compared to PSM, even though DHPSM has a higher T_m than PSM. Since DHPSM forms hydrogen bonds with water molecules (in 2NH configurational functional groups), the interfacial region of the DHPSM bilayer was expected to be in a highly polar environment. The careful analysis of Laurdan through the deconvolution of emission spectra into four components in this study provides important insights for understanding the multiple polarity at the membrane interface.

Chapter 3

Lipid-Surrounding Water Molecules

Probed by Time-Resolved Emission Spectra of Laurdan

1. Introduction

Previous reports have proposed the classification of water molecules that hydrate the lipid bilayer with the group of water molecules directly bound to the lipid molecules known as the first hydration shell (Alarcón *et al*., 2016; Israelachvili, 1985; Laage *et al*., 2017). According to studies using nuclear magnetic resonance and neutron scattering, additional water molecules surround the polar head group. The water population, which could be affected relatively easily by surface pressure in the presence of amino acids and proteins, is called the second shell. Water molecules hydrating the lipid molecules can form additional hydrogen bonds with other water molecules (Disalvo *et al*., 2013; Morita *et al*., 2003). The water molecules in the second shell can be easily excluded by interactions with other biomolecules, and this mobility (degree of freedom) might affect the enzymatic function and penetration of various chemical compounds. As described in these reports, it is important to consider the contribution of water activity at the membrane surface in a molecular-level.

Laurdan, a solvent-sensitive fluorescence molecule studied in Chapter 2, is commonly used to evaluate the hydration state of lipid bilayers. The generalized polarization (*GP*) value is widely used to assess membrane polarity as follows:

$$GP = (I_B - I_R)/(I_B + I_R) \quad \text{(Eq. 3-1)}$$

where I_B is the intensity of the representative blue-shifted emission band and I_R is the intensity of the red-shifted band. In the previous chapter, it is investigated that Laurdan can adopt multiple excited states, and the assignment of the two components is only tentative when described by only the position of the peak. If multiple components are present, *GP* analysis could lead to the loss of information derived from other components, as the *GP* values consider only two components. To overcome this disadvantage, the

deconvolution of emission spectra (in Gaussian and lognormal) and spectral phasor analysis have been performed (Bacalum *et al*., 2013; Malacrida *et al*., 2016; De Vequi-Suplicy *et al*., 2015). However, the obtained information was averaged data and further investigation was required for the comprehension of dynamic hydration states at the lipid membrane.

Fluorescence lifetime analysis can be used to understand the subtle changes in the fluorescence properties (Lakowicz, 1999). Fluorophores excited with a pulse laser on the femtosecond timescale emit fluorescence derived from corresponding excitation states on the nanoseconds lifetime scale (Lakowicz, 1999). Because of the rapid relaxation of water molecules (picoseconds), each component with different lifetimes assigned from corresponding excitation states was already relaxed due to the surrounding environment before the fluorescence emission. Laurdan exhibits two major lifetimes expected from the relaxed and nonrelaxed states (De Vequi-Suplicy *et al*., 2006; Lúcio *et al*., 2010; Parasassi *et al*., 1986). The fluorophore relaxed due to surrounding solvents has a long lifetime because of its low quantum yield (Lakowicz, 1999). Components identified from these lifetimes are indicative of the different molecular environments in the system. Thus, the decomposition with fluorescence lifetimes is useful for evaluating the heterogenic properties of membrane systems. However, the assignment of the lifetimes and relaxation states is difficult. In 1,2-dimyristoyl-*sn*-glycero-3-phosphocholine (DMPC) vesicles, the fluorescence lifetime of Laurdan becomes shorter as a function of temperature because collisional molecular movements promote the nonradiative emission path, although the long lifetime components were assigned to relaxed molecules (De Vequi-Suplicy *et al*., 2013). As observed in the time-resolved emission spectra (TRES) of Patman, another Laurdan derivative, DOPC exhibits a shorter lifetime than that of DPPC because the water relaxation is more rapid (Lakowicz *et al*., 1984). In some membrane systems, longer lifetimes can be assigned as a relaxation state, and in other situations, shorter lifetimes are also regarded as indicative of the relaxed states due to collisional quenching effects. These conclusions were derived from the competitive properties between the relaxation time and fluorescence decay (Lakowicz, 1999; Lakowicz *et al*., 1984). In a system with rapid collisional quenching effects, the fluorophore will exhibit emissions with negligible solvent relaxation effects (Lakowicz, 1999; Valeur, 2001). Therefore, it is not always

possible to assign relaxed or nonrelaxed molecular states from the two-lifetime components (**Figure 3-1**).

In this chapter, the temporal and spatial hydration behaviors at the lipid bilayer interface were evaluated based on dynamic motion in a molecular level. A novel fluorescence analysis technique was used, that is the decomposition of the time-resolved emission spectra (TRES) of Laurdan. Each lifetime component was extracted from the TRES, and the deconvolution was performed following a method described in a previous chapter. Information obtained from lifetime-based and emission peak-based fluorescence properties were summarized based on the lifetime (τ) and peak position (λ) (τ vs λ plot). This τ vs λ plot simplifies the analysis of Laurdan fluorescence by simultaneously evaluating the effects of the hydration and collisional quenching behavior of the water molecules in the lipid bilayer. Based on the hypothetical calculations of the water population per lipid molecule, the specific hydration behavior at the lipid bilayer interface in binary systems is also discussed.

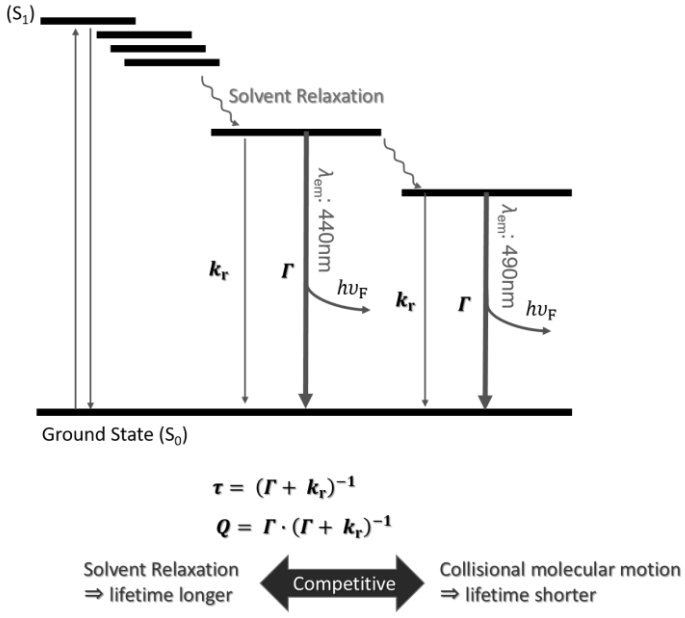

Figure 3-1 Jablonski diagram of fluorescence emission pathways of Laurdan. τ is the lifetime of fluorophore; k_r is the nonradiative constant, which loses the energy in nonradiative pathway. Q is a quantum yield; Γ is the emission rate constant, which can be converted into the emission pathway; υ_F is the frequency at which the fluorescence emission occurs. The definition of lifetime and quantum yield are described in the figure.

2. Materials and Methods

2.1. Materials

All phospholipids (1-palmitoyl-2-palmitoyl-*sn*-glycero-3-phosphocholine (DPPC), and 1-oleoyl-2-oleoyl-*sn*-glycero-3-phosphocholine (DOPC)) and egg yolk SM were purchased from Avanti Polar Lipids (Alabaster, AL, USA). PSM was purified from egg yolk SM, as described previously (Nyholm *et al*., 2003a). PSM was hydrogenated to yield DHPSM, as previously reported (Ramstedt *et al.*, 1999). The purity of the sphingomyelins was confirmed by mass spectrometry. Laurdan was purchased from Sigma Aldrich (St. Louis, MO, USA). Other chemicals were obtained from FUJIFILM Wako Pure Chemical Corporation (Osaka, Japan) and used without further purification.

2.2. Preparations of the Lipid Vesicles

All lipids were dissolved in methanol with Laurdan in a glass tube, and methanol was completely evaporated under a nitrogen flow at 40 ℃. The dried lipid film was hydrated with pure water and incubated for 50 mins at 65 ℃. After the incubation, samples were sonicated by Brasonic 2510 (Branson Ultrasonics, CT, USA) for 5 mins at 65 ℃. Large unilamellar vesicles were prepared with a lipid extrusion device using 100 nm pore-size film (Liposofast; Avestin Inc., Ottawa, ON, Canada). Samples were cooled to room temperature before measuring.

2.3. Time-Resolved Emission Spectrum (TRES) measurements

The TRES of Laurdan was measured using the FluoTime 200 from PicoQuant (Rudower Chaussee, Berlin, Germany). In all measurements, the total concentrations of lipids and Laurdan were 100 μM and 1 μM, respectively. For the excitation of the samples, a diode laser with a light source of 378 nm was used. Emission decays were obtained from 400 to 540 nm in 10 nm steps with a 64-picosecond resolution. The acquisition time was 150 seconds for each emission wavelength. The cuvette temperature was controlled by a Peltier system, and the instrumental response function was taken with pure water in the Quartz cell. Obtained data were analyzed using the FluoFit Pro software also from PicoQuant (Rudower Chaussee, Berlin, Germany). Global reconvolution fitting was

performed for all ranges of collected emission wavelengths and were well fitted with the double exponential fitting equation as follows (Lakowicz, 1999):

$$I(t) = \int_{-\infty}^{t} \mathrm{IRF}(t') \sum_{i=1}^{n} A_i \mathrm{e}^{-\frac{t-t'}{\tau_i}} \mathrm{d}t' \qquad \text{(Eq. 3-2)}$$

where $I(t)$ is the intensity at decay time t, n is the number of components (herein, n = 2), and A_i is the amplitude in counts at time zero. Following the fitting and the determination of the lifetimes, the global TRES was extracted for each lifetime component, wherein the amplitude of each lifetime component in the experimental wavelength range was plotted as a function of wavelength as TRES (**Figure 3-2**).

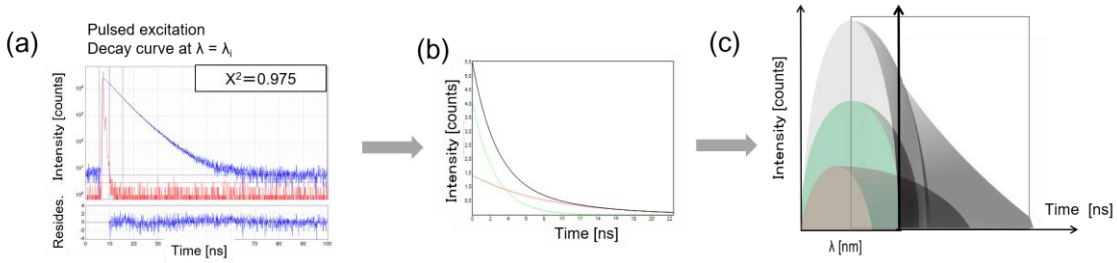

Figure 3-2 In the experimental procedure, the fluorescence decay curve **(a)** was decomposed of a double exponential fitting curves **(b)**. The integration of the whole spectral range comprise the spectrum **(c)**. The concept of the experimental data obtained from TRES is drawn in gray color, and short and long lifetime components are depicted in green and red colors, respectively.

2.4. Deconvolution of Spectra

Both the shorter and longer lifetime components, obtained from the TRES of Laurdan, were decomposed using the fitting software PeakFit (Systat Software, Inc., San Jose, CA, USA). According to the previous report (Bacalum *et al.*, 2013), the deconvolution was performed with a lognormal amplitude function as follows:

$$\mathrm{y} = a_0 \exp\left(-\frac{1}{2}\left(\frac{\ln\frac{x}{a_1}}{a_2}\right)^2\right) \qquad \text{(Eq. 3-3)}$$

where a_0 is the amplitude and a_1 and a_2 are the center ($\neq$ 0) and width (> 0) of the fitting curve, respectively. The number of fitting curves was varied from one to four, to satisfy the coefficient of determination value $R^2 \geq 0.9$. The integral area and peak position were collected from the obtained results.

3. Results and Discussion

3.1. Comparison of the TRES of Laurdan in PC and PSM bilayer systems

TRES obtained in this study was analyzed using the global fitting analysis mode in the FluoFit software. The fluorescence decay curve of Laurdan in the lipid bilayer could be described using a double exponential fitting equation (for details, see **Figure 3-2**), suggesting that the emission of Laurdan in bilayer systems can be derived from two lifetime components. TRES of Laurdan was composed of shorter (filled circles) and longer (open circles) lifetime components (**Figure 3-3**). The Laurdan in DPPC bilayers exhibited both lifetime components with peaks at approximately 440 nm at 20 ℃ (**Figure 3-3 (a)**). In the DOPC bilayer, the TRES of Laurdan showed two major peaks: a less relaxed state (at 440 nm) for the short lifetime component and a highly relaxed state (490 nm) for the long lifetime component (**Figure 3-3 (b)**). As shown in the Jablonski diagrams (**Figure 3-4**), for the DPPC bilayers, a single excited state is expected with different lifetimes. In the DOPC bilayers, Laurdan has two excitation energy states: less relaxed and highly relaxed states. This is of interest that DOPC bilayers could exhibit less relaxed states because the DOPC bilayers are well known as loosely-packed fluidic membranes ($T_{m,\ DOPC}$: -16.5 ℃) (Ulrich *et al*., 1994). The shift in the emission peak could be caused by solvent relaxation (Józefowicz *et al*., 2005), and the difference in the fluorescence lifetime could be due to molecular mobility (viscosity). The collision effect from surrounding water molecules shortens the fluorescence lifetime, while the hydration (solvation) by water molecules extends the fluorescence lifetime. Taking the short lifetime component of the DOPC bilayers as an example, it is difficult to isolate the contributions of relaxation and mobility (collision). Peak positions in TRES found in the DOPC and DPPC bilayers are also consistent with those found in steady-state emission spectra (Parasassi *et al*., 1990).

In comparison with glycerolipid bilayers, the TRES of Laurdan in the PSM bilayers showed unique emission properties (**Figure 3-3 (c)**). The spectral shape of the short lifetime component contained multiple components, which could be furthermore decomposed into two peaks, approximately at 420 and 460 nm (**Figure 3-4 (c)**). The multiple peaks obtained in the PSM bilayers could be relevant to multiple excitation energy states, which will reflect the difference in the hydration state of Laurdan in PSM

bilayers. The longer lifetime component in the PSM bilayers (7.77 ns, λ_{em} = 440 nm) was similar to that in the DPPC bilayers (7.76 ns, λ_{em} = 440 nm). On the basis that the less collisional situation extends the lifetime, the 440-nm emission peaks with 7.76-7.77-ns lifetime could be evident to a typical Laurdan in gel phase bilayers. The blue-shifted emission component (420 nm) in the PSM bilayers could be caused by the strong intermolecular H-bonds of PSM that stabilizes the motion of Laurdan (Kinoshita *et al*., 2014; Nyholm *et al*., 2003b; Slotte, 2016), resulting in a rapid transition from an exited state to a ground state. The red-shifted emission peak (460 nm) in PSM bilayers indicates that the PSM bilayers provide a unique hydrophobic environment, which is neither categorized as a gel phase nor a fluid phase. It is concluded that Global TRES analysis is a powerful tool to investigate the detailed environmental information around Laurdan in bilayer systems. This method can be applied to understand more precious information about the membrane hydration; however, the presence of water around Laurdan provides a competitive effect, such as collisional energy loss (mainly for lifetime (τ)) and a relaxation state (mainly for peak position (λ)), which makes the results complicated.

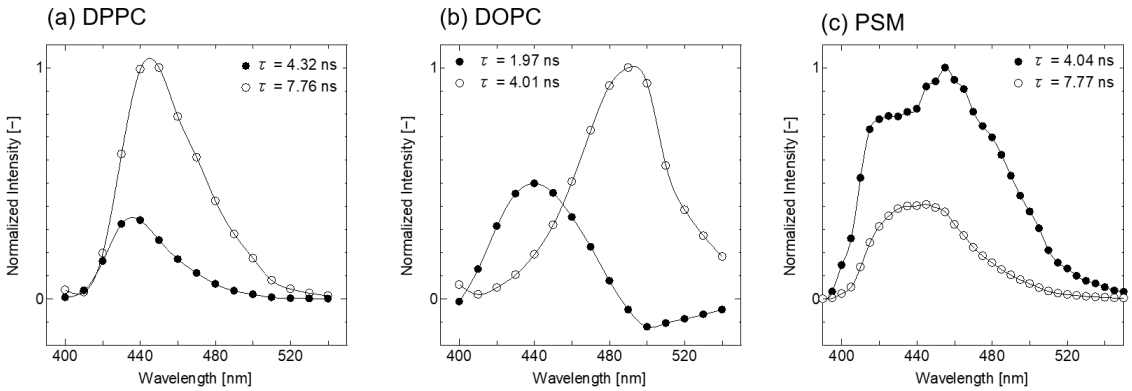

Figure 3-3 TRES of Laurdan in **(a)** DPPC, **(b)** DOPC, and **(c)** PSM bilayers. Shorter and longer lifetime components are depicted with filled circles and open circles, respectively. The lifetimes were 4.32 and 7.76 ns for DPPC bilayers, 1.97 and 4.01 ns for DOPC bilayers, and 4.04 and 7.77 ns for PSM.

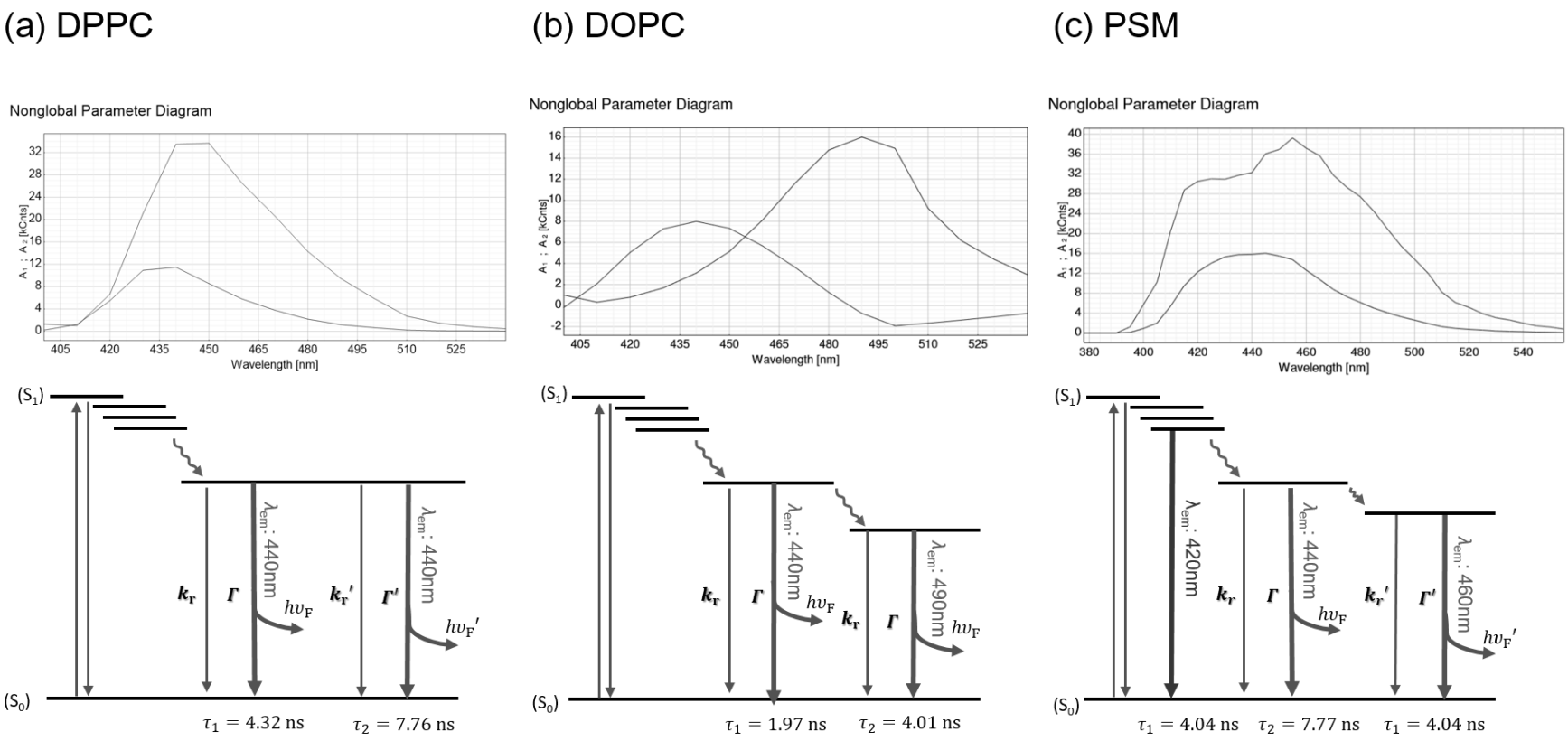

Figure 3-4 Jablonski diagram of Laurdan in **(a)** DPPC, **(b)** DOPC, and **(c)** PSM bilayers. The spectra were the raw data obtained from the global fitting analysis in Fluofit pro software.

3.2. Distributions of τ and λ values in pure lipid bilayers

The *GP* analysis is quite popular in the steady-state emission fluorescence of Laurdan in bilayers (Celli *et al*., 2010; Parasassi *et al*., 1991, 1997; Sanchez *et al*., 2012), wherein the emission peak intensities from 440 and 490 nm are generalized to identify the phase states and phase transition behaviors. The emission peak position of Laurdan strongly reflects the degree of water solvation. In recent works, the deconvolution of Laurdan emission spectrum and the area fraction analysis has helped researchers to successfully investigate the polar environment at the membranes composed of amphiphiles (Iwasaki *et al*., 2017; Suga *et al*., 2018). Thus, the hydration property of lipid bilayers could depend on the lifetime (τ) and peak position (λ). The λ-dependent deconvolution of Laurdan TRES was carried out using the PeakFit software. **Figure 3-5 (a)** shows the deconvoluted TRES of Laurdan in DPPC bilayers at 20 ℃. The emission spectrum of Laurdan was well fitted using the lognormal function (Bacalum *et al*., 2013; Parasassi *et al*., 1997), resulting in the emission peak positions varying from 420 to 490 nm. The longer lifetime component was decomposed into three individual components, wherein the components at 441 and 464 nm were dominant with the integrated area ratio of 42% and 22%, respectively (**Table 3-1**). For a shorter lifetime component, the deconvolution resulted in a peak at 435 nm and in a red-shifted one at 462 nm. The correlation of τ and λ is shown in **Figure 3-5 (b)**, with each integrated area ratio described according to the size of the bubble. As shown in the bubble chart, the distribution of λ and τ values indicates the variations of local environments for Laurdan in each bilayer.

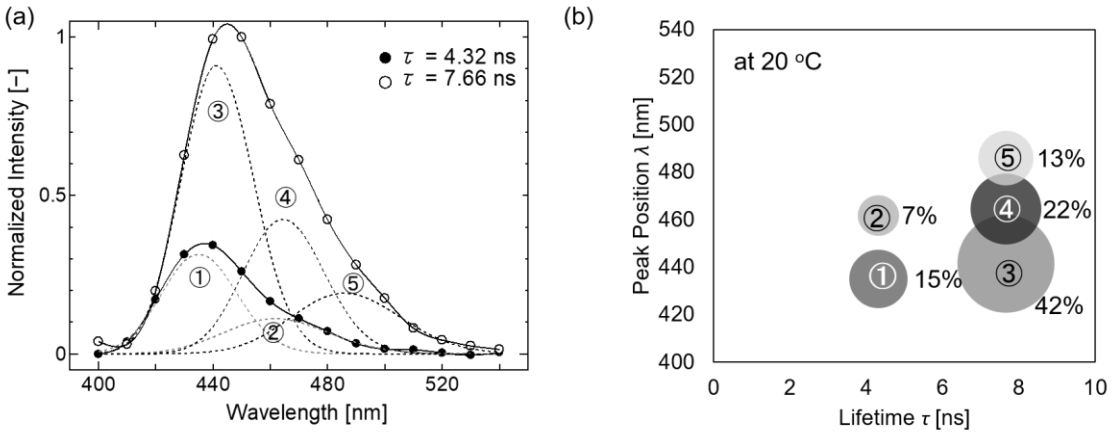

Figure 3-5 (a) Deconvolution analysis of the TRES of Laurdan in DPPC bilayers at 20 ℃ and **(b)** the distribution of deconvolution components in the τ vs λ plot. Raw data are depicted with a solid line with marks, filled and open circles for short and long lifetime components, respectively. The deconvolution curve is illustrated with a broken line. Deconvolution was performed using the lognormal function, as described in Eq. 3-3, and the area ratio was calculated from the ratio of the integrated fitting curve shown in **(a)**. Detailed results obtained from the deconvolution fitting are shown in **Table 3-1**.

Table 3-1 The results from the deconvolution of TRES

Peak	τ [ns]	λ [nm]	Area [%]
①	4.32 ± 0.107	435	15.1
②	4.32 ± 0.107	462	7.41
③	7.76 ± 0.026	441	42.1
④	7.76 ± 0.026	464	22.0
⑤	7.76 ± 0.026	486	13.4

Particularly in the emission spectrum of Laurdan, the λ value is relevant to the phase state. To evaluate the phase transition, the τ vs λ plot, the deconvoluted TRES of Laurdan was analyzed in DPPC bilayers at different temperatures (**Figure 3-6**). At temperatures above the phase transition temperature ($T_{m,\ DPPC}$: 41 ℃), the shorter lifetime components with red-shifted peak positions were dominant. This reveals that the DPPC bilayer in the fluid phase is more hydrated, wherein the contribution of collision water become significant as compared to the gel phase.

In the DOPC bilayers, the dominant lifetime and peak position were 2.7–4.0 ns

and 484–491 nm, respectively (**Figure 3-7**). The short lifetime component (filled circles) in the DOPC bilayers at lower temperatures showed a blue-shifted spectral feature. In the whole experimental temperature range, the DOPC bilayers are in fluid phases, which exhibit more hydrophilic membrane properties based on steady-state Laurdan analysis (Parasassi *et al*., 1990, 1991, 1993). Although blue-shifted (hydrophobic) components were observed, the lifetime values of the major components in the deconvoluted TRES in the DOPC bilayers were shorter than the lifetime values of the gel phase (DPPC, $T < T_m$). Based on these findings, this region with short lifetimes and longer wavelength peaks is indicative of the membrane in the fluid phase (liquid crystalline phase).

In PSM (T_m: 41 ℃) bilayers, the dominant lifetime and peak position were observed in 3.7–4.0 ns and 437–450 nm, respectively, at temperatures below T_m (**Figure 3-8**). The distributions of τ and λ values in the PSM bilayers were similar to those in the DPPC bilayers. The peak positions of the major component in the DPPC and PSM bilayers were similar, but the lifetime in PSM bilayers decreased compared with that in DPPC bilayers. This suggests the more hydrated property of the PSM bilayers, possibly due to the intermolecular hydrogen bond between PSM molecules. In the PSM bilayers, the distributions contained two distinct components: a blue-shifted peak at approximately 420 nm and a red-shifted peak at approximately 490 nm. In the previous study reporting the steady-state fluorescence properties of Laurdan in SM bilayers, the emission spectra exhibited broader spectral features, suggesting that multiple excited states were affected by environmental factors, such as water population and hydrogen bonds (Nyholm *et al*., 2003). Our results that SM bilayers could have multiple excited states are consistent with the previous observations, indicating that the significant influences of hydrogen bonding induced plural relaxed states by water molecules in PSM bilayer.

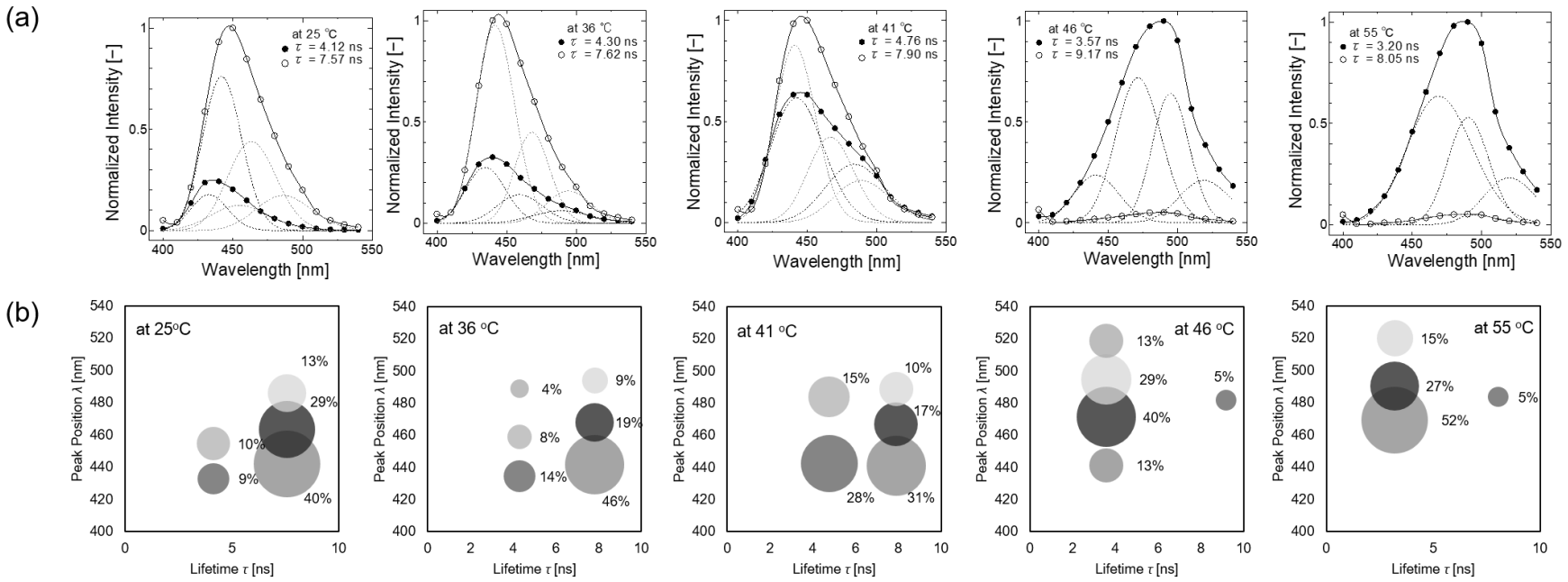

Figure 3-6 (a) TRES of Laurdan in DPPC bilayers. The lifetimes were represented in the figure. The solid line and dotted line represent the obtained TRES and deconvoluted peaks, respectively. Shorter and longer lifetime components were each depicted with filled and open circles, respectively. **(b)** The τ vs λ plot for the deconvoluted TRES of Laurdan in DPPC bilayers. The integrated area ratio of each component was reflected in the size of the bubbles.

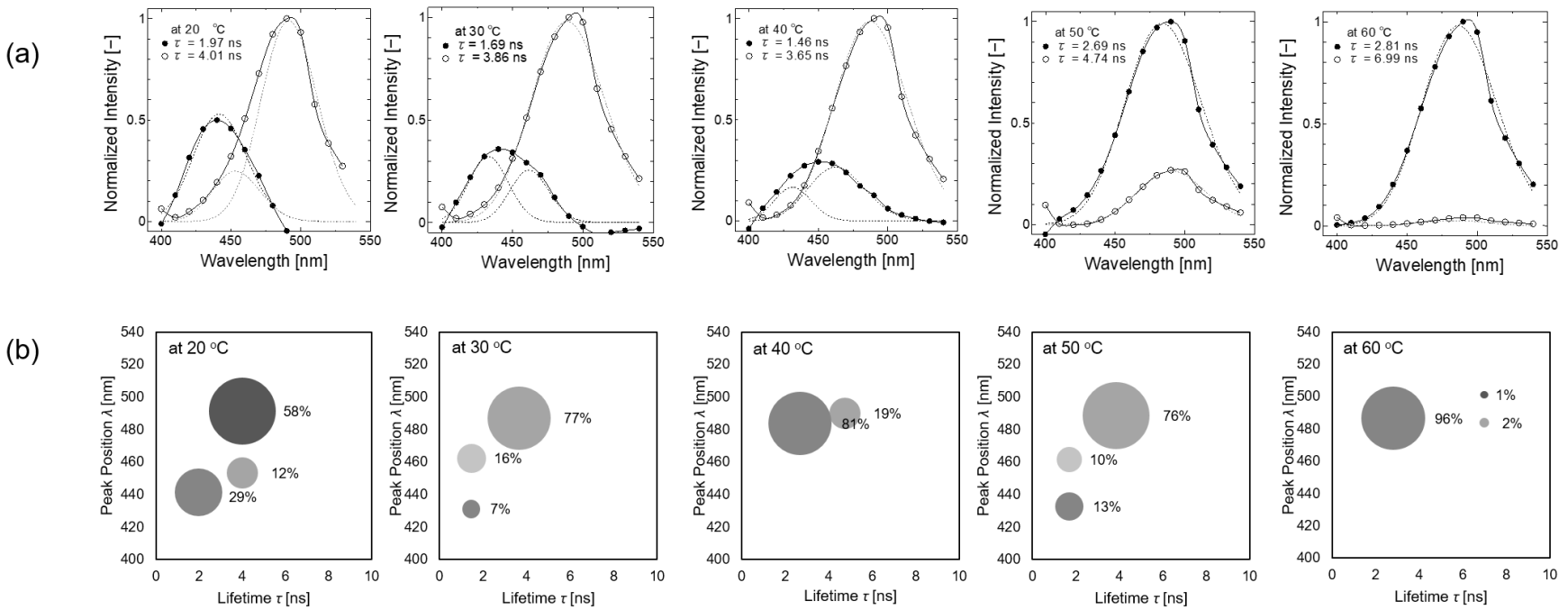

Figure 3-7 (a) TRES of Laurdan in DOPC bilayers. The lifetimes were represented in the figure. The solid and dotted lines represent the obtained TRES and deconvoluted peaks, respectively. Shorter and longer lifetime components were each depicted with filled and open circles, respectively. **(b)** The τ vs λ plot for the deconvoluted TRES of Laurdan in DOPC bilayers. The integrated area ratio of each component was reflected in the size of the bubbles.

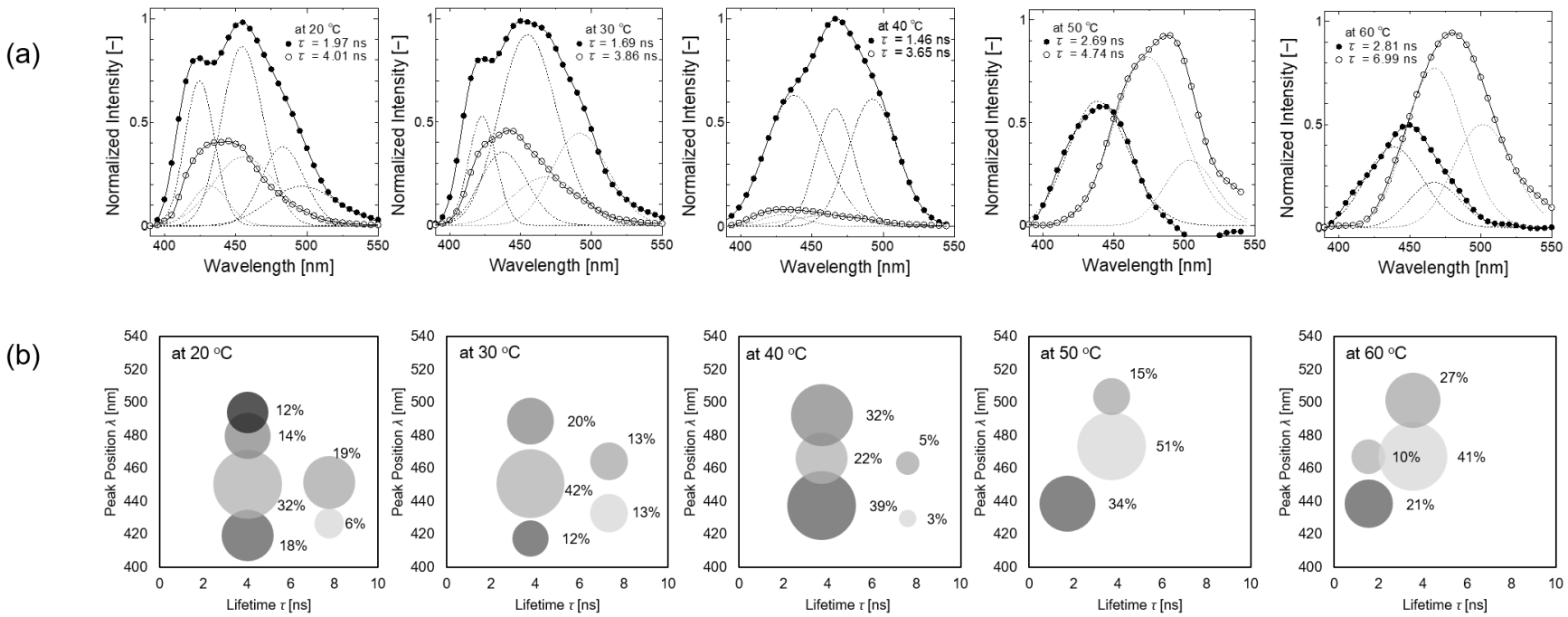

Figure 3-8 (a) TRES of Laurdan in PSM bilayers. The lifetimes were represented in the figure. The solid and dotted lines represent the obtained TRES and deconvoluted peaks, respectively. Shorter and longer lifetime components were each depicted with filled and open circles, respectively. **(b)** The τ vs λ plot for the deconvoluted TRES of Laurdan in PSM bilayers. The integrated area ratio of each component was reflected in the size of the bubbles.

3.3. Water mapping: Quantitative consideration for the number of hydration/collision water molecules associating with Laurdan

The factors that influence the fluorescence of Laurdan can be explained as follows: the solvation of water (i.e., hydration) and molecular mobility (i.e., collisional quenching effects). With regards to hydration, the emission peak was significantly affected by the degree of solvent relaxation. According to Parasssasi *et al.*, the water cavity around the Laurdan fluorophore can be calculated based on the Poisson distribution (Parasassi *et al*., 1997). Assuming the average number of hydration water molecules for Laurdan as *n*, the probability of the number of water molecules is 0.135 ($n = 0$), 0.270 ($n = 1$), 0.270 ($n = 2$), 0.203 ($n = 3$), 0.090 ($n = 4$), 0.031 ($n = 5$), and 0.020 ($n \geq 6$) (Parasassi *et al*., 1997). The Laurdan emission peak was observed at 400 nm, without hydration (De Vequi-Suplicy *et al*., 2015): thus, no solvent relaxed emission peak (no hydration water, $n = 0$) can be confirmed as $\lambda \sim 400$ nm. In our experiments, the deconvoluted TRES resulted in 4–6 peak positions. Based on bubble charts (**Figures 3-6**, **3-7**, and **3-8**), the distributions of λ values are classified into four groups: ~420–440, 440–460, 460–480, and >480 nm. These peak distributions were also corresponding to the steady-state fluorescence spectra of Laurdan (in Chapter 2). Shifts in the Laurdan emission peak could be dependent on the number of associating water molecules. Thus, the distribution of *n* values could be assigned as four states: 1, 2, 3, and ≥ 4. The average number of hydration water molecules for Laurdan in each bilayer can be calculated by considering the peak position (λ) and probability (area%).

The fluorescence lifetime can be defined using the fluorescence emission rate constant and the nonradiative constant (Lakowicz, 1999), revealing that the fluorescence lifetime can be shortened with the increasing collisional waters existing around chromophores. In addition, the mobility of Laurdan molecules can be resembled by the lipid acyl chain and molecular size. For example, the water molecules would contribute to the collisional effects due to their high diffusion constant compared to that of phospholipids ($D_{water} \sim 10^{-10}$ m^2/s > $D_{POPC} \sim 10^{-12}$ m^2/s) (Gaede *et al*., 2003; Volke *et al*., 1994). In the dynamic quenching process caused by water, the relation of the emission intensity and the concentration of the quencher can be defined using the Stern–Volmer equation (Lakowicz, 1999):

$$I_0/I = 1 + K_{SV}[Q] \quad \text{(Eq. 3-4)}$$

where I_0 and I represent the fluorescence intensity in the absence and presence of the quencher, respectively. K_{SV} is the Stern–Volmer constant, and $[Q]$ is the concentration of the quencher. The intensity ratio as a function of $[Q]$ exhibits a linear relation. Thus, Eq. 3-4 is described by the lifetime, shown as follows (Lakowicz, 1999):

$$I_0/I = \tau_0/\tau = 1 + k_q\tau_0[Q] \quad \text{(Eq. 3-5)}$$

$$K_{SV} = k_q\tau_0 \quad \text{(Eq. 3-6)}$$

where k_q is the bimolecular quenching constant, τ_0 is the fluorescence lifetime without the quencher, and τ is the lifetime in the presence of the quencher. For static quenching, the fluorophore can adopt a non-emission pathway by forming a complex with a quencher (Lakowicz *et al*., 1984):

$$I_0/I = [F]_{total}/[F] = ([F] + [Q])/[F] = 1 + k_a[Q] \quad \text{(Eq. 3-7)}$$

$$F + Q \rightarrow FQ, \quad k_a = \frac{[FQ]}{[F]+[Q]} \quad \text{(Eq. 3-8)}$$

where $[F]$ is the concentration of fluorescence molecules and k_a is the quenching constant for the static quenching. The quantum yield of Laurdan would decrease in a highly hydrated state and can be quenched by forming a molecular complex with water molecules. When both dynamic and static quenching occurs in a same system, the quenching effect can be defined as follows:

$$I_0/I = \tau_0/\tau = (1 + k_q\tau_0[Q])(1 + k_a[Q]) \quad \text{(Eq. 3-9)}$$

This model is plotted in **Figure 3-9 (a)**.

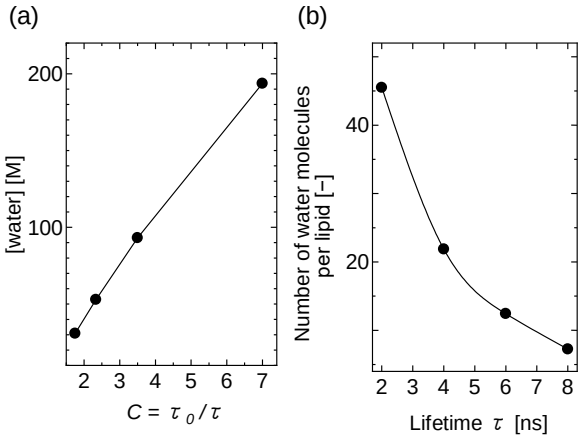

Figure 3-9 (a) Correlation model between the lifetime and the water concentration estimated from Eq. 3-9. **(b)** Correlation between the measured lifetimes and the number of water molecules working toward quenching. As a representative of lifetime, 2, 4, 6, and 8 ns were selected in the lifetime range observed in the experiments.

Based on the model described in Eq. 3-9, the correlation between the lifetime and quencher concentration (i.e., the relation between the lifetime and concentration of water molecules used for quenching) could be estimated. Based on these, the quenching water molecules could be easily distinguished as free water molecules in the bulk region. Herein, DPPC is selected as model lipid, because its size, diffusion constant, and molecular viscosity are well characterized (Alarcón *et al*., 2016; Marsh, 2010; Parasassi *et al*., 1992; Rifici *et al*., 2014; Viard *et al*., 1997). Kinetic parameters (k_q, τ_0, and k_a) are employed as reported. Considering the average volume per lipid head group (for DPPC in the gel phase, 0.397 nm^3) (Marsh, 2010), the number of water molecules associating with a lipid molecule was calculated (**Figure 3-9 (b)**). Especially for the short lifetime region (approximately 2 ns), the quenching water population was remarkable at 45.5 molecules per lipid molecule.

Accordingly, a model for a water map was finally established (**Figure 3-10**). The correlation between τ and the collisional water population is reflected in the *x*-axis (collision effect). The correlation between λ and the number of hydration water molecules is reflected in the *y*-axis (hydration effect). The assumptions used to generate the water map are briefly explained in **Figure 3-11 (a)**. The number of water molecules per lipid was determined for each distributed component based on the correlation of the experimental τ vs λ plot with the model water map (**Figure 3-11 (b)**). The number of water molecules was estimated using the area% derived from the deconvolution fitting.

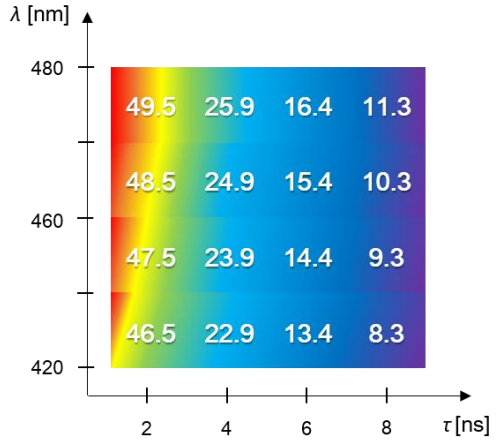

Figure 3-10 Model of the water map. The number written in each table is the number of water molecules per lipid. For the details of the model, please see **Figures 3-9** and **3-11**.

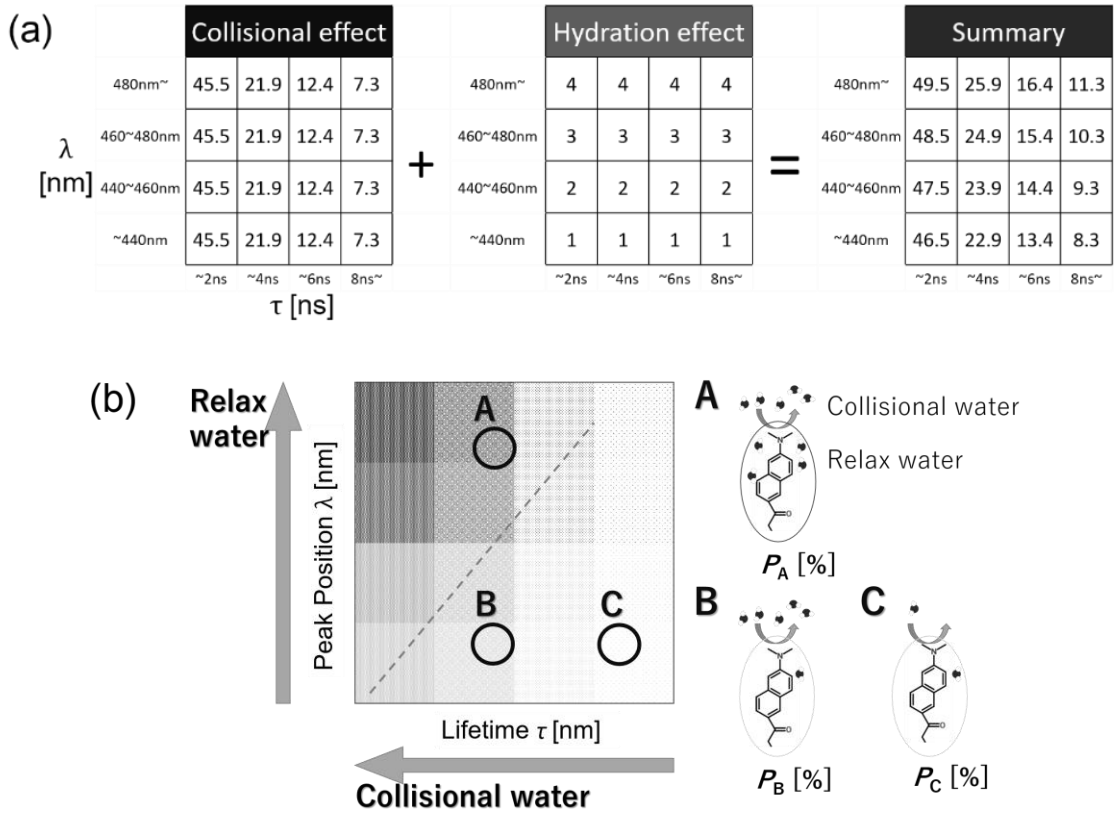

Figure 3-11(a) Model of the water map. The number written in each table is the number of water molecules per lipid. The numbers provided for "*Collisional effect*" were estimated from the results shown in **Figure 3-9 (b)**. The numbers for "*Hydration effect*" were assigned based on previous reports (Parasassi *et al*., 1997). **(b)** Concept for the water map. The number of water molecules per lipid is indicated with blue in the chart. A darker color represents a higher amount of water molecules. Hydrating water used for the relaxation of Laurdan would increase in proportion to the wavelength, and collisional water used for quenching decreases in proportion to the lifetime. The probability (P_A, P_B, and P_C) of each distribution can be calculated from the area ratio at the given points (A, B, and C).

3.4. Dynamic hydration behaviors during phase transitions and in phase separation

According to the water map, the number of water molecules per lipid was investigated for each lipid bilayer system. As shown in **Figure 3-12**, the number of water molecules per lipid at the DPPC bilayers was approximately 10 in the gel phase ($T < T_m$ = 41 ℃), and the value increased to approximately 25 at $T > T_m$.

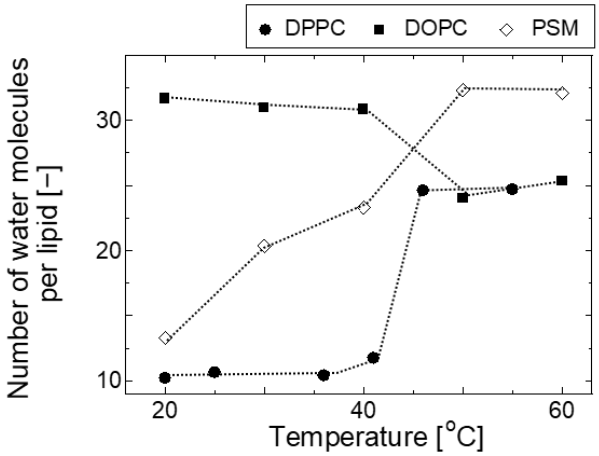

Figure 3-12 Average number of water molecules per DPPC (filled circles), DOPC (filled squares), and PSM (diamonds) molecule as a function of temperature. The calculations were performed as described in the text.

Table 3-2 Comparison of the number of water molecules per lipid molecule between in this study and in the reported results

	Temperature	Number of water		Ref.
		Reported	In this study	
DPPC	$T < T_m$ (= 41 ℃)	10.0	10	Alarcon *et al.*, 2016
	$T > T_m$	23.3	25	Gaede *et al.*, 2003
DOPC	30 ℃	32.5	32 (T < 50 ℃)	Chiu *et al.*, 2003 Nagle *e al.*, 1998
PSM	50 ℃	32.0	32 (T > 50 ℃)	Chiu *et al.*, 2003 Nagle *et al.*, 1998

Alarcón *et al.* estimated the average number of water molecules per DPPC using molecular dynamics simulations (Alarcón *et al.*, 2016). They showed that each molecule of DPPC was associated with approximately 10.0 water molecules in the gel phase and 23.3 in the liquid crystalline phase, which also confirms other report (Gaede *et al.*, 2003) (**Table 3-2**). Regarding the DOPC and PSM bilayers, our results also correspond to previous studies; 32.5 water molecules per DOPC molecule (at 30 ℃) obtained by X-ray diffraction (Chiu *et al.*, 2003; Tristram-Nagle *et al.*, 1998); 32 water molecules per 18:0 sphingomyelin (at 50 ℃ ($T > T_m$ = 41 ℃) calculated by molecular dynamics simulation (Chiu *et al.*, 2003; Tristram-Nagle *et al.*, 1998). In the DOPC bilayers, the number of water molecules per lipid gradually decreased due to the low quantum yield at high temperatures (**Figure 3-12**). The number of water molecules per PSM gradually increased

in proportion to temperature, which is similar to the tendency of *GP* values of Laurdan in the PSM bilayers in the steady state study in previous chapter. Therefore, our method, the deconvolution of TRES of Laurdan, strongly supports the insight into the number of hydration water molecules in the lipid bilayer system.

3.5. Hydration behaviors of DOPC/PSM binary systems

In DOPC/PSM binary mixture systems, the phase state can vary depending on the composition (Nyholm *et al*., 2011). **Figure 3-13** shows the TRES and the distributions of τ and λ values measured at 20 ℃. As the PSM content increased, both of shorter and longer lifetime components spectra became broader, indicating that the number of excitation states increased to more than two. With an increase in the PSM content, the patterns of τ and λ distributions altered from the fluid phase (in DOPC-rich, upper left region) to the gel phase (in PSM-rich, bottom right region). In the PSM and DPPC bilayers below T_m, the lifetime values of the major TRES component were 7.8–8.0 ns, suggesting the evidence of the gel phase with long lifetime. The lifetime values in the DOPC/PSM bilayers at PSM ≥ 80% were 7.8–8.1 ns, revealing their phase state as the gel phase. The presence of the component with $\lambda \leq 420$ nm also reveals the gel phase of PSM bilayers. λ values of less than 420 nm were observed in the DOPC/PSM bilayers at PSM ≥ 80%, suggesting the coexistence of gel and fluid phases at 50% ≤ PSM ≤ 80%.

In general, Laurdan coexist both in fluid and gel phases (Bagatolli *et al.*, 2000a, 2000b; M'Baye *et al*., 2008). Thus the area% of each TRES component reflects the population of the local environments. The thermotropic states of DOPC/PSM binary systems have been reported using differential scanning calorimetry (Nyholm *et al*., 2011). At 20℃, the phase boundaries appear at PSM = 33mol% (fluid and fluid-gel coexistence) and at PSM = 92 mol% (fluid-gel coexistence and gel). Expected phase states are as follows: fluid phase, 0% ≤ PSM ≤ 30%; fluid-gel coexistence, 40% ≤ PSM ≤ 90%; gel phase, 90% ≤ PSM ≤ 100%. The values of the number of water molecules per lipid are calculated for the DOPC/PSM bilayers, and the results are plotted as a function of PSM content (**Figure 3-14**). In the regions with less than 30% of PSM, the hydration levels were almost constant (31-32 water molecules per lipid), revealing that both DOPC and PSM molecules were in disordered conformation. Excessed number of water molecules

were significantly observed in the phase boundary compositions (PSM 30% and 90%) compared with the number expected from the PSM composition (solid line in **Figure 3-14**). In DOPC/brain sphingomyelin (bSM) systems, the DSC thermograms indicate that the phase transition temperatures of bSM can decrease in proportion to DOPC ratio, together with decreases of phase transition enthalpy (Petruzielo *et al*., 2013). This suggests that DOPC molecules disturb the packing of SM domain in binary mixtures. As a result, the SM molecules in disordered state can acquire the extra hydration waters. Despite the enthalpy energy loss due to the partial melting of PSM, the binary membrane could be stabilized by the entropy energy associated with water hydration. Yang *et al*. reported that line tension at the phase boundaries could be the driving force for HIV fusion peptide-mediated fusion (Yang *et al*., 2016). Given the accumulation of hydration water at the domain boundary, the boundary edge can be assumed as an active site for external molecules: their interaction would decrease the hydrating water molecules, which makes the hydration level of PSM bilayer ideal. This mechanism will reveal the spontaneous interaction with external molecules (Simons *et al*., 2010). In thermodynamic aspects, the entropic change in the process of the dehydration (release of counterions) is speculated as the driving force for binding with macromolecules (Lobo *et al*., 2001). Thus, it is necessary to evaluate the membrane-associating water molecules. The developed method could be useful for evaluating the thermodynamic property of membrane interfaces.

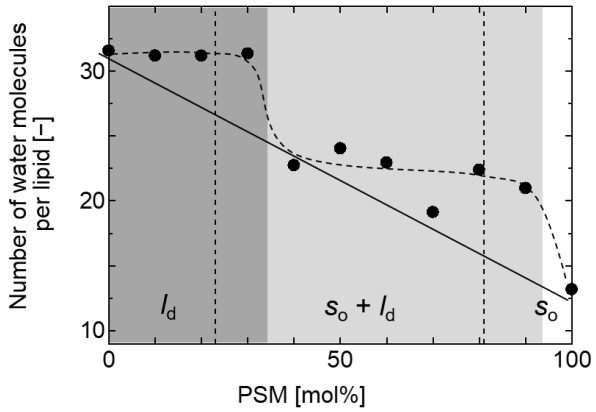

Figure 3-14 Number of water molecules per lipid in DOPC/PSM bilayers calculated with the same calculation in the case of DPPC. The phase states for the gel phase (s_o), the liquid-crystalline phase (l_d), and the two-phase coexistence regions (s_o + l_d) were colored with white, dark grey, and light grey, respectively. The dashed lines represent the phase boundaries as previously determined (Nyholm *et al*., 2011). The solid line represents the ideal transition to the PSM content.

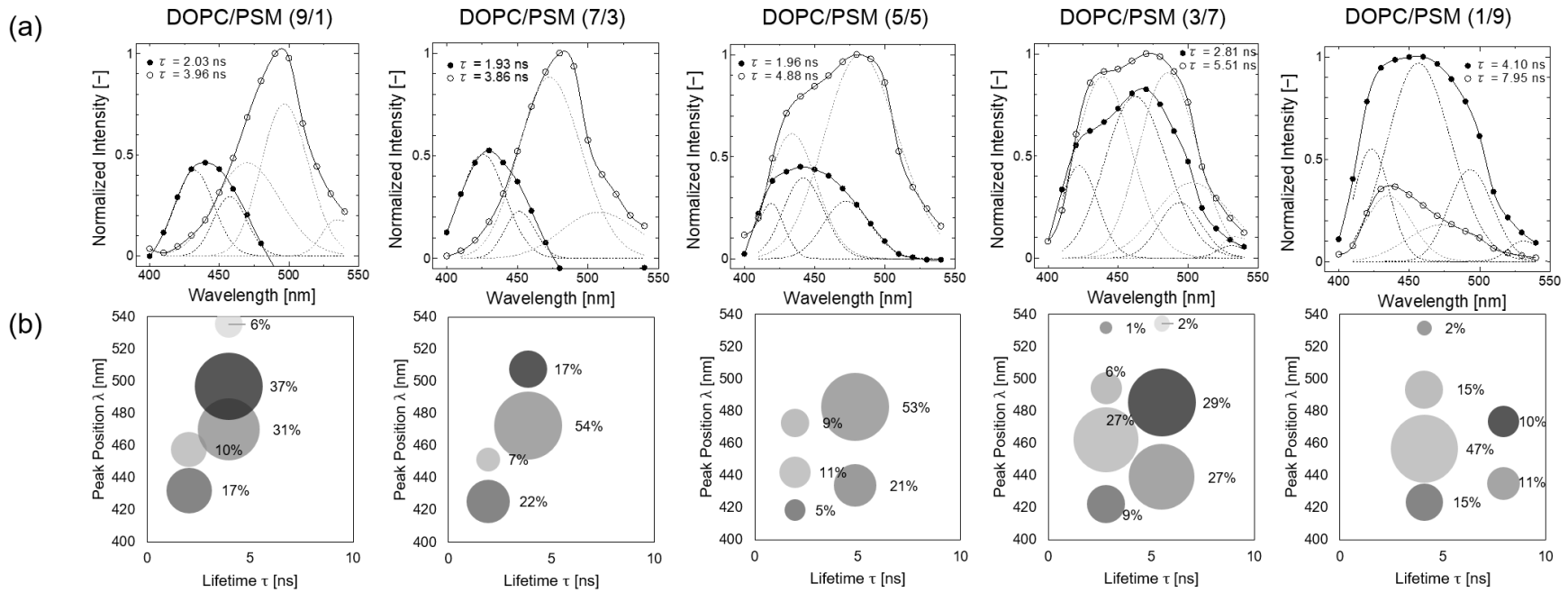

Figure 3-13 (a) TRES of Laurdan in DOPC/PSM bilayers. The lifetimes were represented in the figure. The solid and dotted lines represent the obtained TRES and deconvoluted peaks, respectively. Shorter and longer lifetime components were each depicted with filled and open circles, respectively. **(b)** The τ vs λ plot for the deconvoluted TRES of Laurdan in DOPC/PSM bilayers. The integrated area ratio of each component was reflected in the size of the bubbles.

4. Summary

TRES of Laurdan was analyzed as a function of the individual lifetime components. Depending on the relaxation states induced by the hydrated water molecules and molecular collisional quenching effects, the fluorescence components were extracted and analyzed using lifetime (τ) vs peak position (λ) plots. Based on the assumptions regarding the molecular collisional quenching of the water molecules, a model water map was established. The number of water molecules associated with lipid was estimated using the water map. In terms of bound water, the polar head group of the lipids may include a clustered state of the water molecules (Damodaran, 1998; Pasenkiewicz-Gierula *et al*., 2016; Tieleman *et al*., 1997). Laurdan is present in the hydrophobic/hydrophilic interfacial region near the carbonyl group of the phospholipid (Jurkiewicz *et al*., 2006). In addition, depending on the specific membrane properties, the vertical position of the Laurdan (i.e., how deep the molecules are intercalated) could change (M'Baye *et al*., 2008). However, the fact of different hydration conditions (static and dynamic) among various lipid species observed in this work is a key for understanding the membrane associating water molecules.

According to the investigations in Chapters 2 and 3, the information relating to the membrane hydration properties as the environment or as the molecular level was suggested. In Chapter 2, the different types of local solvent environments were classified mainly based on their dielectric constants, which was equilibrated as the spatial-property as a result of the long measurement time in the steady-state fluorescence method. In this chapter, kinetic difference of hydrating water molecules were revealed together with their concentration dependence (**Figure 3-15 (a)**). Based on both methodologies, the numbers of water molecules per lipid molecule depending on the solvent environments were calculated (**Figure 3-15 (b)**). As shown in the figure, the distributions of the number of water molecules in each solvent system were observed. Especially, the number of water molecules in the polar protic region increased as the temperature increase.

The gradient of the concentration of the water molecules is illustrated with the function of the dielectric constants (**Figure 3-16**). It is notable that the contribution of the collisional water molecules was dominant especially after the phase transition, suggesting the gradient of water concentration ([water]) would increase in $T > T_m$. The gap of the concentration of water molecules intrinsically indicates the capacitance of the membrane

for the active water molecules, as "*membrane-fluctuation*". Control of the active water may lead to the regulation of membrane-relating phenomenon such as molecular interactions, therefore, the design for the regulation of diffusive active water molecules will be proposed in the following chapters.

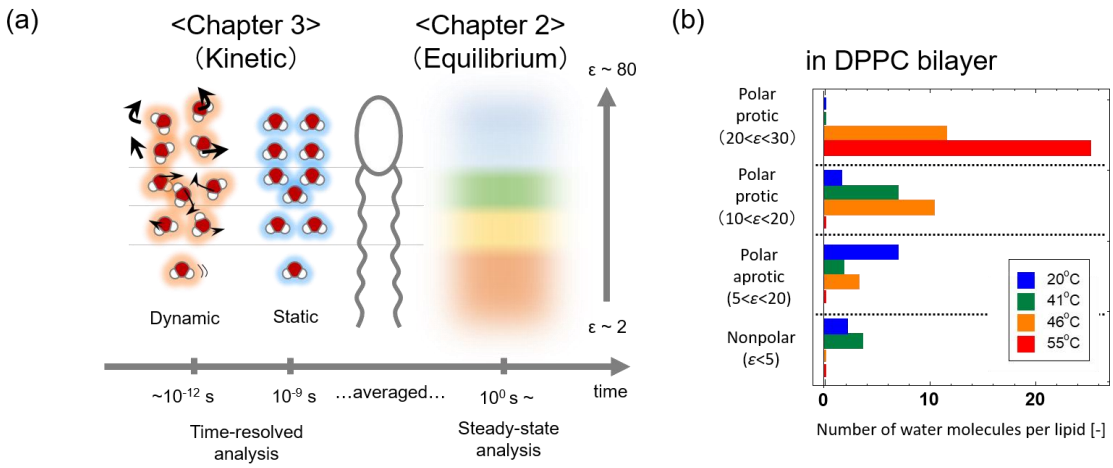

Figure 3-15 (a) Summary of the concepts of the observation results in Chapters 2 and 3.
(b) The number of water molecules per lipid

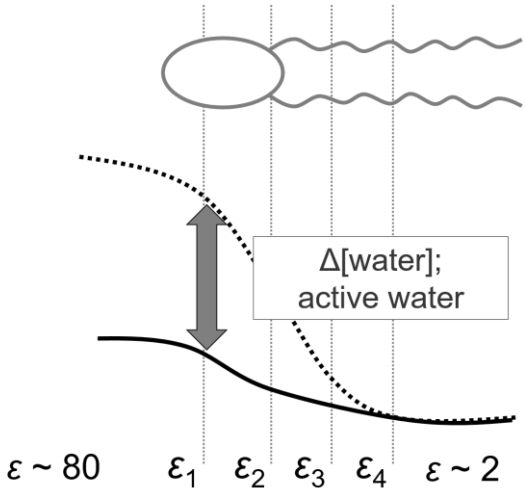

$$\frac{1}{U} = \frac{1}{f(\varepsilon_1)} + \frac{1}{f(\varepsilon_2)} + \frac{1}{f(\varepsilon_3)} + \frac{1}{f(\varepsilon_4)}$$

Figure 3-16 Schematic illustration of the membrane water gradient with the function of dielectric constants. Dielectric constants may describe the resistant of the system as environmental factor, for the regulation of active water.

Chapter 4

Design of Hydrophobic Membrane Interface based on the Guanidinium Modification

1. Introduction

Membrane modification is one of the strategies to acquire high affinity between the designed biomaterial and target molecule, which is already applied for biosensor or drug carrier. The cationic lipids have been attracted significant interest because of their promising efficiencies in gene delivery as nonviral carriers (Felgner *et al*., 1987; Gao *et al*., 1991; Leventis *et al*., 1990). The most common approach is to modify the cationic lipids or cationic surfactants into the lipid membrane, aiming for the strong electrostatic interactions between positively charged lipid membrane and negatively charged nucleic acids. The challenging issue is to control the assembled structure of lipid-based drug carrier. The strong ionization enhances the formation of multiple layers composed of counterions, in which the neutralized surface net charge of the membrane leads to the weak interaction with opposite charged molecules. In contrast, the enhanced charge state makes it difficult to target the lipoplex to the desired site, because the electrostatic interaction nonselectively works to the charged species. In addition, the strong electrostatic interaction leads the denaturation of associating molecules, resulting in unfavorable gene conformation (less or no activity after transfection). Therefore, the modification of the membrane surface should be important to improve the delivery systems of "*active*" molecules. Given the case of coupling of enzyme-substrate as a model of intermolecular interaction which works in a well-organized manner, the dissociation of the hydrophilic part on the molecular surface and the association of the hydrophobic parts should be performed sequentially. Applying this concept into the membrane systems, it is necessary to expel the water molecules that are existing at the hydrophilic region of the lipid membrane, to achieve further enhancement of the association of biomolecules. Herein, the effective interaction mechanism is considered referring to the behavior of the

guanidinium moieties as the representative of the active binding site.

The guanidinium moiety, which is seen in the side chain of arginine (Arg), shows a strong affinity toward negatively charged moieties, especially phosphate groups. The guanidinium-phosphate interaction is observed in nucleic acid−protein interactions (Pantos *et al*., 2008). Arg plays key roles in the formation of the supramolecular complexes; for example, the Arg binding site for free amino acids regulates the Tetrahymena self-splicing rRNA introns (Yarus, 1988). Additionally, the Arg moiety in human immunodeficiency virus-type 1 nucleocapsid protein binds to the major groove of the RNA stem, interfering with genome encapsidation (Guzman *et al*., 1998). These activities are derived from the cationic nature of guanidinium, and also from the "*chaotoropic property*" which enables to cut the surrounding hydrogen bonds due to its hydrophobic planar structure (Mason *et al*., 2004). However, the guanidinium interaction toward target moieties is weak in bulk water solution, in which surrounding water molecules disturb the formation of hydrogen bonding between guanidinium and phosphate (Onda *et al*., 1996). At the self-assembly interface, the guanidinium−phosphate interaction can be strengthened: for example a bilayer form in a bulk water and a monolayer form at the air−water interface, resulting in strong affinity (Onda *et al*., 1996). This suggests that the "*dehydrated* " platform is important for strengthening the molecular recognition of phosphate groups by guanidinium groups (Ariga *et al*., 2006; Ma *et al*., 2015; Onda *et al*., 1996). Given the model of cyclodextrin, which has ability to include molecules in its hydrophobic cavity, the well-designed interfacial environment and hydrophobic interaction are essential for enhancing intermolecular binding (Sakurai *et al*., 1989).

As described in above, the membrane interfaces are estimated as intermediate hydrophobicity with the value of $\varepsilon \sim 30$ (Chapter 2), in which the approximately 10 - 30 water molecules associate to a lipid molecule (Chapter 3). Because the bilayer membrane interfaces, can be considered neither as high polar solvent (like water) nor as nonpolar solvent (like hexane), which could provide a proper environment to perform the chaotoropic specificity of guanidinium. Hence, it is expected that the water molecules existing in the hydrophilic region of the lipid membrane can be expelled out by the modification of guanidinium at the membrane interface. This approach could provoke the

upper-shift of hydrophilic/hydrophobic membrane interface and could reduce the hydration layer that presents the molecular interaction, inducing the strong interaction with external molecules existing in the bulk region.

The aim of this chapter is to design the guanidinium derivative-modified vesicles with altered membrane properties. Two types of guanidinium derivatives were synthesized: stearyl guanidinium (SG), which has a saturated acyl chain with guanidinium, and myristoyl arginine (MA), which has the carbonyl group to neutralize the cationic guanidinium (**Figure 4-1**). Both guanidinium derivatives were incorporated into the bilayer membranes composed of 1-palmitoyl-2-oleoyl-*sn*-glycero-3-phosphocholine (POPC). The properties of modified membranes were characterized using Fourier transform-infrared (FT-IR) and Raman spectroscopy. Comparison to pure POPC vesicles revealed differences in the characteristics of the guanidinium-modified vesicles using fluorescent probe analyses. In addition, the interactions between vesicles and tRNA were studied to investigate the binding affinities. Based on the results, the effects of the guanidinium derivatives on the POPC membrane are discussed.

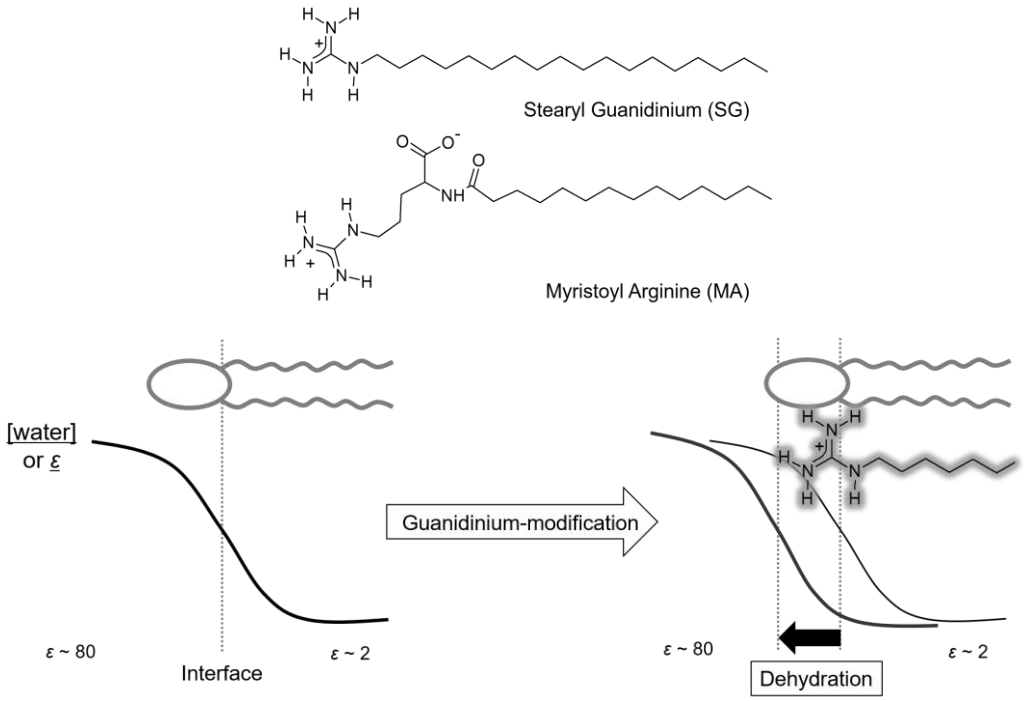

Figure 4-1 Structure of guanidinium derivatives, stearyl guanidinium (SG) and myristoyl arginine (MA), and schematic illustration of the guanidinium modification.

2. Materials and Methods

2.1. Materials

POPC was purchased from Avanti Polar Lipids, Inc. (Alabaster, AL, USA). Stearylamine and *p*-toluenesulfonic acid monohydrate were purchased from Tokyo Chemical Industry Co., Ltd. (Tokyo, Japan). Dimethyl sulfoxide was purchased from Kanto Chemical Co., Inc. (Tokyo, Japan). tRNA originating from *Escherichia coli*, S-methylisothiourea sulfate, and myristoyl chloride were purchased from Sigma Aldrich (St. Louis, MO). 1,6-Diphenyl-1,3,5-hexatriene (DPH) and 6-lauroyl-2-dimethylamino naphthalene (Laurdan) were also purchased from Sigma Aldrich. Other chemicals were purchased from FUJIFILM Wako Pure Chemical Corporation (Osaka, Japan). All chemicals were used as received.

2.2. Synthesis

SG was synthesized based on a previously described method (Onda *et al*., 1996). The reaction scheme is shown in **Figure 4-2**. The weight of SG was 1.95 g (33.9% yield). The synthesis of SG was ascertained by mass spectrometry and nuclear magnetic resonance (NMR) spectroscopy (**Figure 4-3**). MA was synthesized as described previously (Singare and Mhatre, 2012). The reaction scheme is shown in **Figure 4-4.** The weight of MA was 7.94 g (52.4% yield). Mass and NMR spectra are shown in **Figure 4-5**. After the synthesis, the white solid crystals of SG and MA were collected. Critical micelle concentration (CMC) values for SG and MA were 0.26 and 0.29 mM, respectively (see **Figure 4-6**).

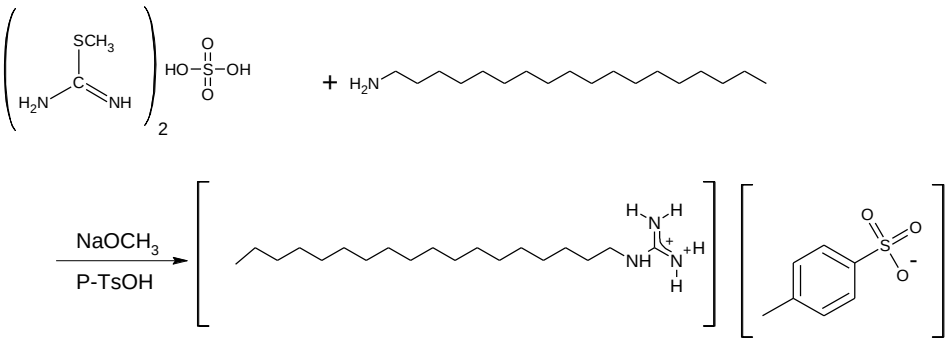

Figure 4-2 Synthesis of stearyl guanidinium (SG).

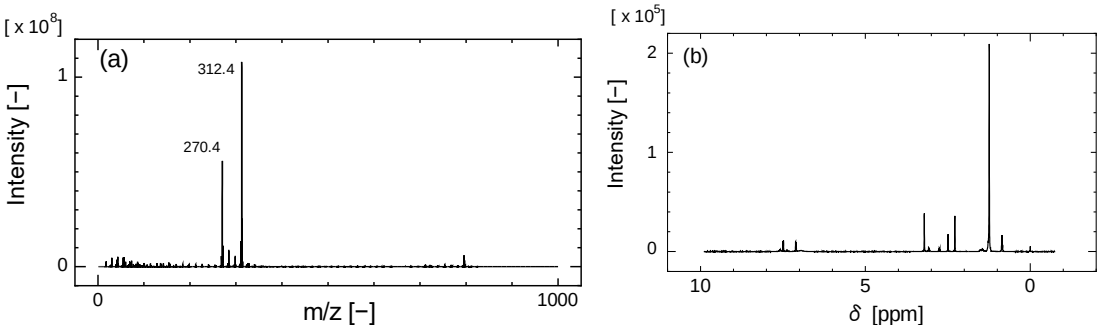

Figure 4-3 (a) Mass spectrum of synthesized stearyl guanidinium. Peak assignments of MS (Fab) are as follows: 270.4, $C_{18}H_{39}N_1$, (Mw, 269.5: stearylamine); 312.4, $C_{19}H_{42}N_3$ (Mw, 312.6, stearyl guanidinium). **(b)** ^{1}H NMR spectrum of stearyl guanidinium in DMSO-d6. Peak assignments are as follows: δ 0.89 (m, 3H, J = 0.2 Hz,CH_3), 1.24 (m, 30H, 15 CH_2), 1.51 (m, 2H, $NHCH_2CH_2$), 2.29 (s, 3H, $ArCH_3$), 3.12 (m, 2H, $NHCH_2$), 7.11 (d, 2H,J = 8.2 Hz, Ar), 7.49 (d, J = 8.2 Hz, Ar) and 7.38 (m, 5H, guanidinium). These peak assignments were well-confirmed to previous study (Onda *et al*., 1996).

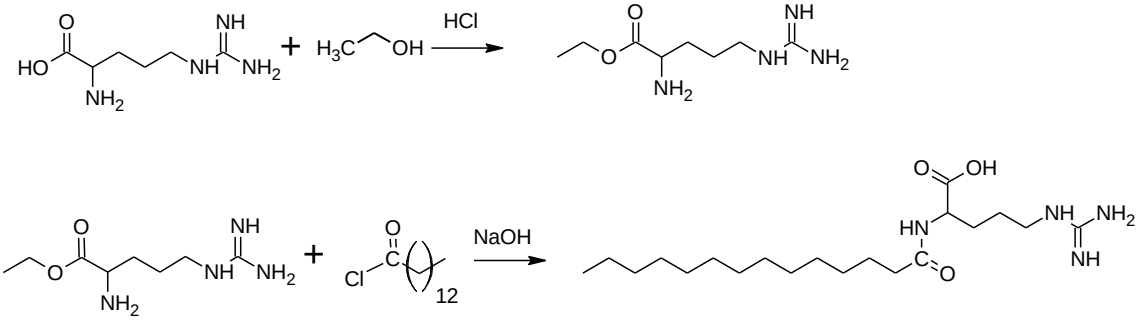

Figure 4-4 Synthesis of myristoyl arginine (MA).

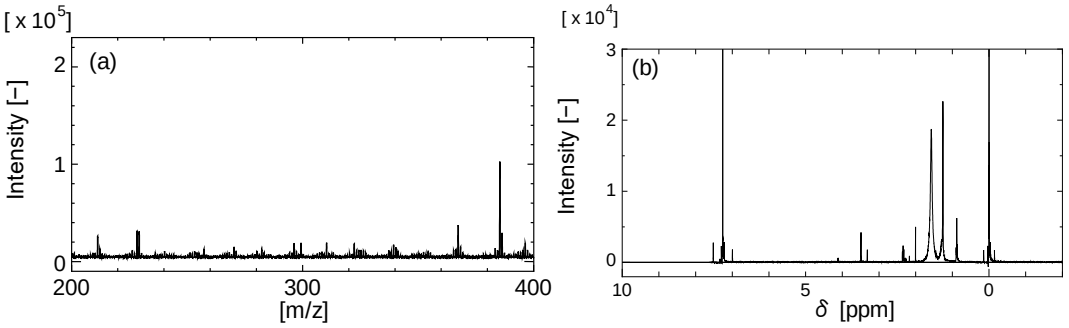

Figure 4-5 (a) Mass spectrum of synthesized myristoyl arginine. Peak assignments of MS (Fab) are as follows: 385.3, $C_{18}H_{39}N_1$, (Mw, 384.6: myristoyl arginine); 412.6, $C_{22}H_{44}N_4$ (Mw, 412.6, myristoyl arginine ester). **(b)** ^{1}H NMR spectrum of myristoyl arginine in d-Chloroform. Peak assignments are as follows: δ 0.881 (t, 3H, CH_3), 1.257 (t, 28H, CH_2), 1.576 (m, 2H, $NHCH_2CH_2$), 2.343 (t, 2H, CH_2CO), 3.492 (m, 2H, OCH_2CH_3), 4.132 (d, 1H,NHCHCOO), 6.997 (m, 3H, $C(=NH)NH_2$) and 7.519 (m, 1H, NHCHCOO). These peak assignments were well-confirmed to previous report (Singare *et al*., 2012).

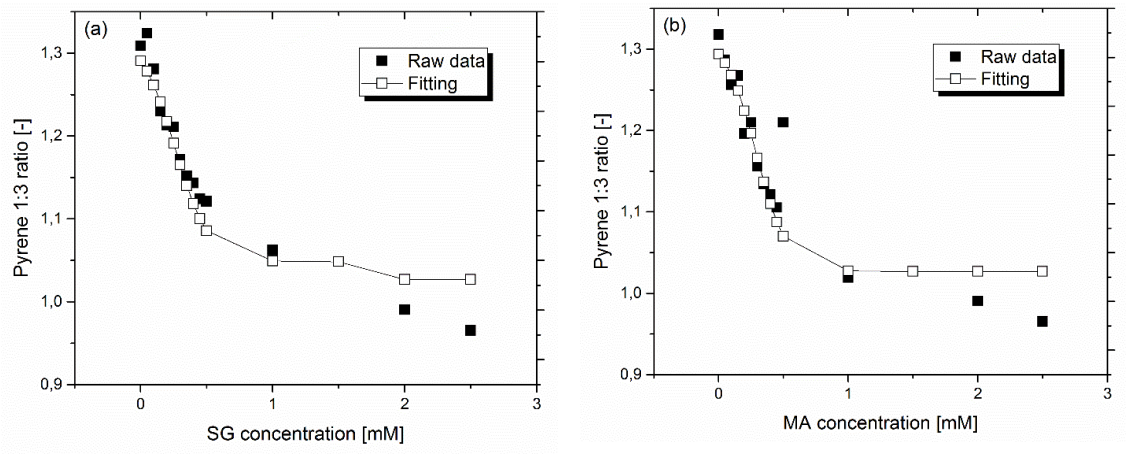

Figure 4-6 Plots of pyrene 1:3 ratio (■) and Boltzmann fitting (□) versus guanidinium concentration; SG **(a)** and MA **(b)**, respectively. Pyrene 1:3 ratio was measured according to the literature (Aguiar *et al*., 2003). Based on the sigmoidal fitting with Boltzmann equation, the critical micelle concentration (CMC) values for SG and MA were calculated as 0.26 and 0.29 mM, respectively.

2.3. Preparation of guanidinium-modified vesicles

POPC and SG or MA with different ratios were dissolved in chloroform in a round-bottom flask. The solvent was removed by rotary evaporation. The obtained thin layer was kept under a high vacuum for more than 3 h. After the addition of 1000 µL Tris-HCl buffer (100 mM, pH 8.0) to disperse the lipids, five cycles of freezing and thawing (−80 °C/50 °C) were carried out to obtain the aqueous suspension of guanidinium modified vesicles. Extrusion treatment, in which the vesicle suspension was passed through a polycarbonate filter membrane with a pore diameter of 100 nm, was repeated 11 times using a Liposofast extrusion device (Avestin Inc., Ottawa, ON, Canada). Milky-white suspensions were observed for both POPC/SG and POPC/MA vesicles, indicating the formation of bilayer vesicles, because this turbidity cannot be detected with a micelle suspension. After the extrusion, vesicle suspensions were kept in 4 °C until used.

2.4. Characterization of lipid interactions using FT-IR spectroscopy

A 20 µl sample was applied in a 50-µm-thick cell with a CaF_2 window. Infrared spectra were measured using a FT-IR 4100 spectrometer (JASCO, Tokyo, Japan)

equipped with an Hg-Cd-Te detector. The resolution was set at 2 cm^{-1} and frequency data ranging from 600 to 4000 cm^{-1} were collected for each sample. The infrared spectrum of water was subtracted from those of the samples. The accuracy of the frequency reading was better than ±0.1 cm^{-1}. One hundred scans excluding buffer and liposome background signals were accumulated. The spectra were smoothed with the Savitzky-Golay procedure. The total concentration of lipid was adjusted to 20 mM.

2.5. Lipid packing density estimation by Raman spectroscopy

Packing densities of guanidinium-modified vesicle were measured using a LabRAM HR-800 confocal Raman microscope (Horiba, Ltd., Kyoto, Japan). A 100 mW YAG laser operated with an excitation wavelength of 532 nm and an x 20 objective lens focused the laser beam. All the spectra were measured three times with a 30-s exposure time. After the background signals were subtracted, the baseline was corrected. Based on the reported methods (Batenjany *et al*., 1994; Fox *et al*., 2007; Levin *et al*., 1985), the packing density (*R*) of lipid membranes was evaluated as follows:

$$R = I_{2850} / I_{2930} \quad \text{(Eq. 4-1)}$$

where I_{2850} and I_{2930} represent the peak intensities at 2850 and 2930 cm^{-1}, respectively.

2.6. Characterization of membrane polarities using Laurdan

From the fluorescence analysis of Laurdan, the generalized polarization (GP_{340}) for vesicles was calculated. For a 1 mL volume of sample, the concentrations of lipid and Laurdan were 100 μM and 1 μM, respectively. After incubation for 30 min in the dark (30 ℃), the emission spectrum of Laurdan (Ex. 340 nm) was measured using a FP-6500 spectrofluorometer (JASCO). GP_{340} values were defined (Parasassi *et al*., 1990):

$$GP_{340} = (I_{440} - I_{490}) / (I_{440} + I_{490}) \quad \text{(Eq. 4-2)}$$

where I_{440} and I_{490} represent the intensity emission at around 440 and 490 nm, respectively.

2.7. Characterization of membrane fluidities using DPH

Membrane fluidity was evaluated from the fluorescence polarization *P* of the fluorescence probe, DPH, at the steady state. The dispersions including 100 μM lipids

and 0.4 μ M DPH were incubated for 30 min at 30 ℃ in the dark. The single emission intensity at 430 nm of DPH (excitation wavelength 360 nm) was measured using the aforementioned spectrofluorometer. Polarization (P) was defined as:

$$P = (I_{\parallel} - GI_{\perp}) \ / \ (I_{\parallel} + GI_{\perp}) \quad \text{(Eq. 4-3)}$$

$$G = i_{\perp} / i_{\parallel} \quad \text{(Eq. 4-4)}$$

where $I_{\perp}$ and $I_{\parallel}$ represent the emission intensities perpendicular and parallel, respectively, to the excitation light, $i_{\perp}$ and $i_{\parallel}$ are the emission intensities perpendicular and parallel, respectively, to the horizontally polarized light, and G is the correction factor. Membrane fluidity was evaluated based on the reciprocal of polarization, $1/P$.

2.8. Measurement of zeta potential

The zeta potential of each vesicle and the particle size was measured in the room temperature using a Zetasizer nano (Malvern Instruments Limited, Tokyo, Japan) as shown in **Table 4-1**. The total concentration of lipid was adjusted to 2 mM. The sample solutions were filtered to remove large aggregates (> 10 μm in diameter).

In the case of POPC/SG vesicles, large-size assemblies were observed, suggesting that POPC/SG vesicles could interact with each other. In the case of POPC/MA vesicles, the obtained PDI values were < 0.1, in most cases, suggesting that POPC/MA vesicles

Table 4-1 Size distribution of vesicles at pH 7.8

Vesicles	Size [nm][a]	PDI[a]
POPC	150.0	0.10
POPC/SG=9/1	121.8	0.09
POPC/SG=7/3	624.7	0.59
POPC/SG=5/5	110.3	0.35
POPC/SG=3/7	2021.0	1.00
POPC/MA=9/1	118.7	0.08
POPC/MA=7/3	133.4	0.10
POPC/MA=5/5	174.3	0.37
POPC/MA=3/7	140.8	0.10

[a] measured using an Zetasizer nano (Malvern Instruments Limited, Japan)

were dispersed in solution. Such differences could be derived by the insertion of SG or MA. It is notable that smaller assemblies (< 10 nm in diameter) were not observed in both cases of POPC/SG and POPC/MA vesicles, suggesting that quite less amount of micelles (self-assembly of SG and MA) exist.

2.9. Estimation of the binding constant: UV optical density assay

Turbidities of the vesicle suspensions were evaluated in the presence or absence of tRNA, using UV micro plate reader (Ultramark, Bio-Rad Laboratories, Inc., Hercules, CA). The optical density at 400 nm (A_{400}) was measured using a 96-well plate at 30 ℃. No absorbance at 400 nm was observed in the case of tRNA only (without vesicle). The total lipid concentration was 250 μM, with the varying concentrations of tRNA (0 to 10 μM). The binding constant (K_a) between lipid and nucleotide was calculated based on the reports (Marty *et al*., 2009; Stephanos *et al*., 1996). The K_a values were defined as follows:

$$\text{tRNA} + \text{vesicle} \rightleftharpoons \text{tRNA} - \text{vesicle complex}$$

$$K_a = \frac{[\text{tRNA}-\text{vesicle } complex]}{[\text{tRNA}][\text{vesicle}]}\ [M^{-1}] \qquad \text{(Eq. 4-5)}$$

The binding constant was calculated on the basis of the following (Marty *et al*., 2009):

$$\frac{1}{A-A_0} = \frac{1}{A_\infty - A_0} + \frac{1}{K_a}\frac{1}{(A_\infty - A_0)}\frac{1}{C_{\text{phosphate}}} \qquad \text{(Eq. 4-6)}$$

where A_0 is the turbidity of vesicles at 400 nm (in the absence of tRNA), A_∞ is the final turbidity of vesicles in the presence of tRNA (final tRNA concentration: 10 μM (750 μM phosphate)), A is the recorded turbidity at each phosphate concentration, and $C_{\text{phosphate}}$ is the concentration of total phosphate (in tRNA). The double reciprocal plot of $1/(A\text{-}A_0)$ versus $1/C_{\text{phosphate}}$ is linear, and K_a was estimated from the ratio of the intercept to the slope.

3. Results and Discussion

3.1. Intermolecular interactions of lipids evaluated by FT-IR spectroscopy.

The acyl chain packing behaviors and phosphate interactions can be confirmed using FT-IR spectroscopy (Seu *et al*., 2006). The peak at 2853 cm^{-1}, which is derived from the CH_2 symmetric stretch vibration (Mantsch *et al*., 1991), shifts toward a lower frequency by the increase in the membrane fluidity. In general, this peaks are observed at around 2850 cm^{-1} for gel phases and at around 2855 cm^{-1} for liquid-disordered phases. **Figure 4-6** shows the transition of peaks positions for the $\nu(CH_{2,sym})$ and for $\nu(PO_{2,asym})$ signals in the presence of POPC/SG and POPC/MA vesicles with different modification ratios. Vesicle suspensions may scatter light due to their Brownian motion, which weakens the FT-IR signals. Although the obtained signals in POPC/MA = 9/1 and POPC/MA = 7/3 were relatively weak, they showed sufficient peak intensities to identify each peak assignment. The $\nu(CH_{2,sym})$ peak in POPC/SG displayed a clear red shift from 2855 to 2850 cm^{-1}, while POPC/MA vesicles displayed no remarkable changes independent of MA ratios (**Figure 4-7 (a)**, **(b)** and **(e)**). These results indicate that POPC/SG vesicles adopted ordered phases, while conversely POPC/MA vesicles remained in a fluid state.

The peak at 1236 cm^{-1} derives from the PO_2 asymmetric vibration, and it has been reported to exert peak shift sensitively due to the hydrogen bonding with the surrounding environment. Seu *et al*. confirmed the red shift of the peak from 1235 to 1210 cm^{-1} due to the phosphate interaction in saturated monoacyl-phosphoethanolamine (PE) vesicles by addition of lyso-phosphatidylethanolamine (LPE) (Seu *et al*., 2006). Hence, the red shift in the phosphate asymmetric vibration indicates noncovalent interactions, such as electrostatic and hydrogen bond interactions, at the phosphate moieties. Regarding the $\nu(PO_{2,asym})$ signals, red shifts were observed in the presence of POPC/SG and POPC/MA vesicles (**Figures 4-7 (c)**, **(d)**, and **(f)**). Presumably, the interaction with the phosphate moiety derived from the guanidinium moieties. In particular, the marked peak shifts observed in POPC/MA vesicles with higher MA ratio indicates that a stronger interaction between phosphate and guanidinium moieties could be formed in POPC/MA vesicles, as compared to POPC/SG vesicles. This is because the head group of MA is composed of positively charged guanidinium and negatively charged carbonyl groups, which allows greater interactions through the electrostatic interactions with choline and phosphate

groups in POPC. In contrast, the SG molecule has a positively charged guanidinium, suggesting that an electrostatic interaction between POPC phosphate groups and SG guanidinium groups is the only attracting force at the head group region.

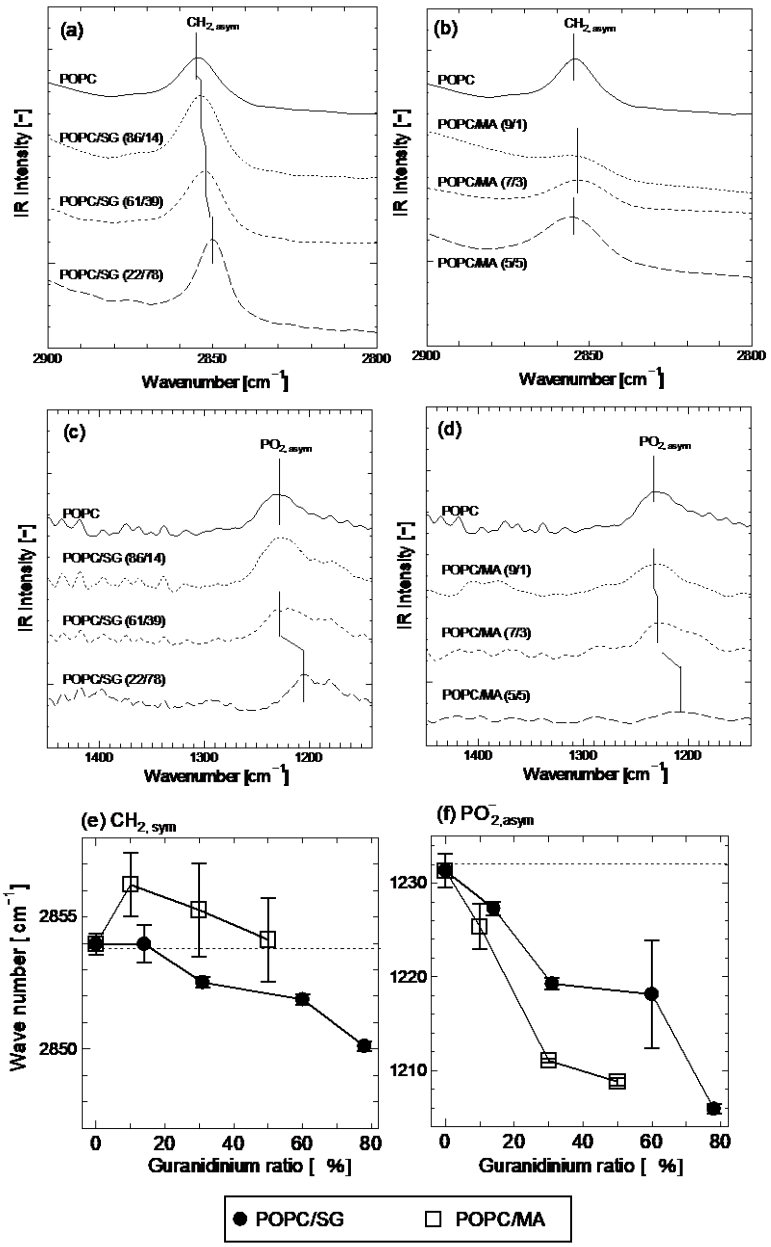

Figure 4-7 FT-IR spectra focusing on the stretching vibrational signals of $CH_{2,sym}$ **(a, b)** and $PO_2^-{}_{,asym}$ **(c, d)** in POPC/SG and POPC/MA vesicles. The peak wavenumbers of $CH_{2,sym}$ **(e)** and $PO_2^-{}_{,asym}$ **(f)** were plotted as a function of the guanidinium molar ratio: POPC/SG (●) and POPC/MA (□).

3.2. Lipid packing density estimated by Raman spectroscopy

The intermolecular interactions between lipid molecules reflect the packing states in the bilayer. Raman spectroscopy is commonly used to determine the packing density of acyl chains in lipid membranes (Suga *et al*., 2015). Based on Raman spectroscopic measurements, the signals derived from acyl chains were presently evaluated. These signals were the peak at 2850 cm^{-1} from methylene (CH_2) groups and the peak at 2930 cm^{-1} from methyl (CH_3) groups located at the terminus of the acyl chains. The lipid packing density R (= I_{2850}/I_{2930}) is defined from the ratio of mobility for each moiety and reveals membrane fluidity (Suga *et al*., 2015). The dependencies of packing densities in guanidinium vesicles on guanidinium ratios are shown in **Figure 4-8**. The R values were clearly increased by the modification with SG. In membranes in ordered (gel) phases, relatively weak signals at 2930 cm^{-1} were obtained due to the restricted CH_3 moiety, which resulted in higher R values. The molecular interactions between POPC and SG molecules could facilitate the dense packing of membranes. In contrast, the packing densities of POPC/MA vesicles were almost same as pure POPC vesicles. The results of FT-IR measurements (i.e., no significant red shifts in the $\nu(CH_{2,\,sym})$) indicated that the steric head group and short acyl chain of MA influence the inner components of the membrane and disturb membrane packing. The analyses of the intermolecular interactions revealed that POPC/SG vesicle membranes were densely packed with lower membrane fluidities. The addition of SG molecules quantitatively altered the membrane properties to produce more ordered. Conversely, POPC/MA vesicles are in a fluidic membrane state. In common with SG and MA, the guanidinium moieties likely undergo interactions with neighboring phosphate groups.

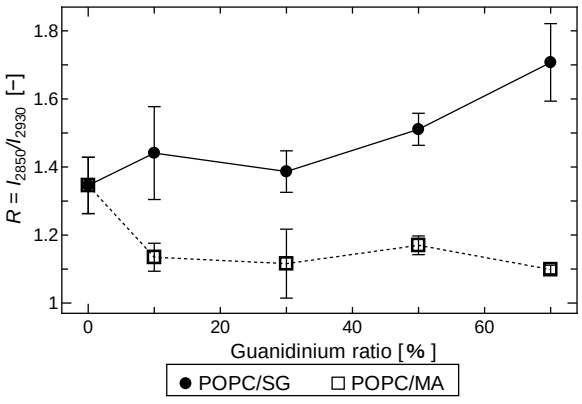

Figure 4-8 Packing densities R (=I_{2850}/I_{2930}) estimated from Raman spectra of POPC/SG (●) and POPC/MA (□) vesicles.

3.3. Membrane polarities and membrane fluidities of POPC/SG and POPC/MA vesicles

The hydration states can vary according to the phase states of the membranes (Hirsch-Lerner *et al*., 1999; Viard *et al*., 1997). The interior hydrophobic/hydrophilic environment of a membrane can be evaluated using Laurdan and Prodan fluorescent probes, which determine the membrane polarity of the inner and outer surface regions (Parasassi *et al*., 1998). Alterations in membrane properties can reveal the localization of external molecules to membrane surfaces, which can clarify the possible interactions between biomolecules and membranes.

The fluorescence emission of Laurdan is derived depending on the phase state. The peak appears at around 440 and 490 nm in the ordered and fluid phase, respectively (Parasassi *et al*., 1998). Here, the *GP* analysis using Laurdan was employed to simply-evaluate differences in the membrane polarities, which could be altered depending on the type and amount of guanidinium molecules (SG and MA). **Figure 4-9** shows the GP_{340} values for POPC/SG and POPC/MA vesicles. GP_{340} values for POPC/SG vesicles increased in proportion to the guanidinium ratio, indicating that the membrane became hydrophobic. POPC/MA vesicles exhibited hydrophilic properties (lower GP_{340} values, as well as POPC vesicles). These differences may have originated from lipid structures. SG molecules, with their longer acyl chain (C18) and smaller head group, tightly interact with POPC molecules, resulting in the elimination of water molecules from the membrane. For POPC/MA vesicles, while, hydrophilic membrane properties are maintained independent of the MA modification ratio. The bulky head group and shorter acyl chain (C14) of MA might not allow tight association with POPC molecules, although guanidinium-phosphate interaction is possible.

The fluorescent probe DPH measures membrane fluidity (Ahmed *et al*., 1997; Lentz *et al*., 1976). The relationship between the guanidinium modification ratios and $1/P$ values is shown in **Figure 4-10**. The membrane fluidities of POPC/SG decreased with higher ratios of guanidinium modification, whereas no marked changes in $1/P$ values were observed in POPC/MA. Membrane fluidity values of POPC/SG vesicles were altered in a dose-dependent manner by the modification with SG. Although it might be difficult to evaluate the true amount of guanidinium in the membrane, the observed results could

indicate the insertion of guanidinium into the vesicles. Considering the location of the DPH probe, SG molecules could lead to a dense packing of the inner region of the membrane, due to the smaller head group and longer acyl chain. In contrast, MA molecules, which possess a larger head group and shorter acyl chain, disturb the membrane packing, resulting in higher membrane fluidities, as well as in POPC vesicles.

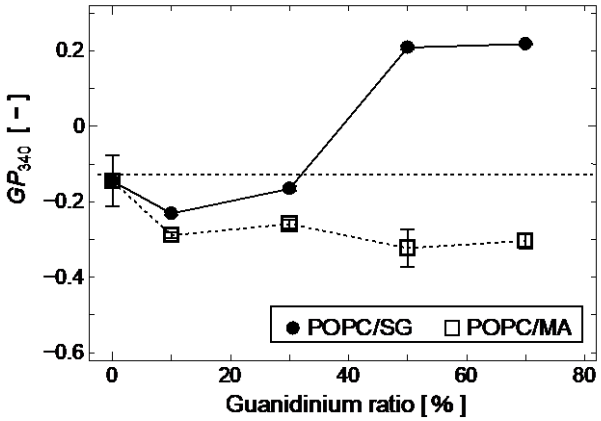

Figure 4-9 GP_{340} values of POPC/SG (●) and POPC/MA (□) vesicles, plotted as a function of molar ratio of guanidinium in vesicles. Total concentration of lipid and Laurdan were 100 and 1 μM, respectively. All measurements were conducted at 30 ℃.

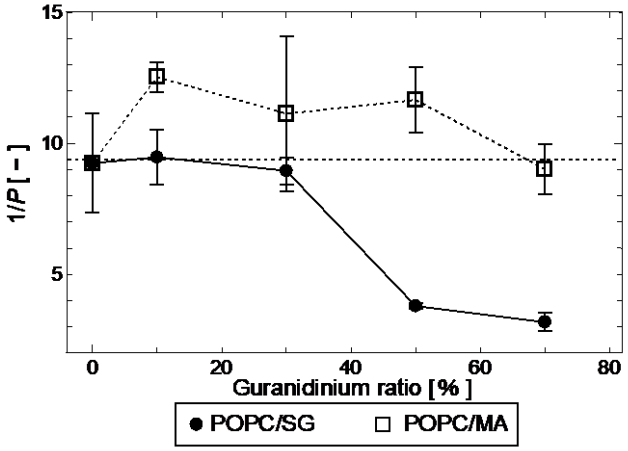

Figure 4-10 1/*P* values of POPC/SG (●) and POPC/MA (□) vesicles, plotted as a function of molar ratio of guanidinium in vesicles. Total concentration of lipid and DPH were 100 and 0.4 μM, respectively. All measurements were conducted at 30 ℃.

The phase states of POPC/SG and POPC/MA vesicles have been examined using the previously reported method (Suga *et al*., 2013). DPH and Laurdan analyses have determined that the phase state of lipid membranes can be classified into solid-ordered (gel, s_o), liquid-ordered (l_o), and liquid-disordered (fluid, l_d) phases (De Almeida *et al*., 2003; De Lange *et al*., 2007; Veatch *et al*., 2005). The 1/*P* values (x-axis) and GP_{340} values (y-axis) are plotted on a two-dimensional Cartesian diagram. The diagram empirically represents the l_d (*fluid*) phase at the fourth quadrant, heterogenic phases at the first to second quadrants, and ordered (s_o, l_o) phases at the second quadrant. Cartesian diagrams for POPC/SG and POPC/MA vesicles are shown in **Figure 4-11**, and the phase states estimated are summarized in **Table 4-2**.

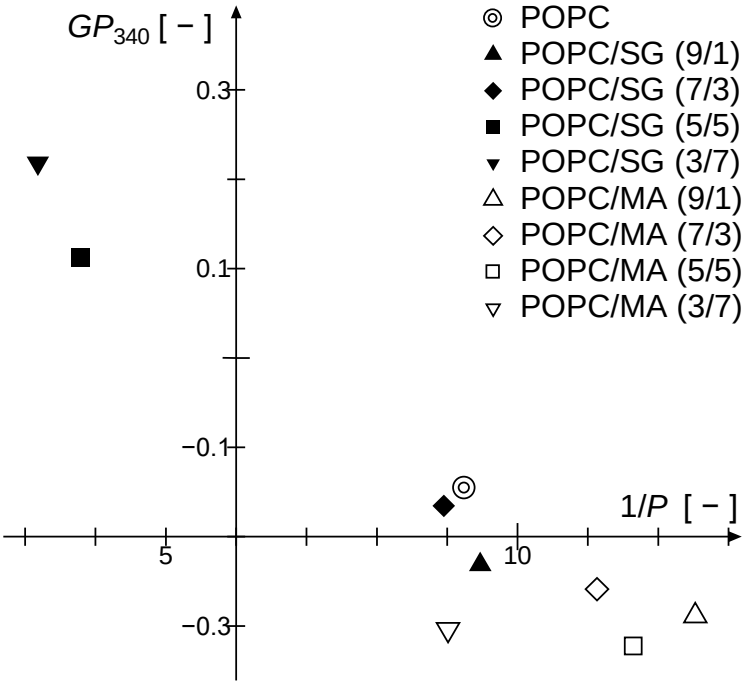

Figure 4-11 Cartesian diagram (Suga *et al*., 2013) for POPC/SG and POPC/MA vesicles at 30 °C. 1/*P* and GP_{340} values indicate the membrane fluidity and polarity. The decrease of GP_{340} values means membrane become more hydrophobic, and the increase of 1/*P* indicates the increase of membrane fluidity. Vesicles plotted in the second quadrant ($1/P < 6$, $GP_{340} > -0.2$) and in the fourth quadrant ($1/P > 6$, $GP_{340} < -0.2$) were considered in disordered phases and in ordered phases, respectively. Symbols indicate POPC (double circle), filled marks for POPC/SG, open marks for POPC/MA, and each guanidinium ratios were illustrated triangle for (9/1), diamond for (7/3), square for (5/5), and inverse triangle for (3/7), respectively.

Table 4-2 Phase state of each vesicle estimated from Cartesian diagram at 30 ℃

Vesicles	**Phase state**[a]
POPC	l_d
POPC/SG=9/1, 7/3	l_d
POPC/SG=5/5, 3/7	l_d + l_o-like[b]
POPC/MA=9/1, 7/3, 5/5, 3/7	l_d

[a] Determined by 1/*P* and GP_{340} values. For details, see the literature. (Suga *et al*., 2013). Data are shown in Figures 4-9 and 4-10.

[b] The ordered phase provided by SG modification was defined as l_o-like phase.

POPC membranes behave as fluidic liquid-disordered phases above −4 ℃, because of the presence of unsaturated acyl chains. As shown in **Table 4-2**, most of the guanidinium-modified vesicles were estimated as fluidic phase states (l_d phase). Saturated lipid molecules, such as DPPC and sphingomyelin, tend to form ordered domains. Thus, it is assumed that SG molecules cluster and then form SG-enriched ordered domains. Generally, "l_o phase" describes lipid domains constructed with cholesterol (Paleos *et al*., 1999). The ordered phase states provided by SG molecules have been described as l_o-like, because their physicochemical membrane properties (1/*P* and GP_{340}) are similar to the vesicles in l_o phases (e.g., POPC/Cholesterol). Thus, POPC/SG = 5/5 and POPC/SG = 3/7 vesicles were categorized as heterogeneous phases (l_d + l_o-like). POPC/SG vesicles may have a local hydrophobic and ordered region, compared with POPC/MA vesicles. Such heterogeneous domain structures could contribute the enhanced interaction with biomolecules (Suga *et al*., 2013). In particular, the l_o domains of POPC/cholesterol vesicles could interact with RNA and affect the translation process in cell-free protein expression systems (Suga *et al*., 2011). From these points of view, local hydrophobic and ordered regions could interact with RNA molecules.

3.4. Calculation of binding constants between the phosphate group in tRNA and lipid in vesicles

The turbidity of vesicle suspension is sensitive to the aggregation of vesicles via a target molecule (Suga *et al*., 2011; Thomas *et al*., 2005). The turbidity of POPC/SG vesicle suspensions in the presence of tRNA increased as the concentration of total phosphate increase (**Figure 4-12**). Based on the double reciprocal plot method reported previously (Marty *et al*., 2009; Stephanos *et al*., 1996), the binding constants K_a for phosphate (tRNA) and lipid were calculated (**Figure 4-13**, **Table 4-3**). The turbidity increase was not observed for POPC and POPC/MA in the presence of 100 μM of tRNA (total 7.5 mM phosphate), suggesting the K_a value of POPC and POPC/MA was $< 1.3 \times 10^3$ M^{-1}. This is consistent with a previous report (Suga *et al*., 2011). Considering the difference in K_a values for POPC/SG vesicles, the binding behavior may depend on the membrane properties, characterized by the analyses of membrane fluidity ($1/P$) and membrane polarity (GP_{340}). It has been reported that the lipid ordered domains preferentially bind to the nucleic acid (Janas *et al*., 2010; Suga *et al*., 2011), suggesting that membrane heterogeneity is key for the high affinity with biomolecules. POPC/SG = (86/14) showed the highest binding constant among POPC/SG vesicles, suggesting that the SG molecule in the l_d phase is more effective for recognizing phosphate in tRNA than that in the l_o phase. Immobilized ions were reported to alter the strength of hydrophobic interactions between molecules, suggesting a strategy to optimize molecular recognition and self-assembly processes by tuning hydrophobicity (Ma *et al*., 2015). In addition to the affinity of guanidinium moiety for the phosphate group, the membrane properties are thought to play key roles in the association of tRNA by POPC/SG vesicles. As shown in **Figure 4-13**, POPC/SG vesicles revealed larger K_a values compared with that of L-arginine (Janas *et al*., 2010) and guanidinium bilayers (Onda *et al*., 1996), indicating the hybrid lipid membrane interface is working cooperatively to the interaction.

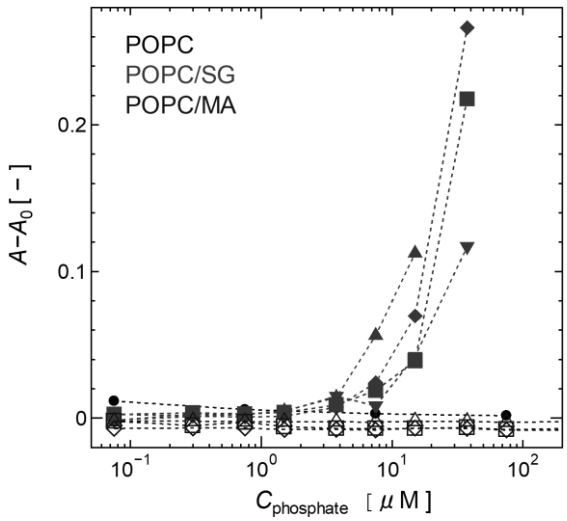

Figure 4-12 Optical density (A_{400}) analysis for POPC/SG and POPC/MA vesicles in the presence of tRNA. Symbols indicate closed circle for POPC, filled marks for POPC/SG, and open marks for POPC/MA. Each guanidinium ratio were illustrated triangle for (9/1), diamond for (7/3), square for (5/5), and inverse triangle for (3/7), respectively. Total lipid concentration was 250 μM, and all experiments were performed at 30 ℃. A_0 indicates the A value in the absence of tRNA. Increase of (A-A_0) value indicates the formation of complex between tRNAs and vesicles.

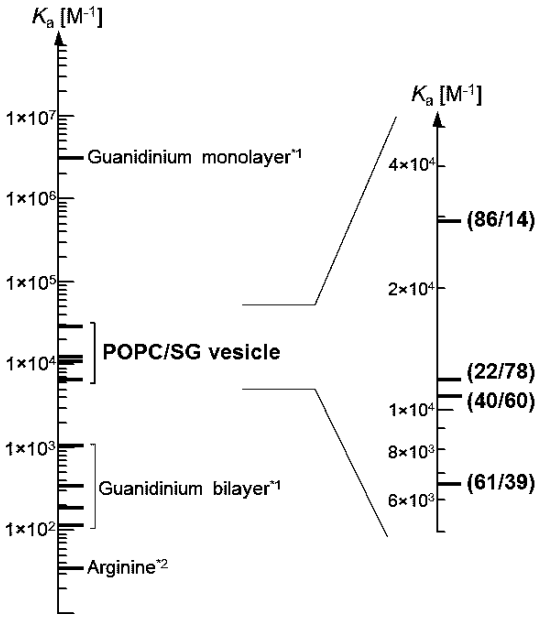

Figure 4-13 Summary of K_a values for phosphate-ligand interaction. The K_a values for POPC/SG vesicles at 30 ℃ were calculated based on Eq. 4-5 and Eq. 4-6 (see Experimental section). The K_a values for guanidinium bilayer and monolayer (^{*1}), and for arginine (^{*2}) were taken from previous reports (Onda *et al*., 1996) and (Janas *et al*., 2010), respectively.

Table 4-3 Summary of K_a values and number of phosphate bound to vesicle

Vesicle	K_a [M^{-1}]	Concentration of phosphate bound to vesicle [%][a]	Number of tRNA on vesicle [-][b]
POPC, POPC/MA	~1.0×10^3	< 4.3 ± 0.9	—
POPC/SG=(86/14)	2.9±0.4 × 10^4	97.2 ± 0.5	20.1 ± 4.1
POPC/SG=(61/39)	6.5±0.6 × 10^3	90.3 ± 0.7	83.0 ± 7.1
POPC/SG=(40/60)	1.1±0.7 × 10^4	93.7 ± 0.3	50.1 ± 3.1
POPC/SG=(22/78)	1.2±2.1 × 10^4	93.6 ± 1.3	51.2 ± 12

[a] Calculated at the following condition: $C_{phosphate}$, 150μM; C_{lipid}, 250μM: at 30 ℃.

[b] Calculated at the following condition: $C_{phosphate}$, 150μM; C_{lipid}, 250μM: at 30 ℃. tRNA was considered as 75 mer of nucleotide. The number of lipid molecules per vesicle was calculated as shown in the literature (Suga *et al*., 2013).

The number of phosphates (in tRNA) binding sites to the membranes and the concentration of complex were calculated (**Table 4-3**). Under this condition, the number of phosphates binding to POPC/SG = (86/14) was the highest, while that to POPC/SG = (61/39) was the lowest. Charge neutralization is one of the dominant driving forces of colloidal aggregation. In POPC/SG = (86/14) (l_d phase), SG molecules may be scattered in the membrane, and the tRNA-bound surface quickly may tune to the negative charge, resulting in a rapid interaction between the tRNA-free surface (positive charge). In contrast to the case for SG-enriched vesicles (including l_o-like phase), SG may be clustered in the membrane surface, where most of the tRNA surface can be neutralized. This would lead decreased binding affinity between the tRNA-bound surface and tRNA-free surface. This indicates that the phase state of the POPC/SG vesicles are crucial for controlling the binding between phosphate and lipid. It was found that only a small number of phosphate groups of tRNA were bound to POPC and POPC/MA (ca. 4.3 %), which may be negligible to the number of SG molecules bound to the phosphate in tRNA.

4. Summary

Two kinds of guanidinium-modified vesicles were prepared to modulate the interactions with nucleic acid molecules (i.e., tRNA), and to induce its conformational changes on the membranes. The investigations based on FT-IR, Raman, fluorescence probes, and UV optical assay revealed that SG-modified vesicles (POPC/SG) have hydrophobic and ordered membrane phase states, and strong affinities. It is anticipated that cationic POPC/SG vesicles induce the robust interactions with tRNA because of their inner membrane hydrophobicity derived from highly-packed membrane property. Comparatively, MA-modified vesicles (POPC/MA) have hydrophilic and disordered phase states, and it showed low affinity to tRNA. These findings reveal the potent use of guanidinium modified vesicles to enhance interactions with RNA molecules, and the importance of self-assembly systems, which could control these interactions by the regulation of membrane hydration properties as a "*platform*".

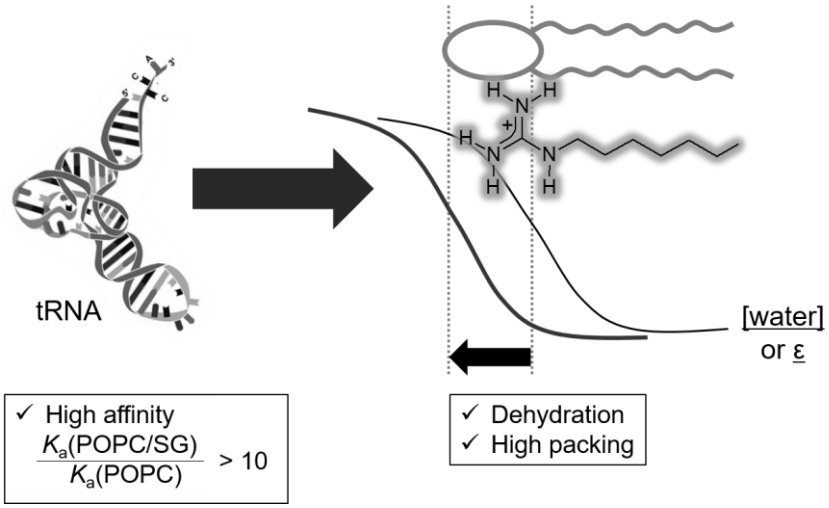

Figure 4-14 Concept of the performance of the guanidinium-modification.

Chapter 5

Mechanism of the Interaction

at the Lipid Membrane Interface

1. Introduction

The water molecules randomly distribute in a finite three-dimensional space by dynamically swapping their dipole–dipole interactions, and form a hydrogen bond network among water molecules via electrostatic interactions. Ultimately, a layer of water molecules is formed from a hydrophobic interface with a thickness that spans several nanometers (Fumagalli *et al*., 2018; Umeyama *et al*., 1977). Although the definition of the hydration layer varies depending on the interface to be targeted, a similar tendency can be observed within biological interfaces.

Israelachvili *et al*. measured the intermolecular forces between mica plates in dilute KCl solutions (Israelachvili *et al*., 1978). The interaction of the two interfaces was well explained by the DLVO theory using its distances of 10 nm or less. When the distance of the interfaces was less than 1.5 nm, the oscillations appeared at every 0.25 ± 0.03 nm (Israelachvili *et al*., 1983). In this case, 6–7 oriented water molecules existed between the mica plates. The short-range hydration force between the smooth rigid surfaces was always oscillatory as water molecules attached to the hydrated surface groups and formed an ordered layer (Israelachvili *et al*., 1983). This repulsive force is a synergistic hydrogen bond (polarized) interaction that attenuates as a function of distance from the surface (Gruen *et al*., 1983; Marcelja *et al*., 1976). Interestingly, in flexible surfaces, such as lipid membranes, these vibrations are averaged into a monotonous repulsive force owing to the entropic constriction of the head group (Kurniawan *et al*., 2015; Kurniawan *et al*., 2014; Shrestha *et al*., 2016). The question arises about how these dissipative properties affect the adsorption behavior on lipid membranes with molecules as the system.

There are two distinct forces, "*strong interactions*" and "*weak interactions*". For example, the interactions between cationic lipid membranes and nucleic acids can be

classified as "*strong interactions*", wherein the interactions take place with high affinity ($K_a > 10^4$ M^{-1}). According to the isothermal titration calorimetric (ITC) analysis, the binding of the plasmid DNA to the liposome composed of cationic lipids was observed with high affinity, whereas the liposomes containing zwitterionic lipids displayed a negative enthalpy upon binding to plasmid DNA (Lobo *et al*., 2001). Therefore, the association of the two oppositely charged molecules (e.g., cationic lipid and nucleic acid) is favorable for entropic reasons wherein the originally associated counterions released into the bulk solution (**Figure 5-1**).

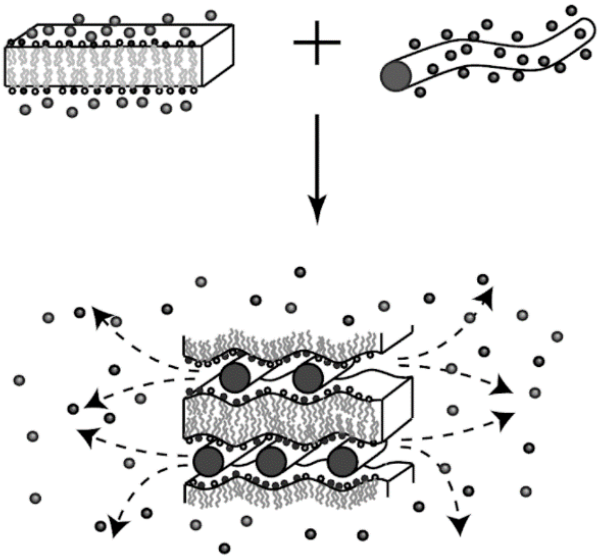

Figure 5-1 Schematic illustration of the condensation of DNA and lipid bilayers. In the process, the previously confined counter ions are expelled out (Templeton, 2008).

Strong charge state of the membrane surface layer is not always required for adsorption to the membrane, which is the case of "*weak interactions*". Selective adsorption of L-tryptophan was observed on liposome membranes. After the long incubation, the chiral recognition could take place in several steps by the rearrangement of surface assembly, such as electrostatic interaction, dehydration, and hydrogen bonding with plural phospholipids. In other case, Janas *et al* proposed the possibility that RNA-membrane association might be varied by selection of suitable RNA structures. Intermediate order membrane state such as liquid-ordered of rafted state shows RNA-structure dependent affinity ($K_a < 10^2$ M^{-1}), even though the ripple or gel phases show higher affinity of binding but no significant RNA-structure specificity (Janas *et al*., 2006).

From these observations, it is considered that the molecular adsorption at lipid membrane can be classified depending on the forces during the interaction, and each interaction experiences the different adsorption process. In particular, the strong interaction provoke rearrangement of the whole system, on the other hand, the weak interaction cooperatively demonstrates the molecular interactions at the lipid membrane surface without significant dehydration (**Figure 5-2**).

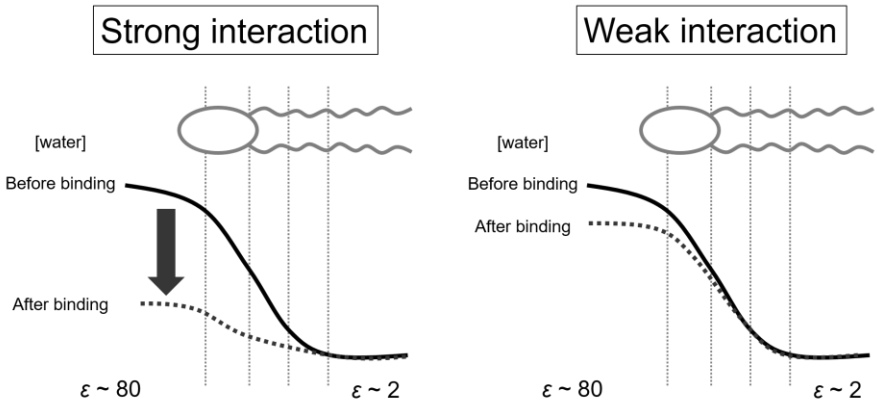

Figure 5-2 Conceptual illustration of dehydration behavior in the "*strong interaction*" and "*weak interaction*".

In this chapter, the dehydration behaviors observed during the interactions between POPC/SG and tRNA were compared with the interactions between DOPC and oligonucleotide. According to the investigation on the population of hydration water molecules, the correlation was observed between the number of water molecules and the conventional *GP* values measured from Laurdan fluorescence properties. ITC measurements were performed with regard to the adsorption of the oligonucleotide composed of single type of nucleotides in order to investigate the selective adsorption of nucleobases on the membrane surface. The fundamental comprehension of the adsorption behavior at the lipid membrane was aimed from the aspects of the thermodynamic behavior in the interaction process and the molecular selectivity that could contribute to revealing the possibility of the molecular recognition on the lipid membrane.

2. Materials and Methods

2.1. Materials

Phospholipids, such as 1,2-dioleoyl-*sn*-glycero-3-phophocoline (DOPC), and 1-palmytoyl-2-oleoyl-phosphocoline (POPC), were purchased from Avanti Polar Lipids, Inc. (Alabaster, AL, USA). Stearyl guanidinium were synthesized as explained in Chapter 4 (see Section 4.2.2.). tRNA originating from *Escherichia coli*, 6-lauroyl-2-dimethylaminonaphthalene (Laurdan), and cholesterol (Ch) were purchased from Sigma Aldrich (St. Louis, MO). Oligonucleotides (poly dX; X = adenine (A), cytosine (C), guanine (G), and thymine (T), each of 25 nucleotides) were purchased from Thermo Fisher Scientific, Inc. (Massachusetts, USA). Other chemicals were purchased from FUJIFILM Wako Pure Chemical Corporation (Osaka, Japan). All chemicals were used as received.

2.2 Preparation of guanidinium-modified vesicles

POPC and SG, DOPC, or DOPC and Ch were dissolved in chloroform in a round-bottom flask, respectively. The solvent was removed by rotary evaporation. The obtained thin layer was kept under a high vacuum for more than 3 h. After the addition of 1000 μL Tris-HCl buffer (100 mM, pH 8.0) to disperse the lipids, five cycles of freezing and thawing (−80 ℃/50 ℃) were carried out to obtain the aqueous suspension of guanidinium modified vesicles. Purified water was used for the hydration of DOPC and DOPC/Ch vesicles. Extrusion treatment, in which the vesicle suspension was passed through a polycarbonate filter membrane with a pore diameter of 100 nm, was repeated 11 times using a Liposofast extrusion device (Avestin Inc., Ottawa, ON, Canada). After extrusion, vesicle suspensions were kept in 4 ℃ until used.

2.3. Emission spectra of Laurdan in the presence of nucleic acids

The fluorescence spectra of Laurdan were measured by using a fluorescence spectrophotometer (FP-8500; Jasco, Tokyo, Japan). The excitation wavelength of Laurdan was 340 nm, measured with a 5 nm path length quartz cell. The fluorescence intensity of Laurdan was normalized with the maximum intensity as 1. The Laurdan was

added to the liposome suspension with a molar ratio of lipid/Laurdan of 100/1. After the measurement of the spectra with pure liposome system, the nucleic acids were added. The concentration of the nucleic acids were selected as the estimated concentration wherein the interaction occurs; the ratio of the lipid/nucleic acids are 250/2 for POPC/SG and tRNA and 1/1 for DOPC and oligonucleotides, respectively. After the addition of the nucleic acids, the samples were incubated at 30 ℃ more than 30 minutes before the measurements.

2.4. Adsorption of oligonucleotides on lipid vesicles; Isothermal titration calorimetry

ITC experiments were performed using a MicroCal™ iTC_{200} System (Malvern, UK). All experiments were done at 25 ℃ in pure water system. The vesicle solution was prepared in the cell (200 µl, 20 µM) and the solution of oligonucleotides (poly dX; X = A, C, G, and T) were prepared in the titration syringe (60 µl, 100 µM). After the thermal equilibration of the instrument, titration was performed. The first injection was 0.4 µl, and that for all others was 2 µl, with 100 seconds interval between injections, as total 20 injections. The dilution heat was calculated from the injection of pure water into vesicle solution, and was subtracted from the titration results of DNA solution.

The main assumption of the model used here is that oligonucleotide binding to cationic lipid is governed by thermodynamic equilibrium of the following process,

$$\text{poly dX} + \text{Lipid} \rightleftarrows \text{Complex} \qquad \text{(Eq. 5-1)}$$

The binding reaction with 1:1 stoichiometry can be described as follows (Wiseman *et al.*, 1989):

$$\frac{1}{V_0(\mathrm{d}Q/\mathrm{d}X_{\mathrm{tot}})} = \Delta H^{\circ}\left(\frac{1}{2} + \frac{1-(1+r)/2-X_{\mathrm{r}}/2}{\left(X_{\mathrm{r}}^2-2X_{\mathrm{r}}(1-r)+(1+r)^2\right)^{1/2}}\right) \qquad \text{(Eq. 5-2)}$$

where X_{tot} is the total ligand concentration of free plus bound, in the reaction cell of volume V_0, Q is the heat absorbed or evolved, and ΔH° is the molar heat of binding. The values of r_{L} and X_{r} are dependent on the total ligand concentration and the total macromolecule concentration (M_{tot}),

$$1/r_{\mathrm{L}} = c = M_{\mathrm{tot}}K \qquad \text{(Eq. 5-3)}$$

$$X_{\mathrm{r}} = X_{\mathrm{tot}}/M_{\mathrm{tot}} \qquad \text{(Eq. 5-4)}$$

Binding curves simulated from the Eq. 5-2 is generated in **Figure 5-3**. The parameter n in **Figure 5-3** is the number of identical and independent binding sites for the ligand on the receptor. The parameter, $n, \Delta H^{\circ}$, and K were obtained as the best values of the fitting parameters were investigated.

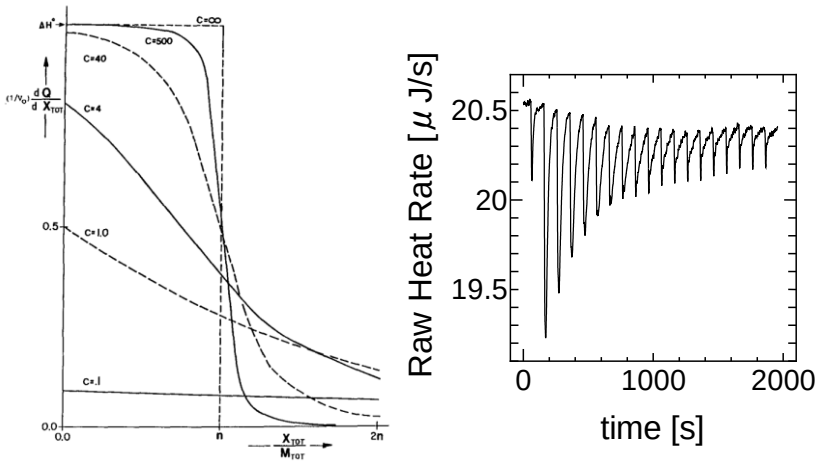

Figure 5-3 (**left**) Simulated binding isotherms for various values of the parameter *c* as introduced in the report (Wiseman *et al*., 1989) (**right**) Raw data obtained for 20 injections wherein 100 μM of poly dC injected into the 20 μM of DOPC vesicle solution.

2.5. Conformational evaluation of nucleic acids by circular dichroism spectroscopy analysis

The conformational effect of the interaction between poly dC and lipid vesicles solution, DOPC and DOPC/Ch, was investigated. The circular dichroism (CD) spectra were measured by JASCO J-820 SFU spectropolarimeter (JASCO, Tokyo, Japan). The CD spectrum from 400 nm to 200 nm was measured with a quartz cell at a scan speed of 100 nm per minute and a width of 1 nm. Three scans were obtained at 25 ℃. The CD spectra of the poly dC were obtained by subtracting the spectra of pure lipid vesicle solution as control. The obtained data was calculated as molar ellipticities. In order to evaluate the step association of poly dC, the CD spectra of the poly dC was measured in the corresponding concentration to the experiments in ITC assay; 20 μM of lipid vesicle solution and the addition of 5, 20, and 40 μl of 100 μM poly dC solution.

3. Results and Discussion

3.1. Dehydration behaviors observed in the emission spectra of Laurdan

Laurdan is a solvent sensitive fluorescence probe locating at the hydrophilic/hydrophobic interface at the lipid bilayer. Therefore, it is possible to assess the effect of dynamic membrane hydration behavior in the adsorption process of the nucleic acids. **Figure 5-4** shows the emission spectra of Laurdan in the POPC/SG and DOPC bilayers under the presence (or absence) of tRNA and poly DNAs, respectively.

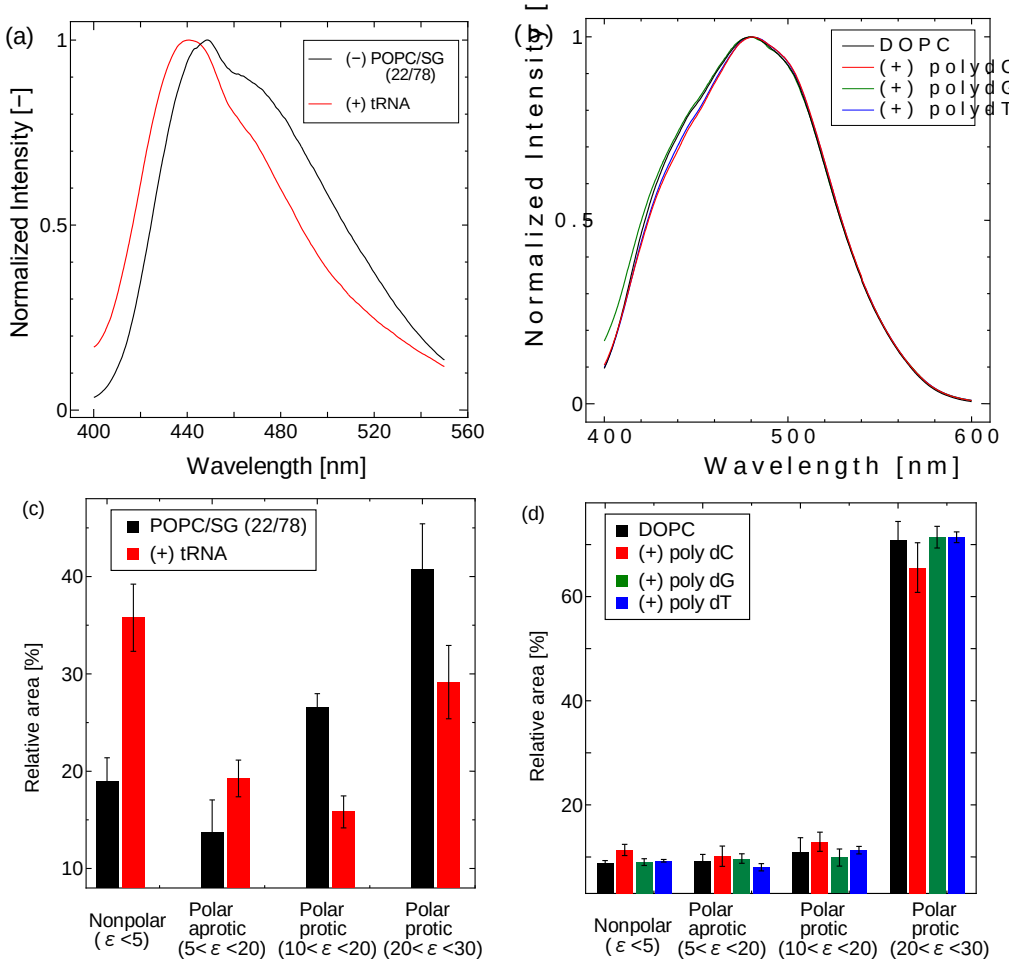

Figure 5-4 Emission spectra of Laurdan **(a)** in the POPC/SG (22/78) bilayers and **(b)** in the DOPC bilayers at 25 °C. The colored spectra were the case of the presence of nucleic acids as represented in the legends. Each spectrum was normalized at the maximum intensity. **(c)** and **(d)** Deconvolution results performed in the same procedure as described in Chapter 2. Each color of bars corresponds to those of spectra.

Addition of tRNA into the POPC/SG vesicle solutions influenced the emission spectra of Laurdan resulting in blue shift. As shown in the result of deconvolution, the increase of "*nonpolar*" component and the decrease of "*polar protic*" component were observed in the presence of tRNA, indicating the blue shift of spectra resulted from the dehydration of membrane polarity. The spectral blueshifts were also observed in other POPC/SG vesicles (POPC/SG = (86/14), (61/39), and (40/60), data not shown), suggesting that the drastic dehydration around the interfacial region of the lipid bilayer was induced under the addition of tRNAs. Given that high affinity of POPC/SG and tRNA was observed, it is considered that the incorporation of tRNA into the lipid membrane surface causes the previously hydrating water molecules released into the bulk solution. On the contrary, the emission spectra in DOPC bilayers did not show any significant differences in the spectral shape and the deconvolution results after the addition of poly DNAs. This result indicates that the addition of oligonucleotides (poly dX) has no influence on the membrane polarities of DOPC bilayer where Laurdan molecules exist.

3.2. Binding affinity of oligonucleotides to DOPC membrane

Isothermal calorimetry was carried out by the injection of oligonucleotide solutions into DOPC bilayers. Titration results for poly dC, poly dG, poly dA, and poly dT are shown in **Figure 5-5**. All the graphs in the upper row are the obtained titration data, and the graphs in the lower row are the integral heat area of each injection. As shown in these results, most of titration curves of oligonucleotide solution were exothermic. Except for poly dC, other oligonucleotides revealed no binding behaviors.

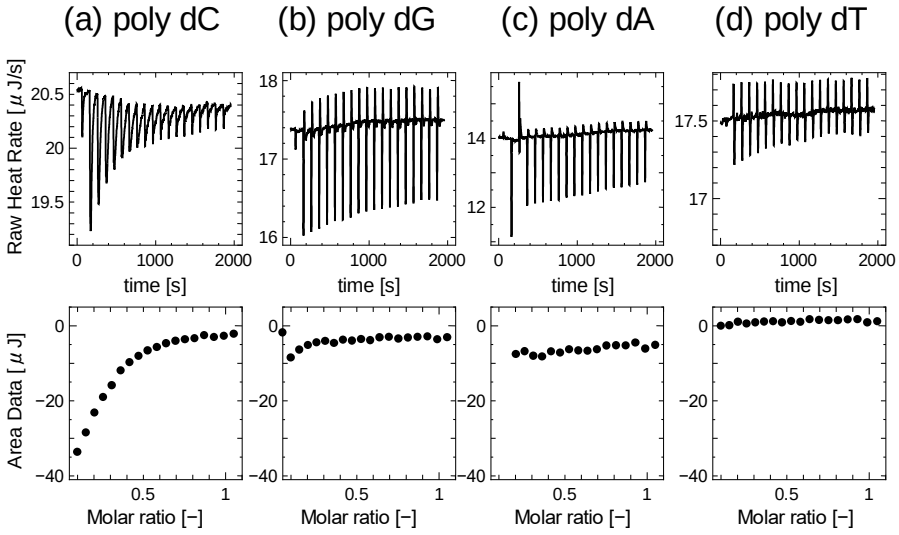

Figure 5-5 ITC results obtained from the titration of **(a)** poly dC, **(b)** poly dG, **(c)** poly dA, and **(d)** poly dT into the DOPC vesicle solutions. The graphs in upper row are the raw heat rate upon the injection time, and the integral area data of titration are shown in the graphs in lower row.

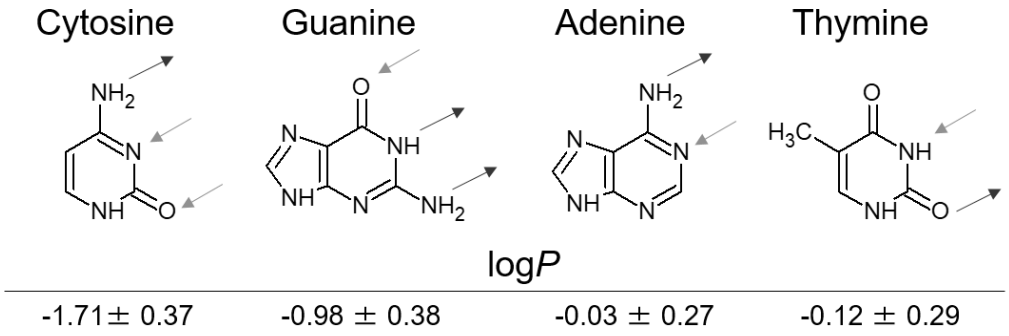

Figure 5-6 Structure of the nucleobases and corresponding log*P* values. Donor and acceptor of the hydrogen bonds are illustrated using arrows colored with dark and light, respectively.

The partitioning behaviors are dependent on the hydrophobicity (log*P* value) of the target molecules. The log*P* values of the base moiety can be calculated using ChemSketch software (ACD/Labs, Canada) as follows: adenine (-0.03 ± 0.27), cytosine (-1.71 ± 0.37), guanine (-0.98 ± 0.38), thymine (-0.12 ± 0.29), and uracil (-0.71 ± 0.29). A higher log*P* value indicates a less polar surface of each compound. Among all types of the nucleobases, the log*P* value of cytosine was the lowest, indicating the hydrophilic cytosine moieties are favorable for the incorporation into the membrane surface. With regards to the conformational properties of the molecules, the cytosine has two hydrogen bonding

acceptor sites, which is the largest number of the hydrogen bonding accessibility among other types of nucleobases (**Figure 5-6**). Although the binding curve was not significant with that of poly dC, the titration curve in poly dG shows a slight decrease of the injection heat, suggesting that guanine moieties are also affective due to its hydrophilic property (low log*P* value) and the plural hydrogen bonding parts. The relatively large injection fluctuations observed in poly dG and poly dA suggest the equilibrium of adsorption and desorption.

The influence of the chain length was investigated for the adsorption of poly dC. **Figure 5-7** represents the binding constants obtained from the titration of different length of poly dC (10, 25, and 50 mer) into DOPC or DOPC/Ch (4/1) vesicle solutions. The values of the binding constant were obtained from the fitting curve using the Eq. 5-2. As shown in the **Figure 5-7**, the longer base chains have higher affinity to the lipid membrane. DOPC/Ch showed higher values of binding constants than that of DOPC, although the difference is not significant. Compared with the binding constant between POPC/SG vesicles and tRNA ($K_a \sim 10^5$ - 10^6 M^{-1}), the scale of the binding constants observed in the system of DOPC (or DOPC/Ch (4/1)) vesicles and poly dC were low, which could explain the slight impact on the Laurdan emission spectra (**Figure 5-4**) under the weak interaction.

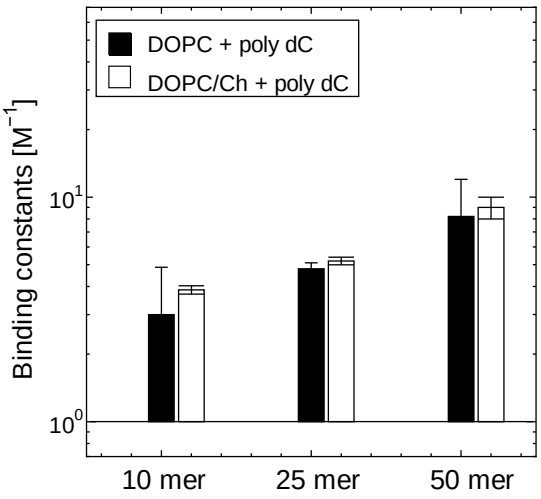

Figure 5-7 The binding constants between lipid and 1mol of poly dC with different length (10, 25, and 50 mer) calculated from the fitting of the titration data according to the Eq. 5-2.

3.3. Implication of dehydration during the interaction between POPC/SG and tRNA

In order to consider the difference of the interaction in POPC/SG system and DOPC system, the evaluation of thermodynamic parameters were attempted. In the model of ITC experiments, the thermodynamic parameters during the binding was obtained. Regarding the POPC/SG system, the strong interaction with tRNA could cause the aggregation of vesicles generating the precipitation, which is not favorable for the ITC measurements. Hence, the application of dehydration behavior monitored by Laurdan was focused.

In Chapter 3, the number of hydration water molecules per lipid was calculated. In the various situations such as membrane phase transition for several types of lipid bilayers or membrane phase separation in binary components, the obtained number of hydration water molecules were compared with the corresponding *GP* values, which is the value that can be obtained from the steady-state emission spectra of Laurdan. As shown in **Figure 5-8**, a linear relationship was obtained between the number of water molecules and *GP* values.

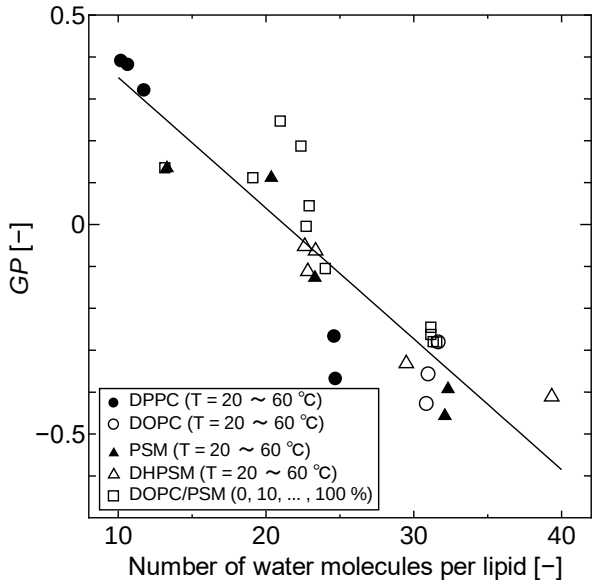

Figure 5-8 Correlation between the number of water molecules per lipid and the conventional *GP* values. The number of water molecules were calculated as explained in the Chapter 3. *GP* values were calculated according to the report (Parasassi *et al*., 1991).

Herein, the contribution of dehydration was furthermore discussed based on the difference of *GP* values. The hydration between lipid and water molecules can be described as follows:

$$\text{lipid} + n\ \text{water} \overset{K_\text{a}}{\rightarrow} \text{lipid} - n\ \text{water complex},$$

$$K_\text{a} = \frac{[\text{lipid}-n\text{water complex}]}{[\text{lipid}][\text{water}]^n} \qquad \text{(Eq. 5-5)}$$

The change of Gibbs free energy in the hydration can be defined as

$$\Delta G = -RT\ln K_\text{a} \qquad \text{(E. 5-6)}$$

Since the concentration of the water molecules are enough high than that of lipid molecules ([lipid] << [water]), the ΔG can be described as follows:

$$\Delta G = -RT\ln K_\text{a} = -RT\ln\left(\frac{1}{[\text{water}]^n}\right) = nRT\ln([\text{water}]) \qquad \text{(Eq. 5-7)}$$

If the *GP* value is proportional to the number of water molecules *n* ($GP \propto n$), the change of free energy between the different hydration states upon binding can be described as follows:

$$\begin{aligned}\Delta G_\text{hydration} &= \Delta nRT\ln([\text{water}]) \\ &= \frac{\Delta GP}{I_{GP}}RT\ln([\text{water}]) \qquad \text{(Eq. 5-8)}\end{aligned}$$

where the I_{GP} is the slope of the correlation between *GP* and *n*. Upon this assumption it is possible to calculate the contribution of dehydration process.

Pozharski *et al*. have previously investigated the interactions between cationic lipid and DNA, where the association could occur in the manner with large entropic term (Pozharski *et al.*, 2003). Regarding the questions of the entropy loss generated by the binding, the contribution of the reduced dimensionality of the system into the free energy of binding is ~3.5 Å*RT*/(2a) ~8.3 J/mole (assuming DNA persistence length a ~500 Å), which is negligible compared with the overall binding energy. Hence, in the system of POPC/SG vesicles and tRNA, the contribution of entropy (ΔS) can be assigned with the free energy change of dehydration $\Delta G_\text{hydration}$. From the assumption of $\Delta H = \Delta G + T\Delta S$, the enthalpy change can be calculated using the binding constants obtained in Chapter 4 (calculated based on the binding constants of tRNA). Thermodynamic behavior of the interaction at lipid membrane will be discussed in the following section.

3.4. Enthalpy-entropy compensation at lipid membrane

It has been reported that a strong positive correlation is established between ΔH and ΔS in many chemical reactions and chemical equilibrium systems (Lumry *et al.*, 1970; Olsson *et al.*, 2011; Rekharsky *et al.*, 2007). The relationship of ΔS and ΔH in the POPC/SG vesicles and tRNA system was investigated as a model of strong interactions using the values obtained based on the dehydration and the free energy change, respectively. As the weak interaction model, the system of DOPC (or DOPC/Ch) bilayers and oligonucleotides was selected for the discussion by using the thermodynamic parameters obtained from the ITC measurements. **Figure 5-9** shows the relationship between ΔH and $T\Delta S$ found in the interactions at the lipid membranes.

As shown in this figure, most of the results were appeared in the positive linear relation. The series of interaction at POPC/SG vesicles were appeared positive side of the identical correlation (black line). Cationic lipid vesicles (DOPC/DOTAP, and DOPC/DC-Ch) were appeared on the similar line, suggesting the interaction behavior could resemble that of POPC/SG vesicles. The upper side of the correlation indicates the large

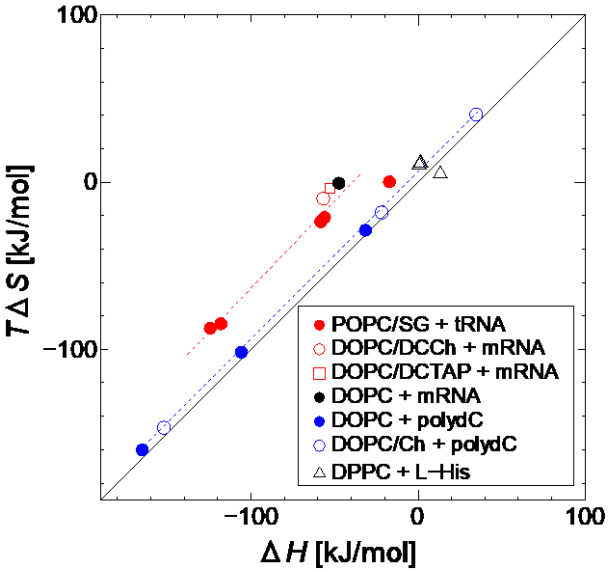

Figure 5-9 Enthalpy-entropy compensation at the lipid membrane. The pairs of interactions are explained in the legend. Identical correlation was depicted with the linear black line. Series of POPC/SG vesicles with tRNA and series of DOPC (or DOPC/Ch) bilayers with poly dC were represented with the linear fitting line with the color red and blue, respectively. The other results were obtained from the previous studies (Ishigami *et al.*, 2015; Suga *et al.*, 2011).

contribution of the entropy, which requires the dissipative change in the system when the interaction occurs. In the system of DOPC or DOPC/Ch bilayers with poly dC, the plots showed complementary relation, which means the contribution of the ΔH and ΔS is identical. Chiral recognition of $_{L}$-His on the DPPC bilayer appeared on the same line. The binding constants of chiral recognition could occur with the scale of (K_a < 10 M^{-1}), suggesting that the "*weak interaction*" is a key to perform molecular selective association at lipid membrane, which follows the enthalpy-entropy compensation. Besides, the selection of molecular morphology could be generated with a weak interaction by cooperatively adjusting the molecular arrangement near the lipid molecules as the second step after the adsorption.

4. Summary

The evaluation of the various interaction at the lipid membrane was performed in the aspects of the difference of the interaction force degree. The "*strong interactions*" (K_a > 10^4 M^{-1}) that affect the dehydration of the membrane close to the hydrophilic/ hydrophobic interface would generate the large contribution of entropy among the association. The estimation of the free energy change during the dehydration was performed using the hydrating water number and conventional *GP* values. Besides, these obtained values followed the low of enthalpy-entropy compensation, suggesting the evaluation of thermodynamic behavior could be established by the fluorescence analysis. The "*weak interactions*" (K_a < 10^2 M^{-1}) were observed in the system of small nucleotides such as poly dC and in the system with amphiphilic DOPC molecules in the identical manner of enthalpy and entropy contribution. In this system, the selective adsorption of cytosine was observed, which could be due to the hydrophilic property and the possible number of hydrogen bonding acceptors. As indicated with the chiral recognition of the amino acids, the "*weak interactions*" could induce the selectivity by modulating the plural interactions in the cooperative manner. This systematic comprehension of the interactions at the lipid membrane could provide important view for the design of the self-assembly system (**Figure 5-10**).

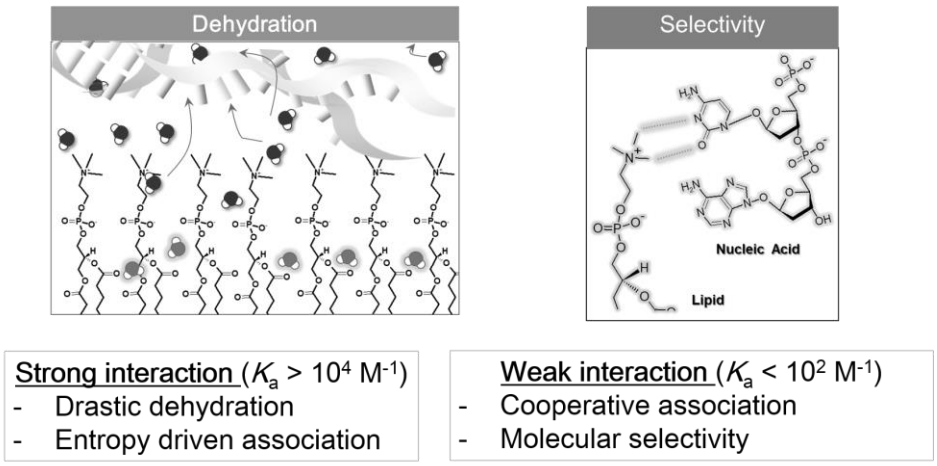

Figure 5-10 Conceptual summary in this chapter.

Chapter 6

Cooperative Effects of

Guanidinium-modified Lipid Membrane

1. Introduction

Lipid bilayer vesicles have been reported to influence the configuration of binding molecules (Walde, 2010; Walde *et al*., 2014): molecular chaperone-like activity in peptide folding (Yoshimoto *et al*., 2015), regulation of enzymatic activities (Umakoshi *et al*., 2008), and conformational change of DNA (Tsuji and Yoshikawa, 2010). In previous studies, it is shown that the lipid membranes act as a platform for regulating RNA conformation (Suga *et al*., 2011, 2013, 2016a). In particular, such biomolecule−membrane interactions may influence the *in vitro* gene expression system (Bui *et al*., 2010). RNA molecules interact with cationic liposomes, where strong electrostatic interactions between RNA and cationic lipid in liquid-disordered phases can induce unexpected denaturation in RNA, leading to a loss of RNA function (Suga *et al*., 2011). Therefore, a rational design for the conformation property is required in the self-assembly systems wherein several noncovalent forces are working simultaneously.

Conformation properties of lipid membrane surface is not simple. Zwitterionic phospholipids are commonly used as neutral lipids to construct vesicles. However, the surface charge densities of the vesicle are usually negative (Klasczyk *et al*., 2010). One dominant factor to control the surface charge of vesicles is the orientation of lipid head group. Orientation can be affected by the ionic strength, or phase state, of the vesicle (Suga *et al*., 2016). The charge neutralization of a negative phosphate group in zwitterionic phospholipid by cationic lipid increased the lipid packing density, which conferred an overall cationic charge on the membrane due to the “upright” choline group (Troutier *et al*., 2005). In above examples, the cationic lipids, cetyl-trimethylammonium-bromide (CTAB) and DOTAP, are mainly applied to construct membranes with neutral lipid membrane 1,2-dioleoyl-s*n*-glycero-3-phosphoethanolamine (DOPE). In such a system, the cationic moieties of the cationic surfactant are electrically neutralized by the phosphate group of DOPE lipid, and the deprotonation of amino moiety of DOPE has a

significant influence on the interaction with DNA molecules (Lobo *et al*., 2001). In another system with Ca^{2+} ions to induce the aggregation with nucleic acids on the lipid membrane, the binding mechanism was expected that the neutralization of phosphate by Ca^{2+} ion adjusts the orientation of cationic choline group resulting in the adsorption of external molecules (McManus *et al*., 2003). Therefore, the head group orientation of the zwitterionic phospholipid molecules is a key factor for controlling the characteristics of membrane surface, which contributes to the accumulation of guest molecules.

The phase states of the lipid membrane would affect the interaction with external biomacromolecules. It is expected that the phase transition of the lipid membrane under the heating condition induces the distribution of the binding sites, resulting in the increase of contact frequency. Besides, the apolar region of the lipid membrane could be exposed after the phase transition, and it enhances the hydrophobic interaction with the external molecule whose the structure is denatured and energetically unstable under the high temperature. Incorporation of nucleic acid molecules during the phase transition of lipid membrane was experimentally observed from the difference of differential scanning calorimetry (DSC) measurements (Giatrellis and Nounesis, 2011). For the guanidinium modified membrane as shown in the results of membrane property analysis in Chapter 4, the SG-modified membrane revealed highly ordered and hydrophobic properties. On the other hand, the MA-modified membrane showed high fluidity with hydrophilic membrane properties. From the analysis of IR spectroscopy, the effect of guanidinium modification was discussed focusing on the behaviors of the phosphate group (-P=O) and carbonyl group (-C=O) around the membrane interface. Since the SG-modified membranes indicated high affinities to tRNA, it is important to clarify the membrane structures such as the head group orientation and the heat effects for the phase transition.

In this chapter, the cooperative effects of the guanidinium modification were evaluated focusing on the configurational impact on the surface charge state. The apparent pK_a values were analyzed from the observation of pH dependencies on the fluorescence intensity of 2-*p*-toluidinylnaphthalene-6-sulfonate (TNS) and the effects of the modification on the head group orientation were discussed. Furthermore, the phase transition behavior of POPC/SG vesicles was investigated in the aspects of the configurational impacts on the tRNA molecules.

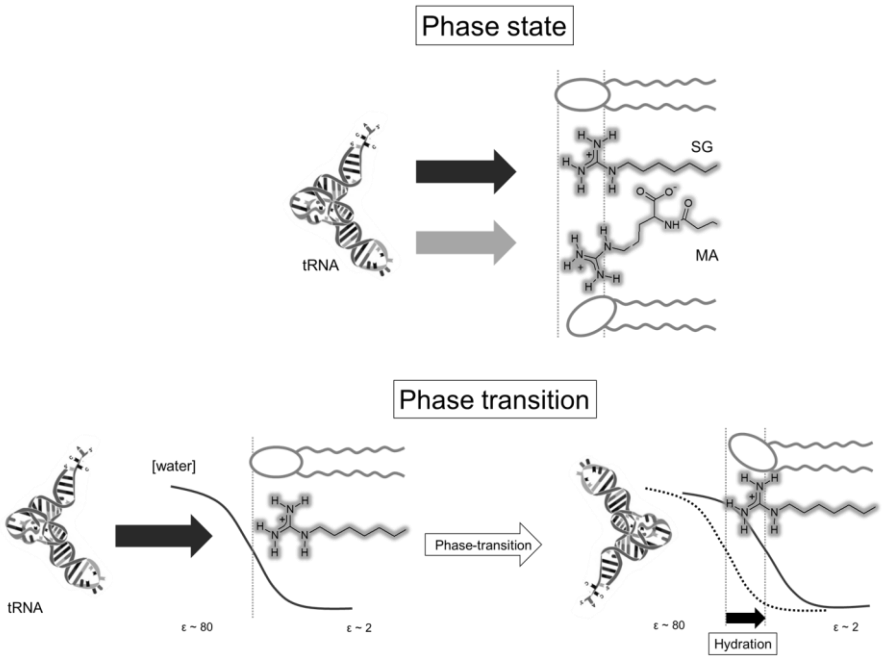

Figure 6-1 Conceptual illustration in this chapter.

2. Materials and Methods

2.1. Materials

1-Palmytoyl-2-oleoyl-*sn*-glycero-3-phosphocoline (POPC) was purchased from Avanti Polar Lipids, Inc. (Alabaster, AL, USA). Stearylguanidinium and myristoylarginine were synthesized as explained in Chapter 4 (see Section 4.2.2.). tRNA originating from *Escherichia coli*, fluorescence probes (TNS, 6-lauroyl-2-dimethyl aminonaphthalene (Laurdan), and 1,6-diphenyl-1,3,5-hexatriene (DPH)) were purchased from Sigma Aldrich (St. Louis, MO). Other chemicals were purchased from FUJIFILM Wako Pure Chemical Corporation (Osaka, Japan). All chemicals were used as received.

2.2. Vesicle preparation

POPC and SG or MA with different ratios were dissolved in chloroform in a round-bottom flask. The solvent was removed by rotary evaporation. The obtained thin layer was kept under a high vacuum for more than 3 h. After the addition of 1000 μL Tris-HCl buffer (100 mM, pH 8.0) to disperse the lipids, five cycles of freezing and thawing (−80 ℃/50 ℃) were carried out to obtain the aqueous suspension of guanidinium modified vesicles. Extrusion treatment, in which the vesicle suspension was passed through a polycarbonate filter membrane with a pore diameter of 100 nm, was repeated 11 times using a Liposofast extrusion device (Avestin Inc., Ottawa, ON, Canada). Milky-white suspensions were observed for both POPC/SG and POPC/MA vesicles, indicating the formation of bilayer vesicles, because this turbidity cannot be detected with a micelle suspension. After extrusion, vesicle suspensions were kept in 4 ℃ until used.

2.3. Characterization of membrane surface charge using TNS

The fluorescence intensity of TNS was measured under the pH titration. The pH of each sample was adjusted to pH ~12 using NaOH aq, and then was incubated for 30 min in dark place (30 ℃). The pH of dispersions including 500 μM of lipids and 20 μM of TNS were titrated by the addition of HCl aq. using alkali-resistant pH electrode (LAQUA, Horiba, Ltd., Kyoto, Japan). The emission spectrum of TNS (Ex. 340 nm) at each pH value was measured by Spectrofluorometer (FP-8500; Jasco, Tokyo, Japan). The TNS

peak intensities were normalized, then the sigmoidal curves were obtained. To calculate the apparent pK_a value, a midpoint in each curve was defined as pK_a.

The deprotonation state can be evaluated according to the Henderson-Hasselbalch equation using the obtained pK_a value as follows (Henderson, 1908; Weast, 1983):

$$[PO_2^-] + [PO_2H] + [\text{SG or MA}] = 1 \quad \text{(Eq. 6-1)}$$

$$\text{pH} = \text{p}K_a + \log(([PO_2^-]) \,/\, (PO_2H)), \quad \text{(Eq. 6-2)}$$

where [PO_2^-], [PO_2H], and [SG or MA] represent mole fraction of ionized POPC, protonated POPC, and SG or MA, respectively. Cation ratio [-] was calculated as follows;

$$\text{Cation ratio} = {([PO_2H] + [\text{SG or MA}])}/{1}, \quad \text{(Eq. 6-3)}$$

2.4. Membrane property analysis using Laurdan

The generalized polarization (GP_{340}) for vesicles were evaluated by Laurdan spectra (Hirsch-Lerner *et al.*, 1999; Parasassi *et al*., 1998). The lipid concentration was 100 μM, and each sample volume was 1 mL, including 1 μM of Laurdan. The sample solution was incubated at 30 ℃ for 30 min in dark, before measurement. The emission spectrum of Laurdan (Ex. 340 nm) was measured at different temperatures, then the GP_{340} value for each vesicle was evaluated as follows:

$$GP_{340} = (I_{440} - I_{490}) \,/\, (I_{440} + I_{490}) \quad \text{(Eq. 6-4)}$$

where I_{440} and I_{490} are the emission intensity of Laurdan at 440 and 490 nm, respectively.

2.5. Membrane property analysis using DPH

Membrane fluidities in the interior region were evaluated in the same manner as described in previous reports (Hayashi *et al*., 2011; Yoshimoto *et al*., 2007). DPH was added to a vesicle suspension (lipid/probe molar ratio was 250:1). The lipid concentration was 100 μM, and each sample volume was 1 mL, including 0.4 μM of DPH. The sample solution was incubated for 30 min in dark before measurement. The fluorescence intensities of DPH (Ex. 360 nm) were measured by using a fluorescence spectrophotometer (FP-6500; JASCO, Tokyo, Japan). The emission intensities at 430 nm, both perpendicular ($I_{\perp}$) (0 °, 0 °) and parallel ($I_{/\!/}$) (0 °, 90 °) to the excited light, were recorded when the sample was excited with vertically polarized light (at 360 nm). Thereafter, the polarization (P) of DPH and correlation factor (G) were then calculated

based on the following equations:

$$P = (I_{\parallel} - GI_{\perp}) \ / \ (I_{\parallel} + GI_{\perp}) \quad \text{(Eq. 4-3)}$$

$$G = i_{\perp} / i_{\parallel} \quad \text{(Eq. 4-4)}$$

Herewith, $i_{\perp}$ and $i_{//}$ represent emission intensity perpendicular to the horizontally-polarized light (90 °, 0 °), and that parallel to the horizontally-polarized light (90 °, 90°), respectively. The obtained value (1/*P*) was utilized to the calculation of membrane fluidity.

2.6. CD spectra analysis

The conformational changes in tRNA in the absence or presence of vesicles were evaluated by spectropolarimeter (J-820 SFU, JASCO, Tokyo, Japan) (Suga *et al*., 2010, 2012). The circular dichroic (CD) spectrum was recorded from 300 to 200 nm using a quartz cell (0.1 cm path length), where scan speed was 100 nm/min, and slit width was 1 nm. Three scanned data were accumulated, then background signals (obtained from buffer or vesicle suspension) were removed to gain the data as molar ellipticity of tRNA (Suga *et al*., 2013). The total concentration of tRNA was 2 μM in the presence or absence of vesicles (total lipid: 250 μM). The measurements were carried out using 10 mM Tris-HCl at pH 7.8 buffer, under the controlled temperature: heating from 30 to 80 ℃.

2.7. Calculation of melting temperature

tRNA is intact at 30 ℃ and is fully denatured at 80 ℃ (Suga *et al*., 2010). The melting temperature (T_m) of tRNA was calculated from the CD data. The positive peak at around 265 nm (θ) was normalized on the basis of following (Suga *et al*., 2010),

$$\Delta\theta(T) = \frac{\theta(T) - \theta(30℃)}{\theta(80℃) - \theta(30℃)} \ [-] \quad \text{(Eq. 6-7)}$$

where the value of θ was minimum at 30 ℃ (θ(30 ℃)) and was maximum at 80 ℃ (θ(80℃)). The temperature with $\Delta\theta$ = 0.5 was defined as the melting temperature, T_m. The $\Delta\theta$ values were fitted by following equation, and T_m was estimated from the fitting equation in which the value of $\Delta\theta$ equals to 0.5.

$$\Delta\theta(T) = \frac{\Delta\theta(30℃) - \Delta\theta(80℃)}{1 + e^{(T - 30℃)/dT}} + \Delta\theta(80℃) \quad \text{(Eq. 6-8)}$$

2.8. Analysis of peak shift in CD spectra

The shift of the wavelength maximum at around 265 nm was estimated based on the following equation.

$$\Delta\lambda(T) = \frac{\lambda(T) - \lambda(30℃)}{\lambda(80℃) - \lambda(30℃)} \quad \text{(Eq. 6-9)}$$

The $\Delta\lambda$ obtained were fitted based on the following sigmoid function:

$$\Delta\lambda(T) = \frac{\Delta\lambda(30℃) - \Delta\lambda(80℃)}{1 + e^{(T - 30℃)/dT}} + \Delta\lambda(80℃) \quad \text{(Eq. 6-10)}$$

The $\Delta\lambda$ value was calculated using the estimated T_m value.

3. Results and Discussion

3.1. Electrostatic potentials of guanidinium-modified vesicles

To estimate the surface charge density of guanidinium vesicles, the zeta potentials were measured (**Table 6-1**).

Table 6-1 Zeta potential of vesicles at pH 7.8

Vesicle	ζ [mV]
POPC	-9.6 ± 5.9
POPC/SG = 9/1	42.3 ± 12.5
POPC/SG = 7/3	56.5 ± 7.2
POPC/SG = 5/5	46.5 ± 5.1
POPC/SG = 3/7	51.6 ± 5.6
POPC/MA = 9/1	-28.4 ± 14.5
POPC/MA = 7/3	-46.8 ± 21.4
POPC/MA = 5/5	-65.1 ± 16.8
POPC/MA = 3/7	-25.6 ± 9.5

The zeta potential values of POPC/SG vesicles were positive, and the values were almost constant (40−50 mV) independent of the SG ratio. Quantitative characterization for the surface charge density based on zeta potential could be difficult (Suga *et al*., 2016b). These results suggest that the molecular interaction between SG and POPC molecule neutralizes the anionic phosphate group in POPC, exposing the cationic moiety (choline or guanidinium group) to the bulk aqueous phase. Previous study that examined the bending state of DMPC, DPPC, and DSPC head groups also revealed that the phosphate group could be exposed to bulk water (Makino *et al*., 1991). It is assumed that the head group orientation in POPC vesicles is a controlling factor for the surface charge density of the membrane. Based on these points, it is suggested that the negative charge in zeta potential measurements are due to the exposure of phosphate groups in POPC (bent head group). According to **Table 6-1** (ζ values), the negative surface charges of POPC and POPC/MA vesicles were due to the exposure of phosphate groups (POPC) to the bulk water, whereas POPC/SG vesicles showed positive surface charges due to the exposure of cationic guanidinium (SG) or choline (POPC) groups to pH 7.8 bulk water. The presence of cationic lipids leads to the upright orientation of the bent head groups, suggesting that the actual cationic moiety is the choline group of PC in the mixture of PC and cationic lipids (Troutier *et al*., 2005). Also, the surface charge densities of vesicles

are related to the packing state (Sehgal *et al*., 1979; Vogel *et al*., 1988a, 1988b). The collective data indicate that the orientation of the POPC head groups and chain packing can be modified by the interaction with SG molecules. The molecular orientation in POPC and guanidinium derivatives is shown in the side-view in **Figure 6-2**. In the positively charged POPC/SG vesicles, the cationic choline group is upright toward the bulk aqueous phase, which is induced by high affinity of tRNA to SG vesicles as shown in Chapter 4. POPC/MA vesicles display negatively charged surface potentials. MA molecules have both a negatively charged carbonyl groups and positively charged guanidinium groups. In addition to the phosphate-guanidinium interactions, it is expected that the negatively charged carboxyl groups exert strong electrostatic interactions with the positively charged choline groups. As a result of interactions between the head groups, the negatively charged moieties (phosphate group of POPC and carboxyl group of MA) could be exposed to the bulk aqueous phase, performing negative ζ values of POPC/MA vesicles (**Figure 6-2**, top-view). Based on the assumption of head group orientation, it is obvious that POPC/SG vesicles were densely packed with a cationic charged state, especially in higher modification, compared with POPC/MA vesicles. However, it is difficult to monitor the local electrostatic potentials at membrane surfaces by zeta potential estimation, while the studies using fluorescent probes provide important insights into the localization of electrostatic properties (Pierrat *et al*., 2015).

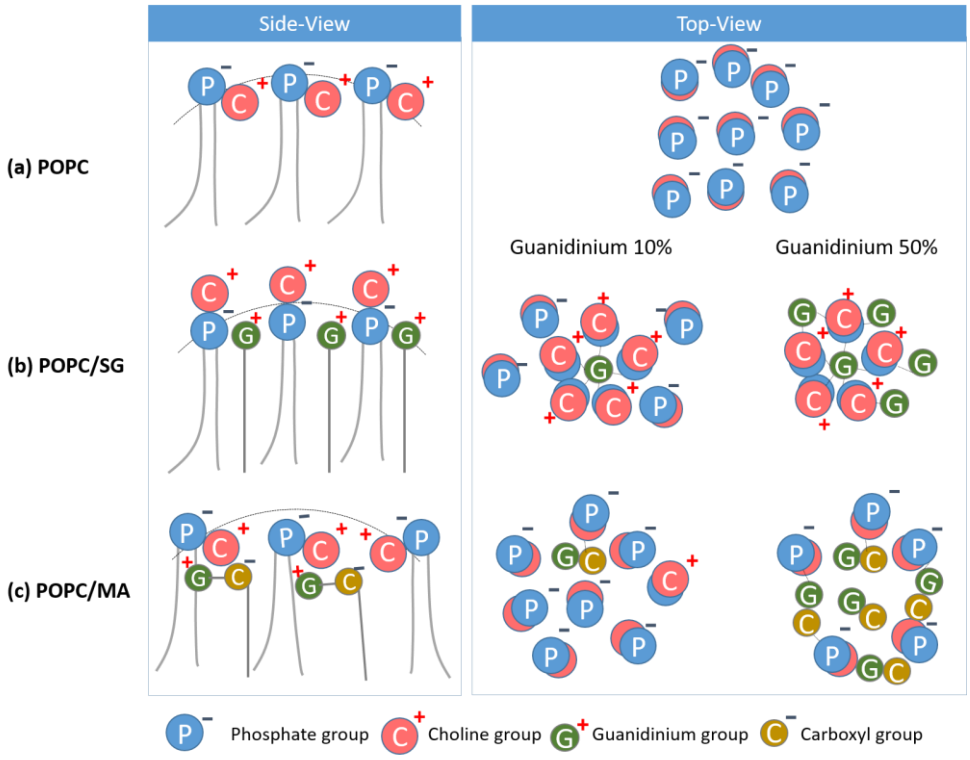

Figure 6-2 Plausible membrane models of **(a)** POPC, **(b)** POPC/SG, and **(c)** POPC/MA vesicles.

3.2. pK_a values from TNS fluorescence assay

The fluorescence of TNS has been used to investigate lipid ionization, depending on pH (Jayaraman *et al.*, 2012; Pierrat *et al.*, 2015). For the cationic lipid membrane, TNS probes are strongly anchored due to the electrostatic interactions, whereas hydrophobic interactions are the dominant attracting forces in distribution to neutral and anionic membranes. Therefore, the contributions of electrostatic and hydrophobic interactions sensitively influenced the partitioning of TNS (Pierrat *et al.*, 2015). The apparent pK_a values of TNS in lipid membranes can be determined by pH titration. Normalized fluorescence intensities are employed to draw titration curves (Pierrat *et al.*, 2015). Presently, the TNS fluorescence intensities responding to surrounding pH were measured and the apparent pK_a value was estimated based on Boltzmann equation fitting (Henderson, 1908; Weast, 1983). **Figure 6-3 (a**) shows the titration curve of POPC. The predicted pK_a value was ~3.4, indicating that deprotonation of the phosphate component can be induced at approximately pH 2.12 (Henderson, 1908) (**Table 6-2**). Therefore, the apparent pK_a could reflect the deprotonation of the phosphate group of POPC. **Figure 6-**

3 (b) and **(c)** display titration curves of POPC/SG and POPC/MA vesicles. In both cases, the inflection points (pK_a) shifted to higher pH. For POPC/MA vesicles, the pK_a values shifted as compared to those of POPC vesicles, but the shifts were smaller than those of POPC/SG vesicles. As shown in the analysis of FT-IR spectra in Chapter 4, the peak shifts of phosphate groups (stronger for hydration) occurred with the increase of MA molecule ratio in a dose-dependent manner. This suggests that MA molecules work to avoid the deprotonation of phosphate group by hydrogen bonding interaction. The results indicate that MA molecules interact with the phosphate group of POPC in sufficient quantity to interrupt deprotonation, but do not lead to a change to a positive surface charge density of the membrane. The degree of deprotonation was estimated to evaluate the molecular structural and charge states.

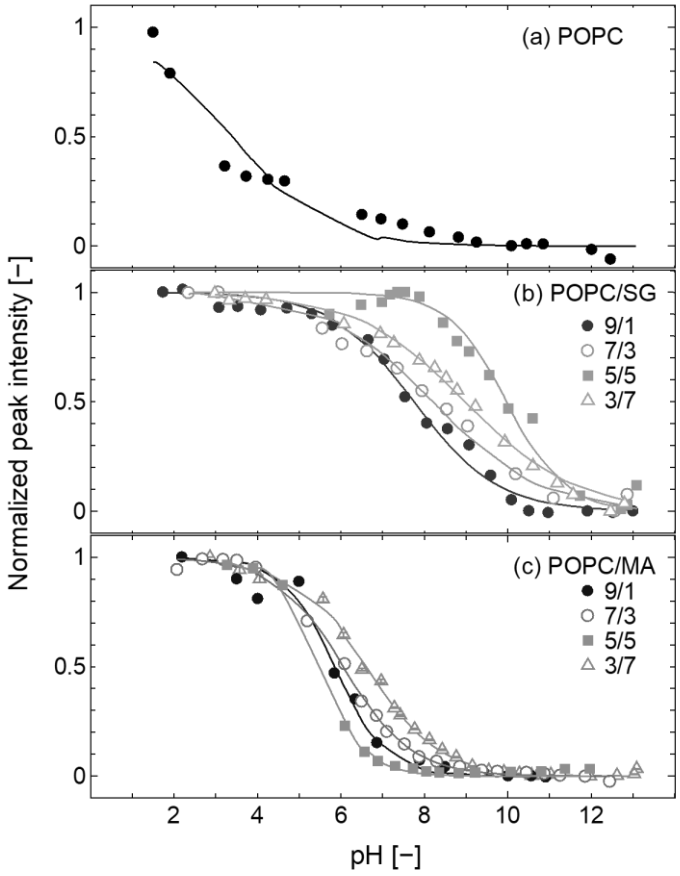

Figure 6-3 pH titration curves of normalized TNS fluorescence intensity for **(a)** POPC, **(b)** POPC/SG, and **(c)** POPC/MA vesicles. Total concentration of lipid and TNS were 100 and 1 μM, respectively. All measurements were conducted at 30 ℃.

Table 6-2 pK_a values and estimated cation ratios

Vesicle	pK_a [-] [a]	Cation ratio [-](at pH 7.8) [b]
POPC	3.4	4.2×10^{-3}
POPC/SG = 9/1	7.8	5.2×10^{-1}
POPC/SG = 7/3	8.2	8.0×10^{-1}
POPC/SG = 5/5	10.0	9.9×10^{-1}
POPC/SG = 3/7	9.0	9.8×10^{-1}
POPC/MA = 9/1	6.0	1.4×10^{-7}
POPC/MA = 7/3	6.1	1.1×10^{-8}
POPC/MA = 5/5	5.5	7.9×10^{-9}
POPC/MA = 3/7	6.6	4.8×10^{-9}

[a,b] Calculated based on the data shown in Figure 6-3.

Cation ratio indicates the molar fraction of cationic molecules within total lipid molecules (**Table 6-2**). In POPC/SG vesicles, cation ratios increased in proportion to the SG ratio, which agrees with the positive zeta potentials (**Table 6-1**). In particular, POPC/SG = 9/1 exhibited a cation ratio of 0.52, which means that 0.1 SG molecules ionized 0.42 POPC molecules. Based on DPH and Laurdan analyses in Chapter 4, SG molecules in POPC/SG = 9/1 could be scattered. This indicates that a SG molecule incorporated in POPC membranes can interact with surrounding POPC molecules. For SG > 30%, no significant differences were seen both in zeta potential and cation ratio. On the other hand, POPC/MA vesicles showed quite low cation ratios at pH 7.8, suggesting that the guanidinium moiety of MA hardly leads to the protonation of surrounding POPC molecules.

The intermolecular interaction model is illustrated in **Figure 6-2** (top-view). In the POPC vesicles, most of the phosphate groups were exposed to the bulk aqueous phase (head group bending). In POPC/SG vesicles, the guanidinium moiety of SG strongly interacted with phosphate groups of POPC, which decreased the exposure of phosphate groups to the bulk water (head group upright). POPC/SG displayed highly packed membrane states in which SG sufficiently interacted with neighboring POPC molecules. In POPC/MA vesicles, the guanidinium-phosphate interactions were revealed by FT-IR and TNS fluorescence analyses. However, almost all the POPC molecules were ionized irrespective of the MA modification. That could force the head groups into a bent-down orientation, exposing the phosphate groups and resulting in a negatively charged surface.

3.3. Membrane phase state of guanidinium-modified membrane

Based on Cartesian diagram analysis, the vesicles plotted in the second quadrant ($1/P < 6$, $GP_{340} > -0.2$) were in the ordered phases (s_o or l_o), and those in the fourth quadrant ($1/P > 6$, $GP_{340} < -0.2$) were in the liquid-disordered (l_d) phases (Suga *et al*., 2013). The increase in GP_{340} values was observed with increasing SG amounts, revealing the formation of SG-enriched ordered phases (**Figure 6-4 (a)**). It has been reported that the SG molecule makes the membrane phase heterogeneous (Onda *et al*., 1996). The GP_{340} values decreased with increasing temperature, indicating that the SG-enriched ordered phase can melt at high temperatures. In the report by Mouritsen (Mouritsen, 2010), the liquid-ordered phase could account for the existence of an intermediate phase, i.e., a phase that is ordered from the perspectives of the conformational structure of the lipid chains but is disordered from the perspectives of the lateral positions of the molecules. In the point of view from DPH and Laurdan analyses (**Figure 6-4 (a)**), solid/ordered (s_o) phase (i.e. DPPC) did not show temperature dependency on membrane properties, while l_o phase (DOPC/Ch = (5/5)) showed slight temperature dependency. POPC/SG vesicles also showed slight temperature dependency on $1/P$ and GP_{340} values. Thus, it could be assumed that SG molecules lead the membrane ordered, and thus l_o-like phase can be formed, similar to the l_o phases formed in the POPC/Ch vesicles. Judging from the $1/P$ and GP_{340} values, the phase diagram of POPC/SG vesicles were summarized (**Figure 6-4 (b)**). At 30 ℃, the phase state of POPC/SG = (86/14) was l_d phase, while those of POPC/SG = (61/39) and POPC/SG = (40/60) were in heterogeneous (l_d+l_o-like) phases. Paleos *et al* reported that guanidinium-phosphate interactions can lead to morphological changes (micelle-to-vesicle transformations) because of the ion pair formation (Paleos *et al*., 1999). Thus, the interaction between POPC and SG may have induced tight packing of the membrane. Because of the phosphate group in POPC, the packing density of the membrane was increased by a strong interaction between POPC and SG head groups. The saturated alkyl chain of SG molecule may also contribute to form ordered phases, resulting in decreased membrane fluidities in POPC/SG vesicles. In the following section, the interaction between POPC/SG vesicles and tRNA was investigated during the phase transition.

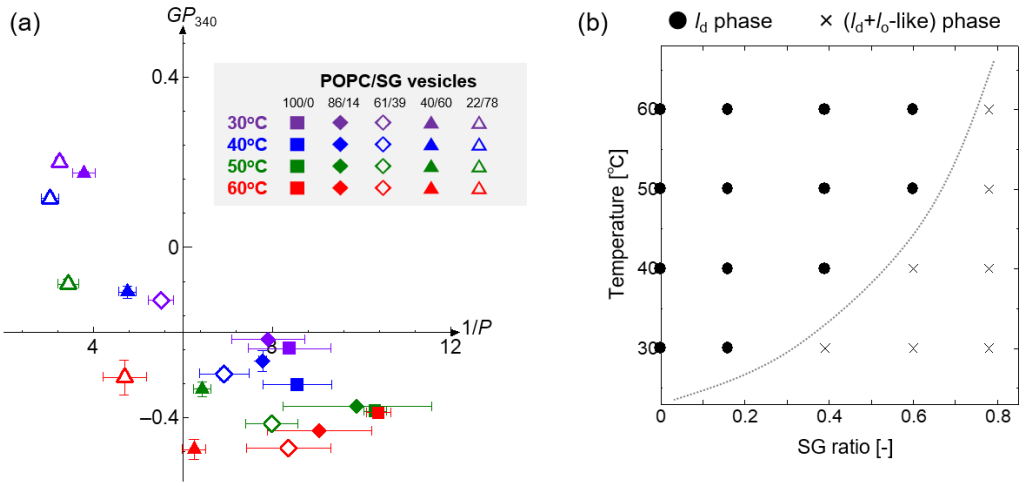

Figure 6-4 (a) Cartesian diagram (Suga *et al.*, 2013) for POPC/SG vesicles at different temperatures. 1/*P* and GP_{340} values indicate the membrane fluidity and polarity, respectively. When the vesicle membrane becomes polar (GP_{340} decrease), its fluidity becomes higher (1/*P* increase). Vesicles plotted in the second quadrant (1/*P* < 6, GP_{340} > -0.2) and in the fourth quadrant (1/*P* > 6, GP_{340} < -0.2) were considered in disordered phases and in ordered phases, respectively. Symbols indicate POPC (*square*), POPC/SG= (86/14) (*closed diamond*), POPC/SG = (61/39) (*open diamond*), POPC/SG= (40/60) (*closed triangle*), and POPC/SG = (22/78) (*open triangle*), respectively. **(b)** Phase diagram of POPC/SG binary systems. The vesicles showing 1/*P* > 6 and GP_{340} < -0.2 are considered in l_d phase, otherwise in (l_d+l_o-like) phase.

3.4. Conformational change in tRNA in the presence of POPC/SG vesicles analyzed by CD measurements

The conformational changes in tRNA in the presence of POPC/SG vesicles were characterized by using CD spectra. tRNA, which is in the A-form double-helix conformation, shows negative and positive CD peaks at 208 and 265 nm, respectively (Carmona *et al.*, 1999; Gregoire *et al.*, 1997). The positive peak at around 265 nm can be considered an indicator of base stacking (formation of intra-molecular base pair), and the negative peak at 208 nm can be an A-form marker (Clark *et al.*, 1997). While there is a difficulty in precise prediction of the tRNA conformation owing to its large molecular weight and flexibility in conformation, the obtained CD data indicated that the tRNA molecules were in A-form conformation with and without POPC/SG vesicles (**Figure 6-5**). To evaluate the conformational stabilities of tRNA further, the peak intensity ($\Delta\theta$) and peak shift ($\Delta\lambda$) were measured under heating conditions.

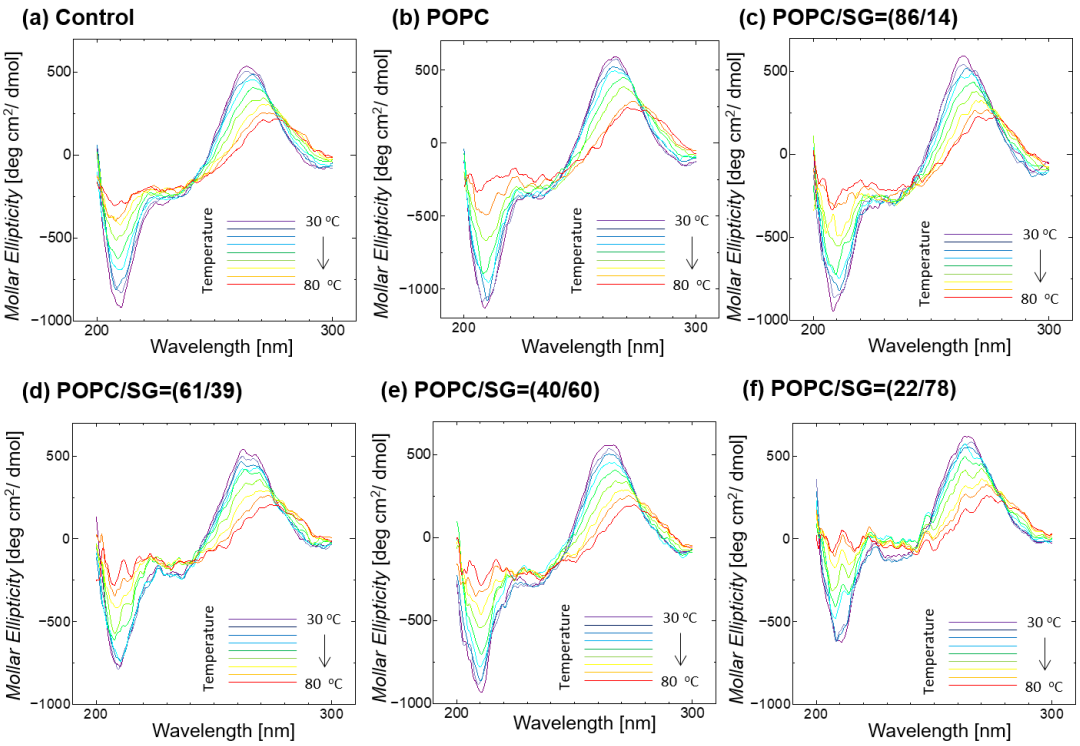

Figure 6-5 CD spectra of tRNA in the presence of POPC/SG vesicles. **(a)** Control (without vesicle), **(b)** POPC, **(c)** POPC/SG = (86/14), **(d)** POPC/SG = (61/39), **(e)** POPC/SG = (40/60), **(f)** POPC/SG = (22/78). Total tRNA and lipid concentration was 2 μM and 250 μM, respectively.

3.5. Evaluation of melting temperature (T_m) based on peak intensity

The melting temperature (T_m) of tRNA can be determined by analyzing the CD peak intensity (θ) (Bailly *et al.*, 1996; Berg *et al.*, 2002). Based on the two-state assumptions, the normalized ellipticities were calculated from the variation in CD peak intensities ($\Delta\theta$): $\Delta\theta = 0$ at 30°C, tRNA is intact; $\Delta\theta = 1$ at 80°C, tRNA is fully denatured; $\Delta\theta = 0.5$ at T_m, half of the tRNA conformation is denatured. A higher T_m value represents that the tRNA is more stable, while a lower T_m value represents the instability of tRNA conformation during the heating process. The $\Delta\theta$ values of tRNA in the presence of POPC/SG vesicles are summarized in **Figure 6-6**, together with the T_m values obtained from the fitting equations. The T_m value was slightly increased by the presence of POPC/SG = (61/39), while the T_m values decreased by POPC/SG = (22/78). This suggests that the destabilization of tRNA was induced by the interaction with the SG-enriched membrane. Although the effect of the vesicles on T_m was small, the observed difference was distinguishable. Considering that the SG molecules in the l_d phases did not influence

the stability of tRNA, the enrichment of SG molecules in the membrane surface may control the interaction and conformational change in RNA molecules. In addition, the previous study suggested that heterogeneous liposomes (l_d + l_o) interact with the nucleobase cytosine, while liposomes in the l_d phases interacted with the nucleobase guanine (Suga *et al*., 2011). It is thought that the exposed C and G (result of C-G cleavage) interact with the membrane surface in heterogeneous domains (including small l_o–like domain) and that in l_d, respectively.

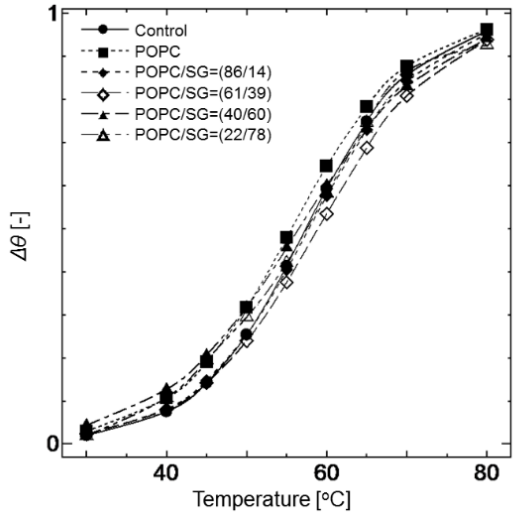

	T_m [°C]
Control	57.5±0.7
POPC	55.6±0.3
POPC/SG=(86/14)	57.8±0.4
POPC/SG=(61/39)	58.9±1.2
POPC/SG=(40/60)	56.5±1.3
POPC/SG=(22/78)	56.6±3.2

Figure 6-6 CD peak intensity of tRNA in the presence of POPC/SG vesicles. Peak intensities at 265 nm were normalized based on Eq. 6-7, and fitting curves were drawn based on Eq. 6-8. CD spectra of tRNA are shown in **Figure 6-5**. Total concentration of tRNA was 2 μM in the presence or absence of POPC/SG vesicles (total lipid concentration: 250 μM). The average T_m values (at least 3-time measurement) were estimated based on the fitting curve: $\Delta\theta$=0.5 at T_m. Control indicates the sample including tRNA only.

3.6. Evaluation of peak shift induced by POPC/SG vesicles during heating process

The peak shift in CD spectrum at 265 nm has been reported to be an indicator of intrinsic base pair formation, because the CD peaks at 265 and 273 nm are derived from A-U and C-G base pair stacking, respectively (Gregoire *et al*., 1997). A-U and C-G base pairs consist of two and three H-bonds, respectively; A-U base pairs are thus cleaved at lower temperatures than C-G pairs. Under heating in the control, a red shift in the CD peak at 265 nm and decreased peak intensity were observed. The peak shift

($\Delta\lambda$) was normalized based on Eq. 6-9, and the relationship between $\Delta\theta$ and $\Delta\lambda$ was investigated (**Figure 6-7 (a) – (e)**). In the control (without vesicles), the $\Delta\theta$ and $\Delta\lambda$ values were similar, suggesting that the C-G base pairs were gradually cleaved with increasing temperature. In the presence of POPC/SG vesicles, a delay in the red shift at 265 nm was observed. POPC/SG = (61/39) and POPC/SG = (40/60) showed significant delays at the T_m. In contrast to the peak shift at each T_m, the $\Delta\lambda$ values decreased in the presence of POPC/SG vesicles (**Figure 6-7 (f)**). This indicates that the A-U base pairs still formed at the T_m, despite the denaturation of half of the tRNA conformation. Such a temperature shift in $\Delta\lambda$ indicates the prospect of preferential cleaving of C-G base pairs below the T_m in the presence of POPC/SG vesicles. Thus, SG molecules can interact with the phosphate groups in tRNA and selectively cleave C-G base pairs during heat denaturation. Focusing on the base-pairs in tRNA (common in tRNA of *E. coli*), C-G rich double strands can be seen in the D-loop arm, anticodon arm, and T-loop arm. If the SG-rich domain attacked such moieties and induced denaturation, C-G selective cleavage can be achieved.

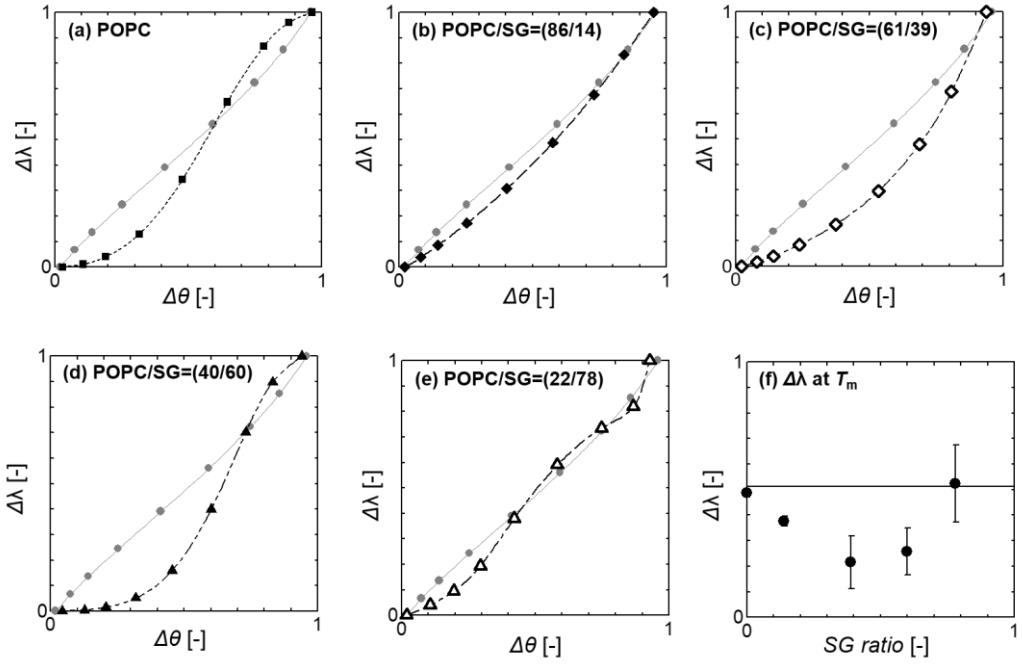

Figure 6-7 $\Delta\theta$ vs $\Delta\lambda$ plot for POPC/SG vesicles. $\Delta\theta$ and $\Delta\lambda$ values were estimated on the basis of Eq. 6-7 and 6-9, in the absence (ash circle) or presence of vesicles (lipid concentration: 250 μM): **(a)** with POPC (closed square), **(b)** with POPC/SG = (86/14) (closed diamond), **(c)** with POPC/SG = (61/39) (open diamond), **(d)** with POPC/SG = (40/60) (closed triangle), and **(e)** with POPC/SG = (22/78) (open triangle). **(f)** $\Delta\lambda$ values at T_m, estimated based on Eq. 6-10.

The results of the deconvolution of Laurdan spectra under the coexistence of nucleic acids also suggest the specific membrane surface property for the cytosine-selective interaction (**Figure 6-8**). POPC/SG (40/60), which revealed the specific delay for C-G melting, showed the hydrophilic property after the phase transition. Compared from the membrane property in DOPC bilayers and poly dC, which revealed the cytosine-selective interaction in Chapter 5, the deconvolution results of POPC/SG (40/60) were similar to that of DOPC bilayers. As the difference of the membrane property was not shown in POPC/SG (22/78) bilayer at 50 ℃, which is the system of non-interactive with the melting of C-G base pair, it is suggested that the hydrophilic membrane property is a key to provide the interaction with cytosine base. This indicates that the water molecules could interact with nucleobase cooperatively as a component of the lipid membrane.

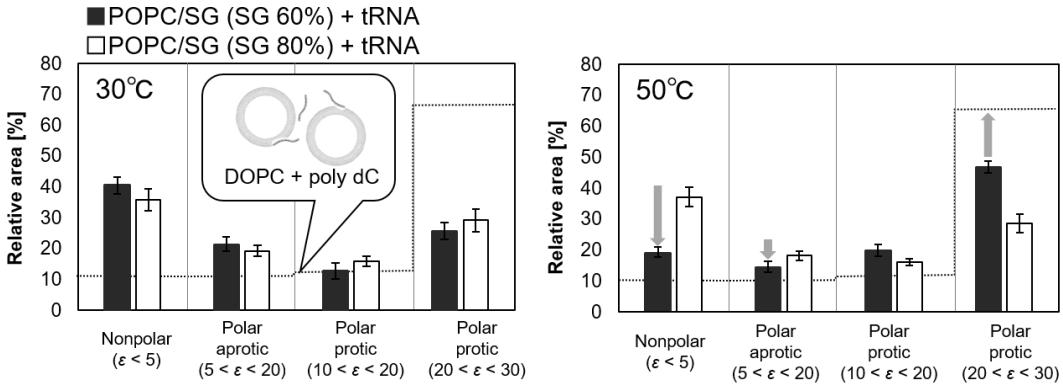

Figure 6-8 Deconvolution results of Laurdan emission spectra after the addition of tRNA at 30 ℃ and 50 ℃. POPC/SG (40/60) and POPC/SG (22/78) are filled black bar and open black bar, respectively. As example of the cytosine-selective interaction, the deconvolution results of Laurdan emission spectra in DOPC bilayers and poly dC system at 25 ℃ was illustrated with dot line.

4. Summary

Analyses of the pH-dependent fluorescence emission of TNS suggested that SG and MA molecules render the membrane surfaces cationic and anionic, respectively, which was also revealed by zeta potential measurements. The obtained results enabled the construction of a model of the headgroup orientation of zwitterionic POPC molecules controlled by modification with guanidinium derivatives. Based on DPH and Laurdan analysis, SG molecules induced the membrane to become rigid, then formed SG-enriched ordered phases, similar to the l_o phases formed by Ch-enrichment. The interaction between SG vesicles and tRNA was further studied by CD spectra analysis, focusing on the conformational changes in tRNA during heating. A red shift in the CD peak θ_{265} at the T_m was observed in the presence of POPC/SG vesicles, indicating the preferential melting of C-G base pairs. This tendency was the most significant by POPC/SG = (61/39) and POPC/SG = (40/60), suggesting that the enrichment of SG molecules in the membrane surface is important for inducing a unique conformational change in nucleic acid molecules. Guanidinium modification is superior to arrange (i) the cationic surface with a small net composition and (ii) the dehydrated membrane interphase by expelling water molecules out of the membrane, compared with the cationic surfactant. Thus, SG-modification can be used as a platform to induce strong affinity with nucleic acids, also performing the molecular selective interaction depending on the membrane phase states. Question arises regarding what type of forces would be dominant as the main driving force depending on the interaction types as classified with regard to the affinity, scale, configuration, and so on. Given that the example relating to the concentration of membrane-associating water molecules (**Figure 6-9**), the shift of water concentration ([water]) was drastic in "*strong interaction*". In "*weak interaction*", in spite of the negligible change of [water], other interactions could be working to generate the cooperativity and molecular selectivity. In order to focus on the parameters, such as polarizability or the number of possible H-bonding sites, further "*closeup*" to the local gradient of factors should be investigated.

Significant impacts of SG-modification on the interaction with biomacromolecules such as tRNA can be understood in the several phases based on the concepts explained in previous chapters (**Figure 6-10**). Before the phase transition, high affinity was performed

due to its cationic surface provided hydrophobic and ordered membrane property. This interaction was induced in the model of "*strong interaction*" with a drastic dehydration. The phase transition could be the trigger of the transition of interaction phase. Following the phase transition, the interaction phase will sequentially shift to the "*weak interaction*", the process wherein the cooperative interactions take place. Since the dehydration has already provoked, further interactions would be replaced into other types of noncovalent interactions such as hydrogen bonding, or hydrophobic interaction etc., generating the molecular selectivity. It was shown that fluidic DOPC membrane revealed selective interaction with nucleobase, especially cytosine, indicating that melted POPC/SG membrane may have a specific affinity with cytosine-guanine pair. This also suggests the molecular selectivity could be performed at the disordered membrane in a cooperative manner of "*weak interaction*".

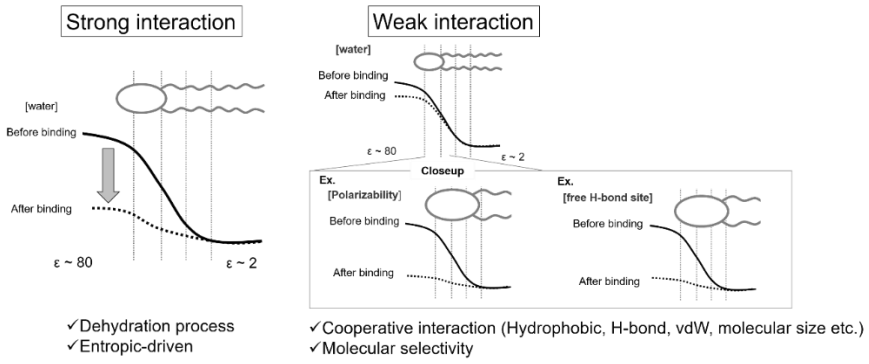

Figure 6-9 Conceptual diagram of the membrane-associating parameters.

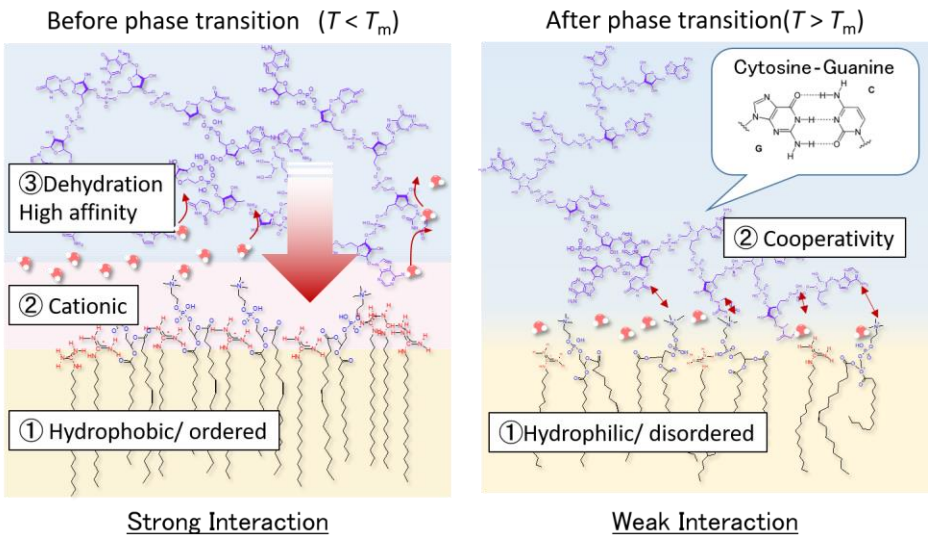

Figure 6-10 Classification of interactions between SG-modified membranes and tRNA.

Chapter 7

General Conclusion

Structures and functions of biomolecules are fascinating but complex. Fundamental comprehension of biological function and its structures are essential for the industrial application of the biomaterials. Molecular interaction at the lipid membrane surface was investigated in this study, especially from the aspects of the solvatochromic properties of the membrane, cooperativity of molecular interaction at the membrane surface, and configurational properties of membrane-constituting molecules, by employing the nucleic acids as the model biomacromolecules.

In Chapter 2, focusing on that the polarity around the membrane interface, a solvent model by using the fluorescent molecule Laurdan was established to monitor the local dielectric environment in the membrane. Based on the investigation of various lipids, it was clarified that the environment of fluorescent molecules could differ greatly depending on the fluorescence wavelengths as observed from anisotropy, excitation spectra and so on. From the results obtained by fluorescence analysis under solvent conditions, a method to decompose and evaluate the drastic change in the dielectric constant of the lipid membrane interface was finally established.

In Chapter 3, the time-resolved fluorescence spectrum of Laurdan was analyzed in order to evaluate the dynamic characteristics of water molecules hydrating to lipid molecules. From the evaluation of the dynamic characteristics of fluorescence lifetime in the fluorescence quenching model, the amounts of collisional lipid molecules were analyzed. Contribution of statically hydrated water was also assigned based on the solvent state assumptions as discussed in Chapter 2. By combining these dynamic and static contributions, the number of water molecules hydrated to a lipid molecule was calculated. The obtained values showed behavior corresponding to the membrane phase transition on temperatures and membrane phase separation in different composition, suggesting this calculation method could be able to evaluate the practical lipid membrane system.

In Chapter 4, a modification of vesicles with guanidinium derivatives was attempted aiming for the removal of the water molecules present in the hydrophilic region

of the membrane and for adjusting the membrane surface to be cationic. Guanidinium molecule with the saturated chain (SG) altered membrane properties hydrophobic and ordered. According to the estimation of the binding constants, this guanidinium-modified lipid membrane (POPC/SG) performed strong affinity to transfer nucleic acids (tRNA) which are the model biomacromolecules, suggesting the effective membrane design of the guanidinium modification.

In Chapter 5, the binding behaviors of nucleic acids on the lipid membrane were evaluated. In the cationic and hydrophobic lipid membranes such as POPC/SG, they are strongly bound with tRNA and their binding was revealed to influence the hydration property of the membrane. On the contrary, neutral lipid membranes and small biomolecules such as DOPC bilayer and oligonucleotides showed selective adsorption behavior without the significant change of the hydration. These results were discussed using the enthalpy-entropy compensation relationship and lead to a systematic understanding of the binding behavior between lipid membrane and biomolecules.

In Chapter 6, the influence of guanidinium modification on lipid membrane was evaluated. From the pH-dependent fluorescence of TNS and the ζ potential, it was indicated that the charge state of the membrane surface was determined by intermolecular interaction among lipid molecules, confirming the potential of SG modified membranes for the interaction with nucleic acids. The unique property of POPC/SG vesicles was also shown that it could induce the specific melting on nucleotide sequence of nucleic acid molecule with temperature during membrane phase transition. Interaction behavior during the membrane phase transition was discussed based on the gradient of water concentration with the classification of the binding types as "*strong interaction*" and "*weak interaction*". While the parameter which dominates the interaction as the driving force could be varied in relation to the other molecules that possess different interaction pair (both for biomacromolecules and for membrane composition), this schematic finding could contribute to obtain the whole image of the interaction platform and its design for control of the functional field of hydrophobic/hydrophilic interface at the lipid membrane.

Suggestions for Future Works

(1) Regulation of hydration layer

As shown in this study, it is conceivable that the adsorption phenomenon is promoted or inhibited by the presence of water molecules present at the lipid membrane. In order to take an advantage of the "*interface*" of the membrane, it is required to fully understand and control this hydration layer existing as a barrier. In this study, the hydrophobic membrane environments were obtained by modifying the guanidinium molecule at the hydrophilic/hydrophobic interface. It is expected that an electric double layer is formed by water molecules as counter ions on the strongly charged membrane surface. Hence, the hydration behavior from the inside of the membrane to the membrane surface should be considered. One possible approach for the promotion of adsorption of biomacromolecules is the addition of salt to induce the dehydration of hydrating water molecules at membrane surface. After the removal of the hydrating water molecules, further strong interaction could be induced by the guanidinium modified membranes due to its cationic and hydrophobic membrane properties. Guanidinium modified membrane could induce the affinity in the hydrophobic environment at the interface, different from the conventional cationic surfactant. Therefore, it can be regarded as a bio-inspired system with less net cationic modification and it provides the recognition platform through various noncovalent interactions, resulting in the strong affinity to the molecules. This "*bio-inspired* " platform could give the promising application for the drug carrier or the biosensor.

(2) Comprehension for the "lipid raft" formation

From the fluorescence analysis of Laurdan developed in this study, the distribution of water molecules in the multicomponent system was confirmed in accordance with the phase state of the membrane. Multiple distribution of water molecules were observed in the system composed of cholesterol (data not shown). This suggests the presence of the plural hydration states at the lipid membrane. The question arises how the distribution of

the hydration state present in one membrane influences the inter-lipid interaction and leads to the formation of local ordered domains. Evaluation of the laterally distributed hydration state will give important knowledge to the discussion of the raft formation that has been attracting many interests for years. Furthermore, there is a possibility of giving a new consideration to the question such as how the heterogeneity of hydration in the lipid membrane determines the state of adsorption with external molecules.

(3) Clarification of "driving force" at the lipid membrane

As shown in the example of "*strong binding*" and "*weak binding*", the differences of the dominant interaction forces were indicated depending on the interaction affinity, molecular size, and so on. The position wherein the drastic gradient of the environmental factor presents is defined as "*interface*", and the "*active*" gradient would generate the interaction forces. One can be expected that several factors, such as the gradient of the dielectric constant or the polarization moment, could induce the molecular interactions, and, especially when those interactions work simultaneously, whole interaction will be "*cooperative*" at the fluctuated self-assembly system. Evaluation of these factors separately could give the detailed view for the selectivity and cooperativity of intermolecular interactions.

Nomenclatures

$1/P$	= membrane fluidity	[-]
A	= absorbance of UV-Vis light	[a.u.]
D	= diffusion constant	[m^2/s]
FWHM	= the full width at half maximum	[nm]
G	= Gibbs free energy	[J]
G	= correction factor	[-]
GP_{340}	= general polarization calculated at exciting light at 340 nm	[-]
H	= enthalpy	[J]
I	= fluorescence intensity	[a.u.]
K_D	= dissociation constant	[M]
K_{SV}	= Stern–Volmer constant	[m^3/mol]
K_a	= binding constant	[M^{-1}]
M_{tot}	= macromolecule concentration	[mol/L]
OD_{400}	= turbidity at 400 nm	[-]
Q	= quantum yield	[-]
R	= packing density of lipid membrane	[-]
R^2	= correlation function	[-]
S	= entropy	[J]
V_0	= reaction cell of volume	[L]
X_{tot}	= total ligand concentration	[mol/L]
k_a	= quenching constant for static quenching	[M^{-1}]
k_q	= quenching rate coefficient	[m^3/mol]
k_r	= nonradiative constant	[m^3/(mol・s)]
pK_a	= acidity constant	[-]
r	= fluorescence anisotropy	[-]
$\Delta H°$	= molar heat of binding	[J]
Γ	= emission rate constant	[-]
ε	= relative dielectric constant	[-]
θ	= CD peak (molar ellipticity)	[deg cm^2/dmol]
λ	= peak position of the deconvolution curve	[nm]
λ_{em}	= emission wavelength	[nm]
λ_{ex}	= excitation wavelength	[nm]
ν	= stretching vibration	[cm^{-1}]
τ	= fluorescence lifetime	[s]

List of Abbreviations

5-DOXYL	2-(3-carboxypropyl)4,4-dimethyl-2-tridecyl-3-oxazolidinyloxy
CD	Circular dichroism
CTAB	Cetyltrimethylammonium bromide
Ch	Cholesterol
DDAB	Dilauryldimethylammonium bromide
DHPSM	D-*erythro*-N-palmitoyl-dihydrosphingomyelin
DLS	Dynamic light scattering
DLVO	Derjaguin-Landau-Verwey-Overbeek
DMPC	1,2-Dimyristoyl-*sn*-glycero-3-phosphocholine
DNA	Deoxyribonucleic acid
DOPC	1,2-Dioleoyl-*sn*-glycero-3-phosphocholine
DOPE	1,2-Dioleoyl-*sn*-glycero-3-phosphoethanolamine
DOTAP	1,2-Dioleoyl-3-trimethylammonium-propane
DPH	1,6-Diphenyl-1,3,5-hexatriene
DPPC	1,2-Dipalmitoyl-*sn*-glycero-3-phosphocholine
DPTAP	1,2-Dipalmitoyl -3-trimethylammonium-propane
FT-IR	Fourier transform-infrared
HPLC	High-performance liquid chromatography
ITC	Isothermal titration calorimetric
LUV	Large unilamellar vesicle
Laurdan	6-Lauroyl-2-dimethylamino naphthalene
MA	Myristoylarginine
MLV	Multilamellar vesicle
NMR	Nuclear magnetic resonance
POPC	1-Palmitoyl-2-oleoyl-*sn*-glycero-3-phosphocholine
PSM	D-*erythro*-N-palmitoyl-sphingosylphosphorylcholine
SG	Stearylguanidinium
TEMPO	2,2,6,6-Tetramethylpiperidine 1-oxyl free radical
TNS	6-(*p*-toluidino)naphthalene-2-sulfonate
TRES	Time-resolved emission spectra
T_m	Phase transition temperature
UV-vis	Ultraviolet-visible
cmc	Critical micelle concentration
l_d	Liquid disordered
l_o	Liquid ordered
s_o	Solid ordered
tRNA	Transfer ribonucleic acid

References

Abrams, F. S.; London, E. Extension of the Parallax Analysis of Membrane Penetration Depth to the Polar Region of Model Membranes: Use of Fluorescence Quenching by a Spin-Label Attached to the Phospholipid Polar Headgroup. *Biochemistry* **1993**, *32 (40)*, 10826–10831.

Aguiar, J.; Carpena, P.; Moline-Bolivar, J. A.; Carnero Ruiz, C. On the Determination of the Critical Micelle Concentration by the Pyrene 1:3 Ratio Method. *J. Col. Int. Sci.* **2003**, *258*, 116–122.

Ahmed, S. N.; Brown, D. A.; London, E. On the Origin of Sphingolipid/Cholesterol-Rich Detergent-Insoluble Formation of a Detergent-Insoluble, Liquid-Ordered Lipid Phase in Model Membrnanes. *Biochemistry* **1997**, *36*, 10944–10953.

Aissaoui, A.; Oudrhiri, N.; Petit, L.; Hauchecorne, M.; Kan, E.; Sainlos, M. Progress in Gene Delivery by Cationic Lipids: Guanidinium-Cholesterol-Based Systems as an Example. *Curr. Drug Targets.* **2002**, *3*, 1–16.

Alarcón, L. M.; de los Angeles Frías, M.; Morini, M. A.; Belén Sierra, M.; Appignanesi, G. A.; Anibal Disalvo, E. Water Populations in Restricted Environments of Lipid Membrane Interphases. *Eur. Phys. J. E* **2016**, *39 (10)*.

Alberts, B.; Johnson, A.; Lewis, J.; Morgan, D.; Raff, M.; Roberts, K.; Walter, P. *Molecular Biology of the Cell, 6th ed.*; Garland Science: New York and Abingdon, UK, **2014**; *16*.

Ariga, K.; Kunitake, T. Molecular Recognition at Air−Water and Related Interfaces: Complementary Hydrogen Bonding and Multisite Interaction. *Acc. Chem. Res.* **1998**, 31 (6), 371–378.

Ariga, K.; Nakanishi, T.; Hill, J. P. A Paradigm Shift in the Field of Molecular Recognition at the Air-Water Interface: From Static to Dynamic. *Soft Matter* **2006**, *2*, 465–477.

Bacalum, M.; Zorilă, B.; Radu, M. Fluorescence Spectra Decomposition by Asymmetric Functions: Laurdan Spectrum Revisited. *Anal. Biochem.* **2013**, *440 (2)*, 123–129.

Bagatolli, L. A.; Gratton, E. A Correlation between Lipid Domain Shape and Binary Phospholipid Mixture Composition in Free Standing Bilayers: A Two-Photon Fluorescence Microscopy Study. *Biophys. J.* **2000**, *79 (1)*, 434–447.

Bagatolli, L. A.; Gratton, E. Two Photon Fluorescence Microscopy of Coexisting Lipid Domains in Giant Unilamellar Vesicles of Binary Phospholipid Mixtures. *Biophys. J.* **2000**, *78 (1)*, 290–305.

Bagatolli, L. A.; Parasassi, T.; Fidelio, G. D.; Gratton, E. A Model for the Interaction of 6-Lauroyl-2-(n,n-dimethylamino)naphthalene with Lipid Environments: Implications for Spectral Properties. *Photochem. Photobiol.* **1999**, *70 (4)*, 557–564.

Bailly, C.; Colson, P.; Houssier, C.; Hamy, F. The Binding Mode of Drugs to the TAR RNA of HIV-1 Studied by Electric Linear Dichroism. *Nucleic Acids Res.* **1996**, *24*, 1460–1464.

Barenholz, Y. *Sphingomyelin and Cholesterol: From Membrane Biophysics and Rafts to Potential Medical Applications. In Membrane Dynamics and Domains; Subcellular Biochemistry*; Springer, Boston, MA, **2004**.

Barreleiro, P. C.; Olofsson, G.; Alexandridis, P. Interaction of DNA with Cationic Vesicles: A Calorimetric Study. *J. Phys. Chem. B* **2000**, *104*, 7795–7802.

Batenjany, M. M.; Wang, Z. Q.; Huang, C. H.; Levin, I. W. Packing Characteristics of Mixed Chain Phospholipid Derivatives: Raman Spectroscopic and Differential Scanning Calorimetric Studies of 1-Stearoyl-2-capryl-*sn*-glycero-3-phosphocholine(C(18):C(10) PC) and 1-Stearoyl-2-capryl-*sn*-glycero-3-phospho-*N*-trimethylpropanolamine (C(18):C(10) TMPC). *Biochim. Biophys. Acta* **1994**, *1192*, 205–214.

Berg, J. M.; Tymoczko, J. L.; Stryer, L. *Biochemistry*, Chapter 5, 5th ed.; W. H. Freeman and Company: New York, **2002**.

Binder, H. The Molecular Architecture of Lipid Membranes—New Insights from Hydration-Tuning Infrared Linear Dichroism Spectroscopy. *Appl. Spectrosc. Rev.* **2003**, *38 (1)*, 15–69.

Bui, H. T.; Umakoshi, H.; Suga, K.; Tanabe, T.; Ngo, K. X.; Shimanouchi, T.; Kuboi, R. Cationic DOTAP Liposome Can Interfere mRNA Translation of GFP in an E. coli Cell-free Translation System. *Biochem. Eng. J.* **2010**, *52*, 38.

Büldt, G.; Gally, H. U.; Seelig, J. Neutron Diffraction Studdies on Phosphatidylcholine Model Membranes I. Head Group Conformation. *J. Mol. Biol.* **1979**, *134*, 673–691.

Carmona, P.; Rodriguez-Casado, A.; Molina, M. Conformational Structure and Binding Mode of Glyceraldehyde-3-phosphate Dehydrogenase to tRNA Studied by Raman and CD Spectroscopy. *Biochim. Biophys. Acta* **1999**, *1432*, 222–233.

Casem, M. L. *Membranes and Membrane Transport. In Case Studies in Cell Biology;* Casem, M. L., Ed.; Problem Sets in Biological and Biomedical Sciences; Academic Press: Boston, **2016**.

Celli, A.; Gratton, E. Dynamics of Lipid Domain Formation: Fluctuation Analysis. *Biochem. Biophys. Acta* **2010**, *1798 (7)*, 1368–1376.

Cevc, G. How Membrane Chain Melting Properties Are Regulated by the Polar Surface of the Lipid Bilayer. *Biochemistry* **1987**, *26 (20)*, 6305–6310.

Cevc, G. Membrane Electrostatics. *Biochim. Biophys. Acta* **1990**, *1031 (3)*, 311–382.

Chattopadhyay, A.; London, E. Parallax Method for Direct Measurement of Membrane Penetration Depth Utilizing Fluorescence Quenching by Spin-Labeled Phospholipids. *Biochemistry* **1987**, *26 (1)*, 39–45.

Chen, H.; Zheng, Y.; Jiang, J.-H.; Wu, H.L.; Shen, G.L.; Yu, R.Q. An Ultrasensitive Chemiluminescence Biosensor for Cholera Toxin Based on Ganglioside-Functionalized Supported Lipid Membrane and Liposome. *Biosens. Bioelectron.* **2008**, *24*, 684–689.

Chesnoy, S.; Huang, L. Structure and Function of Lipid-DNA Complexes for Gene Delivery. *Annu. Rev. Biomol. Struc.* **2000**, *29*, 27–47.

Chiu, S. W.; Vasudevan, S.; Jakobsson, E.; Mashl, R. J.; Scott, H. L. Structure of Sphingomyelin Bilayers: A Simulation Study. *Biophys. J.* **2003**, *85 (6)*, 3624–3636.

Clark, C. L.; Cecil, P. K.; Shingh, D.; Gray, D. M. CD, Absorption and Thermodynamic Analysis of Repeating Dinucleotide DNA, RNA and Hybrid Duplexes $[d/r(AC)]_{12}\cdot[d/r(GT/U)]_{12}$ and the Influence of Phosphorothioate Substitution. *Nucleic Acids Res.* **1997**, *25*, 4098–4105.

Costard, R.; Heisler, I. A.; Elsaesser, T. Structural Dynamics of Hydrated Phospholipid Surfaces Probed by Ultrafast 2D Spectroscopy of Phosphate Vibrations. *J. Phys. Chem. Lett.* **2014**, *5 (3)*, 506–511.

Coster, H. G. L.; Chilcott, T. C.; Coste, A. C. F. Impedance Spectroscopy of Interfaces, Membranes and Ultrastructures. *Bioelectrochem Bioenerg.* **1996**, *40*, 79–98.

Damodaran, S. Water Activity at Interfaces and Its Role in Regulation of Interfacial Enzymes: A Hypothesis. *Colloids Surf. B* **1998**, *11*, 231–237.

Davletov, B. A.; Südhof, T. C. A Single C2 Domain from Synaptotagmin I is Sufficient for High Affinity Ca^{2+}/Phospholipid Binding. *J. Biol. Chem.* **1993**, *268*, 26386-26390.

De Almeida, R. F. M.; Fedorov, A.; Prieto, M. Sphyngomyelin/ Phosphatidylcholine /Cholesterol Phase Diagram: Boundaries and Composition of Lipid Rafts. *Biophys. J.* **2003**, *85*, 2406–2416.

De Lange, M. J. L.; Bonn, M.; Müller, M. Direct Measurement of Phase Coexistence in DC/Cholesterol Vesicles Using Raman Spectroscopy. *Chem. Phys. Lipids* **2007**, *146*, 76–84.

De Vequi-Suplicy, C. C.; Benatti, C. R.; Lamy, M. T. Laurdan in Fluid Bilayers: Position and Structural Sensitivity. *J. Fluoresc.* **2006**, *16 (3)*, 431–439.

De Vequi-Suplicy, C. C.; Coutinho, K.; Lamy, M. T. Electric Dipole Moments of the Fluorescent Probes Prodan and Laurdan: Experimental and Theoretical Evaluations. *Biophys. Rev.* **2014**, *6 (1)*, 63–74.

De Vequi-Suplicy, C. C.; Coutinho, K.; Lamy, M. T. New Insights on the Fluorescent Emission Spectra of Prodan and Laurdan. *J. Fluores.* **2015**, *25 (3)*, 621–629.

De Vequi-Suplicy, C. C.; Lamy, M. T.; Marquezin, C. A. The New Fluorescent Membrane Probe Ahba: A Comparative Study with the Largely Used Laurdan. *J. Fluoresc.* **2013**, *23 (3)*, 479–486.

Disalvo, E. A.; Frias, M. A. Water State and Carbonyl Distribution Populations in Confined Regions of Lipid Bilayers Observed by FTIR Spectroscopy. *Langmuir* **2013**, *29 (23)*, 6969–6974.

Disalvo, E. A.; Lairion, F.; Martini, F.; Tymczyszyn, E.; Frías, M.; Almaleck, H.; Gordillo, G. J. Structural and Functional Properties of Hydration and Confined Water in Membrane Interfaces. *Biochim. Biophys. Acta* **2008**, *1778 (12)*, 2655–2670.

Disalvo, E. A.; Martini, M. F.; Bouchet, A. M.; Hollmann, A.; Frías, M. A. Structural and Thermodynamic Properties of Water–Membrane Interphases: Significance for Peptide/Membrane Interactions. *Adv. Col. Int. Sci.* **2014**, *211*, 17–33.

Epand, R. M. Cholesterol in Bilayers of Sphingomyelin or Dihydrosphingomyelin at Concentrations Found in Ocular Lens Membranes. *Biophys. J.* **2003**, *84 (5)*, 3102–3110.

Felgner, P. L.; Gadek, T. R.; Holm, M.; Roman, R.; Chan, H. W.; Wenz, M.; Northrop, J. P.; Ringold, G. M.; Danielsen, M. Lipofection: A Highly Efficient, Lipid-Mediated DNA Transfection Procedure. *Proc. Natl. Acad. Sci. USA.* **1987**, *84*, 7413–7417.

Ferguson-Yankey, S. R.; Borchman, D.; Taylor, K. G.; DuPré, D. B.; Yappert, M. C. Conformational Studies of Sphingolipids by NMR Spectroscopy. I. Dihydrosphingomyelin. *Biomembranes* **2000**, *1467 (2)*, 307–325.

Fox, C. B.; Uibel, R. H.; Harris, J. M. Detecting Phase Transitions in Phosphatidylcholine Vesicles by Raman Microscopy and Selfmodeling Curve Resolution. *J. Phys. Chem. B* **2007**, *111*, 11428–11436.

Fumagalli, L.; Esfandiar, A.; Fabregas, R.; Hu, S.; Ares, P.; Janardanan, A.; Yang, Q.;Radha, B.: Taniguchi, T.; Watanabe, K.; Gomila, G.; Novoselov, K. S.; Geim, A. K. Anomalously Low Dielectric Constant of Confined Water. *Science* **2018**, *360 (6395)*, 1339-1342.

Gaede, H. C.; Gawrisch, K. Lateral Diffusion Rates of Lipid, Water, and a Hydrophobic Drug in a Multilamellar Liposome. *Biophys. J.* **2003**, *85 (3)*, 1734–1740.

Gally, H. U.; Niederberger, W.; Seelig, J. Conformation and Motion of the Choline Head Group in Bilayers of Dipalmitoyl-3-*sn*-phosphatidylcholine. *Biochemistry* **1975**, *14 (16)*, 3647–3652.

Gao, X.; Huang, L. A Novel Cationic Liposome Reagent for Efficient Transfection of Mammalian Cells. *Biochem. Biophys. Res. Commun.* **1991**, *179*, 280–285.

Gerke, V.; Moss, S. E. Annexins and Membrane Dynamics. *Biochim. Biophys. Acta* **1997**, *1357 (2)*, 129-154.

Giatrellis, S.; Nounesis, G. Nucleic Acid-Lipid Membrane Interactions Studied by DSC. *J. Pharma. Bioall. Sci.* **2011**, *3 (1)*, 70.

Gramse, G.; Dols-Perez, A.; Edwards, M. A.; Fumagalli, L.; Gomila, G. Nanoscale Measurement of the Dielectric Constant of Supported Lipid Bilayers in Aqueous Solutions with Electrostatic Force Microscopy. *Biophys. J.* **2013**, *104 (6)*, 1257–1262.

Graça, J.S.; de Oliveira, R.F.; de Moraes, M.L.; Ferreira, M. Amperometric Glucose Biosensor based on Layer-by-Layer Flms of Microperoxidase-11 and Liposome-encapsulated Glucose Oxidase. *Bioelectrochemistry* **2014**, *96*, 37–42

Gregoire, C. J.; Gautheret, D.; Loret, E. P. No $tRNA_3^{Lys}$ Unwinding in a Complex with HIV NCp7. *J. Biol. Chem.* **1997**, *272*, 25143–25148.

Griffin, R. G.; Powers, L.; Pershan, P. S. Head-Group Conformation in Phospholipids: A ^{31}P Nuclear Magnetic Resonance Study of Oriented Monodomain Dipalmitoylphosphatidylcholine Bilayers. *Biochemistry* **1978**, *17 (14)*, 2718–2722.

Gruen, D. W. R.; Marčelja, S. Spatially Varying Polarization in Water. a Model for the Electric Double Layer and the Hydration Force. *J. Chem. Soc., Faraday Trans.* **1983**, *79(2)*, 225-242.

Guzman, R. N.; Wu, Z. R.; Stalling, C. C.; Pappalardo, L.; Borer, P. N.; Summers, M. F. Structure of the HIV-1 Nucleocapsid Protein Bound to the SL3Ψ-RNA Recognition Element. *Science* **1998**, *279*, 384–388.

Harris, F. M.; Best, K. B.; Bell, J. D. Use of Laurdan Fluorescence Intensity and Polarization to Distinguish between Changes in Membrane Fluidity and Phospholipid Order. *Biochim. Biophys. Acta* **2002**, *1565 (1)*, 123–128.

Haugland, R. P. *Handbook of Fluorescent Probes and Research Chemicals, 6th ed.*; Molecular Probes Inc.: Eugene, OR, **1996**.

Hayashi, K.; Shimanouchi, T.; Kato, K.; Miyazaki, T.; Nakamura, A.; Umakoshi, H. Span 80 Vesicles Have a More Fluid, Flexible and "Wet" Surface than Phospholipid Liposomes. *Colloids Surf. B* **2011**, *87*, 28–35.

Henderson, L. J. Concerning the Relationship between the Strength of Acids and Their Capacity to Preserve Neutrality. *Am. J. Physiol.* **1908**, *21*, 173–179.

Hille, B. *Ion Channels of Excitable Membranes (3rd ed.).;* Mass: Sinauer Associates Inc.: Sunderland, **1984.**

Hirsch-Lerner, D.; Barenholz, Y. Hydration of Lipoplexes Commonly Used in Gene Delivery: Follow-up by Laurdan Fluorescence Changes and Quantification by Differential Scanning Calorimetry. *Biochim. Biophys. Acta* **1999**, *1461*, 47–57.

Hope, M. J.; Bally, M. B.; Webb, G.; Cullis, P. R. Production of Large Unilamellar Vesicles by a Rapid Extrusion Procedure. Characterization of Size Distribution, Trapped Volume and Ability to Maintain a Membrane Potential. *Biochim. Biophys. Acta* **1985**, *812 (1)*, 55–65.

Ikeura, Y.; Kurihara, K.; Kunitake, T. Molecular Recognition at the Air-Water Interface. Specific Binding of Nitrogen Aromatics and Amino Acids by Monolayers of Long-Chain Derivatives of Kemp's Acid. *J. Am. Chem. Soc.* **1991**, *113 (19)*, 7342–7350.

Ishigami, T.; Suga, K.; Umakoshi, H. Chiral Recognition of L-Amino Acids on Liposomes Prepared with L-Phospholipid. *ACS Appl. Mater. Interfaces* **2015**, *7 (38)*, 21065–21072.

Israelachvili, J. N. *Intermolecular and Surface Forces, 3rd ed*.; Academic Press, **1985**.

Israelachvili, J. N.; Adams, G. E. Measurement of Forces Between Two Mica Surfaces in Aqueous Electrolyte Solutions in the Range 0–100 Nm. *J. Chem. Soc. Faraday Transacions.* **1978**, *74*, 975.

Israelachvili, J. N.; Pashley, R. M. Molecular Layering of Water at Surfaces and Origin of Repulsive Hydration Forces. *Nature* **1983**, *306 (5940)*, 249-250.

Iwasaki, F.; Luginbühl, S.; Suga, K.; Walde, P.; Umakoshi, H. Fluorescent Probe Study of AOT Vesicle Membranes and Their Alteration upon Addition of Aniline or the Aniline Dimer P-Aminodiphenylamine (PADPA). *Langmuir* **2017**, *33 (8)*, 1984–1994.

Janas, T.; Janas, T.; Yarus, M. Specific RNA Binding to Ordered Phospholipid Bilayers. *Nucleic Acids Res* **2006**, *34 (7)*, 2128–2136.

Janas, T.; Widmann, J. J.; Knight, R.; Yarus, M. Simple, Recurring RNA Binding Sites for L-Arginine. *RNA* **2010**, *16*, 806–816.

Jay, A. G.; Hamilton, J. A. Disorder Amidst Membrane Order: Standardizing Laurdan Generalized Polarization and Membrane Fluidity Terms. *J. Fluoresc.* **2017**, *27 (1)*, 243–249.

Jayaraman, M.; Ansell, S. M.; Mui, B. L.; Tam, Y. K.; Chen, J.; Du, X.; Buler, D.; Eltepu, L.; Matsuda, S.; Narayanannair, J. K. Maximizing the Potency of siRNA Lipid Nanoparticles for Hepatic Gene Silencing in Vivo. *Angew. Chem. Int. Ed.* **2012**, *51*, 8529–8533.

Jin, Z.-X.; Huang, C.-R.; Dong, L.; Goda, S.; Kawanami, T.; Sawaki, T.; Sakai, T.; Tong, X.-P.; Masaki, Y.; Fukushima, T.; et al. Impaired TCR Signaling through Dysfunction of Lipid Rafts in Sphingomyelin Synthase 1 (*SMS1*)-Knockdown T Cells. *Int Immunol.* **2008**, 20 (11), 1427–1437.

Jurkiewicz, P.; Olżyńska, A.; Langner, M.; Hof, M. Headgroup Hydration and Mobility of DOTAP/DOPC Bilayers: A Fluorescence Solvent Relaxation Study. *Langmuir* **2006**, *22 (21)*, 8741–8749.

Józefowicz, M.; Kozyra, K. A.; Heldt, J. R.; Heldt, J. Effect of Hydrogen Bonding on the Intramolecular Charge Transfer Fluorescence of 6-Dodecanoyl-2-dimethyl aminonaphtalene. *Chem. Phys.* **2005**, *320 (1)*, 45–53.

Kenis, H.; van Genderen, H.; Bennaghmouch, A.; Rinia, H. A.; Frederik, P.; Narula, J.; Hofstra, L.; Reutelingsperger, C. P. Cell Surface-expressed Phosphatidylserine and Annexin A5 Open a Novel Portal of Cell Entry. *J. Biol. Chem.* **2004**, 52623-62629.

Kinoshita, M.; Matsumori, N.; Murata, M. Coexistence of Two Liquid Crystalline Phases in Dihydrosphingomyelin and Dioleoylphosphatidylcholine Binary Mixtures. *Biochim. Biophys. Acta* **2014**, *1838 (5)*, 1372–1381.

Kinoshita, M.; Matsumori, N.; Murata, M. Coexistence of Two Liquid Crystalline Phases in Dihydrosphingomyelin and Dioleoylphosphatidylcholine Binary Mixtures. *Biochim. Biophys. Acta* **2014**, *1838 (5)*, 1372–1381.

Klasczyk, B.; Knecht, V.; Lipowsky, R.; Dimova, R. Interactions of Alkali Metal Chlorides with Phosphatidylcholine Vesicles. *Langmuir* **2010**, *26*, 18951−18958.

Koch, D.; Spiwoks-Becker, I.; Sabanov, V.; Sinning, A.; Dugladze, T.; Stellmacher, A.; Ahuja, R.; Grimm, J.; Schüler, S.; Müller, A.; Angenstein, F.; Ahmed, T.; Diesler, A.; Moser, M.; Tom Dieck, S.; Spessert, R.; Boeckers, T. M.; , Fässler, R.; Hübner, C.A.; Balschun, D.; Gloveli, T.; Kessels, M. M.; Qualmann, B. Proper Synaptic Vesicle Formation and Neuronal Network Activity Critically Rely on Syndapin I. *EMBO J.*, **2011**, *30*, 4955-4969.

Koiv, A.; Mustonen, P.; Kinnunen, P. K. Differential Scanning Calorimetry Study on the Binding of Nucleic Acids to Dimyristoylphosphatidylcholine-sphingosine Liposomes. *Chem Phys Lipids.* **1994**, *70*, 1–10.

Kuikka, M.; Ramstedt, B.; Ohvo-Rekila, H.; Tuuf, J.; Slotte, J. P. Membrane Properties of D-*erythro*-*N*-acyl Sphingomyelins and Their Corresponding Dihydro Species. *Biophys. J.* **2001**, *80*, 2327–2337.

Kunitake, T. Synthetic Bilayer Membranes: Molecular Design, Self-Organization, and Application. *Angew. Chem. Int. Ed. Engl.* **1992**, *31 (6)*, 709–726.

Kurihara, K.; Ohto, K.; Honda, Y.; Kunitake, T. Efficient, Complementary Binding of Nucleic Acid Bases to Diaminotriazine-Functionalized Monolayers on Water. *J. Am. Chem. Soc.* **1991**, *113 (13)*, 5077–5079.

Laage, D.; Elsaesser, T.; Hynes, J. T. Water Dynamics in the Hydration Shells of Biomolecules. *Chem Rev* **2017**, *117 (16)*, 10694–10725.

Lairion, F.; Disalvo, E. A. Effect of Dipole Potential Variations on the Surface Charge Potential of Lipid Membranes. *J. Phys. Chem. B* **2009**, *113 (6)*, 1607–1614.

Lajoie, P.; Nabi, I. R. *Lipid Rafts, Caveolae, and Their Endocytosis. In International Review of Cell and Molecular Biology*; Elsevier, **2010**.

Lakowicz, J. R. *Principles of Fluorescence Spectroscopy; Principles of Fluorescence Spectroscopy*; Kluvert Academic/Plenum Publishers: New York, **1999**.

Lakowicz, J. R.; Balter, A. Analysisofexcited-State Processes by Phase-Modulation Fluorescence Spectroscopy. *Biophys. Chem.* **1982**, *16 (2)*, 117–132.

Lakowicz, J. R.; Balter, A. Differential-Wavelength Deconvolution of Time-Resolved Fluorescence Intensities - a New Method for the Analysis of Excited-State Processes. *Biophys. Chem.* **1982**, *16 (3)*, 223–240.

Lakowicz, J. R.; Cherek, H.; Laczko, G.; Gratton, E. Time-Resolved Fluorescence Emission Spectra of Labeled Phospholipid Vesicles, as Observed Using Multi-Frequency Phase-Modulation Fluorometry. *Biochim. Biophys. Acta* **1984**, *777 (2)*, 183–193.

Leckband, D. E.; Helm, C. A.; Israelachvili, J. Role of Calcium in the Adhesion and Fusion of Bilayers. *Biochemistry* **1993**, *32 (4)*, 1127–1140.

Lehn, J.-M. Perspectives in Supramolecular Chemistry—From Molecular Recognition towards Molecular Information Processing and Self-Organization. *Angew. Chem. Int. Ed.* **1990**, *29 (11)*, 1304–1319.

Lentz, B. R.; Barenholz, Y.; Thompson, T. E. Fluorescence Depolarization Studies of Phase Transitions and Fluidity in Phospholipid Bilayers. 1. Single Component Phosphatidylcholine Liposomes. *Biochemistry* **1976**, *15 (20)*, 4521–4528.

Leventis, R.; Silvius, J. R. Interactions of Mammalian Cells with Lipid Dispersions Containing Novel Metabolizable Cationic Amphiphiles. *Biochim. Biophys. Acta* **1990**, *1023*, 124–132.

Levin, I. W.; Thompson, T. E.; Barenholz, Y.; Huang, C. Levin, I. W.; Thompson, T. E.; Barenholz, Y.; Huang, C. Two Types of Hydrocarbon Chain Interdigitation in Sphingomyelin Bilayers. *Biochemistry* **1985**, *24*, 6282–6286.

Li, C.; Ma, J.; Zhao, L.; Zhang, Y.; Yu, Y.; Shu, X.; Li, J.; Jia, X. Molecular Selective Binding of Basic Amino Acids by a Water-Soluble pillar[5]arene. *Chem. Comm.* **2013**, *49*,1924.

Lobo, B. A.; Davis, A.; Koe, G.; Smith, J. G.; Middaugh, C. R. Isothermal Titration Calorimetric Analysis of the Interaction between Cationic Lipids and Plasmid DNA. *Arch. Biochem. Biophys.* **2001**, *386 (1)*, 95–105.

Luckey, M. *Membrane Structural Biology with Biochemical and Biophysical Foundations*; CambridgeUniversity Press: Cambridge, **2012**.

Lumry, R.; Rajender, S. Enthalpy–Entropy Compensation Phenomena in Water Solutions of Proteins and Small Molecules: A Ubiquitous Properly of Water. *Biopolymers* **1970**, *9 (10)*, 1125–1227.

Lúcio, A. D.; De Vequi-Suplicy, C. C.; Fernandez, R. M.; Lamy, M. T. Laurdan Spectrum Decomposition as a Tool for the Analysis of Surface Bilayer Structure and Polarity: A Study with DMPG, Peptides and Cholesterol. *J. Fluoresc.* **2010**, *20 (2)*, 473–482.

Ma, C. D.; Wang, C.; Acevedo-Vélez, C.; Gellman, S. H.; Abbott, N. L. Modulation of Hydrophobic Interactions by Proximally Immobilized Ions. *Nature* **2015**, *517*, 347–350.

MacDonald, R. C.; MacDonald, R. I.; Menco, B. P. M.; Takeshita, K.; Subbarao, N. K.; Hu, L. Small-Volume Extrusion Apparatus for Preparation of Large, Unilamellar Vesicles. *Biochim. Biophys. Acta* **1991**, *1061*, 297–303.

Makino, K.; Yamada, T.; Kimura, M.; Oka, T.; Ohshima, H.; Kondo, T. Temperature- and Ionic Strength-Induced Conformational Changes in the Lipid Head Group Region of Liposomes as Suggested by Zeta Potential Data. *Biophysical Chemistry* **1991**, *41 (2)*, 175–183.

Malacrida, L.; Astrada, S.; Briva, A.; Bollati-Fogolín, M.; Gratton, E.; Bagatolli, L. A. Spectral Phasor Analysis of LAURDAN Fluorescence in Live A549 Lung Cells to Study the Hydration and Time Evolution of Intracellular Lamellar Body-like Structures. *Biochim. Biophys. Acta* **2016**, *1858 (11)*, 2625–2635.

Mantsch, H. H.; McElhaney, R. N. Phospholipid Phase Transitions in Model and Biological Membranes as Studied by Infrared Spectroscopy. *Chem. Phys. Lipids* **1991**, *57*, 213–226.

Marsh, D. Molecular Volumes of Phospholipids and Glycolipids in Membranes. *Chem. Phys. Lipids* **2010**, *163 (7)*, 667–677.

Martini, M. F.; Disalvo, E. A. Superficially Active Water in Lipid Membranes and Its Influence on the Interaction of an Aqueous Soluble Protease. *Biochim. Biophys. Acta* **2007**, *1768 (10)*, 2541–2548.

Marty, R.; N'soukpoé-Kossi, C. N.; Charbonneau, D. M.; Kreplak, L.; Tajmir-Riahi, H.-A. Structural Characterization of Cationic Lipid–tRNA Complexes. *Nucleic Acids Res* **2009**, *37 (15)*, 5197–5207.

Marčelja, S.; Radic, N. Repulsion of Interfaces Due to Boundary Water. *Chem. Phys. Lett.* **1976**, *42*, 129-130.

Mason, P. E.; Neilson, G. W.; Enderby, J. E.; Saboungi, M. L.; Dempsey, L. E.; MacKerell Jr, A. D.; Brady, J. W. The Structure of Aqueous Guanidinium Chloride Solutions. *J. Am. Chem. Soc*. **2004**, *22*, 11462–11470.

Massey, J. B. Interaction of Ceramides with Phosphatidylcholine, Sphingomyelin and Sphingomyelin/Cholesterol Bilayers. *Biochim. Biophys. Acta* **2001**, *1510 (1)*, 167–184.

Mayer, B. J.; Ren, R.; Clark, K. L.; Baltimore, D. A Putative Modular Domain Present in Diverse Signaling Proteins. *Cell* **1993**, *73*, 629-630.

McManus, J. J.; Rädler, J. O.; Dawson, K. A. Does Calcium Turn a Zwitterionic Lipid Cationic? *J. Phys. Chem. B* **2003**, *107 (36)*, 9869–9875.

Meierhenrich, U. J.; Filippi, J.-J.; Meinert, C.; Vierling, P.; Dworkin, J. P. On the Origin of Primitive Cells: From Nutrient Intake to Elongation of Encapsulated Nucleotides. *Angew. Chem. Int. Ed.* **2010**, *49 (22)*, 3738–3750.

Mohana-Borges, R.; Lima Silva, J.; de Prat-Gay, G. Protein Folding in the Absence of Chemical Denaturants: Reversible Pressure Denaturation of the Noncovalent Complex Formed by the Association of Two Protein Fragments. *J. Biol. Chem.* **1999**, *274 (12)*, 7732–7740.

Mondal, J. A.; Nihonyanagi, S.; Yamaguchi, S.; Tahara, T. Three Distinct Water Structures at a Zwitterionic Lipid/Water Interface Revealed by Heterodyne-Detected Vibrational Sum Frequency Generation. *J. Am. Chem. Soc.* **2012**, *134 (18)*, 7842–7850.

Morita, S.; Shimanouchi, T.; Sasaki, M.; Umakoshi, H.; Kuboi, R. Detection of a Heat Stress-Mediated Interaction between Protein and Phospholipid Membrane Using Dielectric Measurement. *J. Biosci. Bioeng.* **2003**, *95 (3)*, 252–256.

Mouritsen, O. G. The Liquid-Ordered State Comes of Age. *Biochim. Biophys. Acta.* **2010**, *1798*, 126–1288.

Murakami, Y.; Zhang, Z.; Taniguchi, T.; Shogawa, M.; Yamashita, K.; Noda, M. A High-Sensitive Detection of Several Tens of nM of Amyloid-β by Cantilever-type Biosensor Immobilized DPPC Liposome Incorporated with Cholesterol. *Proc. Eng.* **2016**, *168*, 565-568.

M'Baye, G.; Mély, Y.; Duportail, G.; Klymchenko, A. Liquid Ordered and Gel Phases of Lipid Bilayers: Fluorescent Probes Reveal Close Fluidity but Different Hydration. *Biophys. J.* **2008**, *95*.

Nikoleli, G.-P.; Ibupoto, Z.H.; Nikolelis, D.P.; Likodimos, V.; Psaroudakis, N.; Tzamtzis, N.; Willander, M.; Hianik, T. Potentiometric Cholesterol Biosensing Application of Graphene Electrode with Stabilized Polymeric Lipid Membrane. *Cent. Eur. J. Chem.* **2013**, *11*, 1554–1561.

Nyholm, T. K. M.; Lindroos, D.; Westerlund, B.; Slotte, J. P. Construction of a DOPC/PSM/Cholesterol Phase Diagram Based on the Fluorescence Properties of *trans* -Parinaric Acid. *Langmuir* **2011**, *27 (13)*, 8339–8350.

Nyholm, T.; Nylund, M.; Slotte, J. P. A Calorimetric Study of Binary Mixtures of Dihydrosphingomyelin and Sterols, Sphingomyelin, or Phosphatidylcholine. *Biophys. J.* **2003**, *84 (5)*, 3138–3146.

Nyholm, T.; Nylund, M.; Söderholm, A. S.; Slotte, J. P. Properties of Palmitoyl Phosphatidylcholine, Sphingomyelin, and Dihydrosphingomyelin Bilayer Membranes as Reported by Different Fluorescent Reporter Molecules. *Biophys. J.* **2003**, *84*, 987–997.

Olsson, T. S. G.; Ladbury, J. E.; Pitt, W. R.; Williams, M. A. Extent of Enthalpy–Entropy Compensation in Protein–Ligand Interactions. *Protein Sci.* **2011**, *20 (9)*, 1607–1618.

Onda, M.; Yoshihara, K.; Koyano, H.; Ariga, K.; Kunitake, T. Molecular Recognition of Nucleotides by the Guanidinium Unit at the Surface of Aqueous Micelles and Bilayers. A

Comparison of Microscopic and Macroscopic Interfaces. *J. Am. Chem. Soc.* **1996**, *118 (36)*, 8524–8530.

Paleos, C. M.; Kardassi, D.; Tsiourvas, D. Transformation of Dihexadecyl Phosphate Vesicles to Micelles Using Guanidinium-Type Counterions. *Langmuir* **1999**, *15*, 282–284.

Pantos, A.; Tsogas, I.; Paleos, C. M. Guanidinium Group: A Versatile Moiety Inducing Transport and Multicompartmentalization in Complementary Membranes. *Biochim. Biophys. Acta* **2008**, *1778*, 811–823.

Parasassi, T.; Conti, F.; Graton, E. Time-Resolved fluorescence Emission Spectra of Laurdan in Phospholipid Vesicles by Multifrequency Phase and Modulation Fluorometry. *Cell. Mol. Biol.* **1986**, *32 (1)*, 103–108.

Parasassi, T.; De Stasio, G.; Ravagnan, G.; Rusch, R. M.; Gratton, E. Quantitation of Lipid Phases in Phospholipid Vesicles by the Generalized Polarization of Laurdan Fluorescence. *Biophys. J.* **1991**, *60 (1)*, 179–189.

Parasassi, T.; De Stasio, G.; d'Ubaldo, A.; Gratton, E. Phase Fluctuation in Phospholipid Membranes Revealed by Laurdan Fluorescence. *Biophys. J.* **1990**, *57 (6)*, 1179–1186.

Parasassi, T.; Gratton, E. Packing of Phospholipid Vesicles Studied by Oxygen Quenching of Laurdan Fluorescence. *J. Fluoresc.* **1992**, *2 (3)*, 167–174.

Parasassi, T.; Gratton, E.; Yu, W. M.; Wilson, P.; Levi, M. Two-Photon Fluorescence Microscopy of Laurdan Generalized Polarization Domains in Model and Natural Membranes. *Biophys. J.* **1997**, *72*, 2413–2429.

Parasassi, T.; Krasnowska, E. K.; Bagatolli, L.; Gratton, E. Laurdan and Prodan as Polarity-Sensitive Fluorescent Membrane Probes. *J. Fluoresc.* **1998**, *8 (4)*, 365–373.

Parasassi, T.; Loiero, M.; Raimondi, M.; Ravagnan, G.; Gratton, E. Absence of Lipid Gel-Phase Domains in Seven Mammalian Cell Lines and in Four Primary Cell Types. *Biochim. Biophys. Acta* **1993**, *1153 (2)*, 143–154.

Parasassi, T.; Ravagnan, G.; Rusch, R. M.; Gratton, E. Modulation and Dynamics of Phase Properties in Phospholipid Mixtures Detected by Laurdan Fluorescence. *Photochem. Photobiol.* **1993**, *57 (3)*, 403–410.

Pasenkiewicz-Gierula, M.; Baczynski, K.; Markiewicz, M.; Murzyn, K. Computer Modelling Studies of the Bilayer/Water Interface. *Biochim. Biophys. Acta* **2016**, *1858 (10)*, 2305–2321.

Patil, S. D.; Rhodes, D. G.; Burgess, D. J. DNA-Based Therapeutics and DNA Delivery Systems: A Comprehensive Review. *Aaps J.* **2005**, *7*, E61-77.

Peetla, C.; Stine, A.; Labhasetwar, V. Biophysical Interactions with Model Lipid Membranes: Applications in Drug Discovery and Drug Delivery. *Mol. Pharm.* **2009**, *6*, 1264–1276.

Petruzielo, R. S.; Heberle, F. A.; Drazba, P.; Katsaras, J.; Feigensin, G. W. Phase Behavior and Domain Size in Sphingomyelin-Containing Lipid Bilayers. *Biochim. Biophys. Acta, Biomembr.* **2013**, *1828* (4), 1302–1313.

Pierrat, P.; Lebeau, L. Characterization of Titratable Amphiphiles in Lipid Membranes by Fluorescence Spectroscopy. *Langmuir* **2015**, *31*, 12362–12371.

Pozharski, E.; MacDonald, R. C. Lipoplex Thermodynamics: Determination of DNA-Cationic Lipoid Interaction Energies. *Biophys. J.* **2003**, *85 (6)*, 3969–3978.

Purves, D.; Augustine, G. J.; Fitzpatrick, D.; Katz, L. C.; LaMantia, A.; McNamara, J. O.; Williams, S. M. eds. Chapter 4: Channels and Transporters". *Neuroscience* (2nd ed.).; Sinauer Associates Inc. Sunderland, **2001**.

Ramstedt, B.; Slotte, J. P. Interaction of Cholesterol with Sphingomyelins and Acyl-Chain-Matched Phosphatidylcholines: A Comparative Study of the Effect of the Chain Length. *Biophys. J.* **1999**, *76 (2)*, 908–915.

Ramstedt, B.; Slotte, J. P. Membrane Properties of Sphingomyelins. *FEBS Lett.* **2002** 531 (1), 33–37.

Rekharsky, M. V.; Mori, T.; Yang, C.; Ko, Y. H.; Selvapalam, N.; Kim, H.; Sobransingh, D.; Kaifer, A. E.; Liu, S.; Isaacs, L.; et al. A Synthetic Host-Guest System Achieves Avidin-Biotin Affinity by Overcoming Enthalpy–Entropy Compensation. *PNAS* **2007**, *104 (52)*, 20737–20742.

Rifici, S.; Corsaro, C.; Crupi, C.; Nibali, V. C.; Branca, C.; D'Angelo, G.; Wanderlingh, U. Lipid Diffusion in Alcoholic Environment. *J. Phys. Chem. B* **2014**, *118 (31)*, 9349–9355.

Rouser, G.; Fleischer, S.; Yamamoto, A. Two Dimensional Thin Layer Chromatographic Separation of Polar Lipids and Determination of Phospholipids by Phosphorus Analysis of Spots. *Lipids* **1970**, *5 (5)*, 494–496.

Rowe, B. A.; Roach, C. A.; Lin, J.; Asiago, V.; Dmitrenko, O.; Neal, S. L. Spectral Heterogeneity of PRODAN Fluorescence in Isotropic Solvents Revealed by Multivariate Photokinetic Analysis. *J. Phys. Chem. A* **2008**, *112 (51)*, 13402–13412.

Saha, R.; Verbanic, S.; Chen, I. A. Lipid Vesicles Chaperone an Encapsulated RNA Aptamer. *Nature Comm.* **2018**, *9 (1)*.

Saito, H.; Shinoda, W. Cholesterol Effect on Water Permeability through DPPC and PSM Lipid Bilayers: A Molecular Dynamics Study. *J. Phys. Chem. B* **2011**, *115 (51)*, 15241–15250.

Sakurai, M.; Hoshi, H.; Inoue, Y.; Chujo, R. A Method for Estimating Medium Effects in Heterogeneous Systems. Theoretical Analysis of Complexation-Induced ^{13}C-NMR Chemical Shift Changes in α-Cyclodextrin-Guest Systems. *Chem. Phys. Lett.* **1989**, *163*, 217–220.

Sakurai, M.; Tamagawa, H.; Inoue, Y.; Ariga, K.; Kunitake, T. Theoretical Study of Intermolecular Interaction at the Lipid−Water Interface. 1. Quantum Chemical Analysis Using a Reaction Field Theory. *J. Phys. Chem. B* **1997**, *101 (24)*, 4810–4816.

Sanchez, S. A.; Tricerri, M. A.; Gratton, E. Laurdan Generalized Polarization Fluctuations Measures Membrane Packing Micro-Heterogeneity in Vivo. *PNAS* **2012**, *109 (19)*, 7314–7319.

Sasaki, D. Y.; Kurihara, K.; Kunitake, T. Self-Assembled Multifunctional Receptors for Nucleotides at the Air-Water Interface. *J. Am. Chem. Soc.* **1992**, *114 (27)*, 10994–10995.

Schrader, T.; Gal, B.; Klärner, F. G. Molecular Tweezers for Lysine and Arginine – Powerful Inhibitors of Pathologic Protein Aggregation. *Chem. Comm.* **2016**, *52*, 11318-11334.

Sehgal, K. C.; Pickard, W. F.; Jackson, C. M. Phospholipid Monolayers at the Hydrocarbon-Electrolyte Interface. The Interrelation of Film Potential and Film Pressure. *Biochim. Biophys. Acta* **1979**, *552*, 11–22.

Seu, K. J.; Cambrea, L. R.; Everly, R. M.; Hovis, J. S. Influence of Lipid Chemistry on Membrane Fluidity: Tail and Headgroup Interactions. *Biophys. J.* **2006**, *91*, 3727–3735.

Shimizu, Y.; Inoue, A.; Tomari, Y.; Suzuki, T.; Yokogawa, T.; Nishikawa, K.; Ueda, T. Cell-free Translation Reconstituted with Purified Components. *Nat. Biotechnol.* **2001**, *19 (8)*, 751-755.

Shrestha, B. R.; Banquya, X. Hydration Forces at Solid and Fluid Biointerfaces. *Biointerphases* **2016**, *11(1)*, 018907.

Simons, K.; Gerl, M. J. Revitalizing Membrane Rafts: New Tools and Insights. *Nat. Rev. Mol. Cell Biol.* **2010**, *11 (10)*, 688–699.

Simons, K.; Ikonen, E. Functional Rafts in Cell Membranes. *Nature* **1997**, *387 (6633)*, 569–572.

Singare, P. U.; Mhatre, J. D. Cationic Surfactants from Arginine: Synthesis and Physicochemical Properties. *Am. J. Chem.* **2012**, *2*, 186–190.

Siontorou, C. G.; Nikoleli, G. P.; Nikolelis, D. P.; Karaoetis, S. K. Artificial Lipid Membranes: Past, Present, and Future. *Membranes* **2017**, *7 (3)*.

Slotte, J. P. The Importance of Hydrogen Bonding in Sphingomyelin's Membrane Interactions with Co-Lipids. *Biochim. Biophys. Acta* **2016**, *1858 (2)*, 304–310.

Sparr, E.; Wennerström, H. Responding Phospholipid Membranes—Interplay between Hydration and Permeability. *Biophys. J.* **2001**, *81 (2)*, 1014–1028.

Spink, C. H.; Chaires, J. B. Thermodynamics of the Binding of a Cationic Lipid to DNA. *J. Am. Chem. Soc.* **1997**, *119*, 10920-10928.

Stephanos, J. J.; Farina, S. A.; Addison, A. W. Iron Ligand Recognition by Monomeric Hemoglobins. *Biochim. Biophys. Acta* **1996**, *1295*, 209–221.

Subramanian, M.; Holopainen, J. M.; Paukku, T.; Eriksson, O.; Huhtaniemi, I.; Kinnunen, P. K. Characterisation of Three Novel Cationic Lipids as Liposomal Complexes with DNA. *Biochim. Biophys. Acta* **2000**, *1466*, 289–305.

Suga, K.; Akizaki, K.; Umakoshi, H. Quantitative Monitoring of Microphase Separation Behaviors in Cationic Liposomes Using HHC, DPH, and Laurdan: Estimation of the Local Electrostatic Potentials in Microdomains. *Langmuir* **2016**, *32 (15)*, 3630–3636.

Suga, K.; Otsuka, Y.; Okamoto, Y.; Umakoshi, H. Gel-Phase-like Ordered Membrane Properties Observed in Dispersed Oleic Acid/1-Oleoylglycerol Self-Assemblies: Systematic Characterization Using Raman Spectroscopy and a Laurdan Fluorescent Probe. *Langmuir* **2018**, *34 (5)*, 2081–2088.

Suga, K.; Tanabe, T.; Tomita, H.; Shimanouchi, T.; Umakoshi, H. Conformational Change of Single-Stranded RNAs Induced by Liposome Binding. *Nucleic Acids Res* **2011**, *39 (20)*, 8891–8900.

Suga, K.; Tanabe, T.; Umakoshi, H. Heterogeneous Cationic Liposomes Modified with 3β-{N-[(N',N'-Dimethylamino)Ethyl]Carbamoyl}cholesterol Can Induce Partial Conformational Changes in Messenger RNA and Regulate Translation in an Escherichia Coli Cell-Free Translation System. *Langmuir* **2013**, *29 (6)*, 1899–1907.

Suga, K.; Tanaka, S.; Umakoshi, H. Liposome Membrane Can Induce Self-Cleavage of RNA That Models the Core Fragments of Hammerhead Ribozyme. *Eur. Biophys. J.* **2016**, *45*, 55–62.

Suga, K.; Tomita, H.; Tanaka, S.; Umakoshi, H. Hydrophobic Properties of tRNA with Varied Conformations Evaluated by an Aqueous Two-Phase System. *Int. J. Biopl. Sci.* **2012**, *8 (8)*, 1188–1196.

Suga, K.; Umakoshi, H. Detection of Nanosized Ordered Domains in DOPC/DPPC and DOPC/Ch Binary Lipid Mixture Systems of Large Unilamellar Vesicles Using a TEMPO Quenching Method. *Langmuir* **2013**, *29 (15)*, 4830–4838.

Suga, K.; Umakoshi, H.; Tomita, H.; Tanabe, T.; Shimanouchi, T.; Kuboi, R. Liposomes Destabilize tRNA During Heat Stress. *Biotechnol. J.* **2010**, *5*, 526–529.

Suga, K.; Yokoi, T.; Kondo, D.; Hayashi, K.; Morita, S.; Okamoto, Y.; Shimanouchi, T.; Umakoshi, H. Systematical Characterization of Phase Behaviors and Membrane Properties of Fatty Acid/ Didecyldimethylammonium Bromide Vesicles. *Langmuir* **2014**, *30*, 12721–12728.

Suga, K.; Yoshida, T.; Ishii, H.; Okamoto, Y.; Nagao, D.; Kondo, M.; Umakoshi, H. Surface-Enhanced Raman Spectroscopy for Sensitive Detection of Molecular Behavior of Lipid Assemblies. *Anal. Chem.* **2015**, *87*, 4772–4780.

Suleymanoglu, E. Divalent Cation Induced DNA-zwitterionic Vesicle Formulation Compacted for Gene Delivery: Thermodynamic Aspects. *Pak J Pharm Sci.* **2004**, *17*,129–133.

Talbott, C. M.; Vorobyov, I.; Borchman, D.; Taylor, K. G.; DuPré, D. B.; Yappert, M. C. Conformational Studies of Sphingolipids by NMR Spectroscopy. II. Sphingomyelin. *Biochim. Biophys. Acta* **2000**, *1467 (2)*, 326–337.

Templeton, N. S. Gene and Cell Therapy: Therapeutic Mechanisms and Strategies, Third Edition; *CRC Press*, **2008**.

Thomas, C. F.; Luisi, P. L. RNA Selectively Interacts with Vesicles Depending on Their Size. *J. Phys. Chem. B* **2005**, *109*, 14544–14550.

Tieleman, D. P.; Marrink, S. J.; Berendsen, H. J. C. A Computer Perspective of Membranes: Molecular Dynamics Studies of Lipid Bilayer Systems. *Biochim. Biophys. Acta* **1997**, *1331 (3)*, 235–270.

Tristram-Nagle, S.; Petrache, H. I.; Nagle, J. F. Structure and Interactions of Fully Hydrated Dioleoylphosphatidylcholine Bilayers. *Biophys. J.* **1998**, *75 (2)*, 917–925.

Troutier, A. L.; Véron, L.; Delair, T.; Pichot, C.; Ladaviére, C. New Insights into Self-Organization of a Model Lipid Mixture and Quantification of Its Adsorption on Spherical Polymer Particles. *Langmuir* **2005**, *21*, 9901–9910.

Tsuji, A.; Yoshikawa, K. Real-Time Monitoring of RNA Synthesis in a Phospholipid-Coated Microdroplet as a Live-Cell Model. *Chem. Bio. Chem.* **2010**, *11*, 351–357.

Török, Z.; Crul, T.; Maresca, B.; Schütz, G.J.; Viana, F.; Dindia, L.; Piotto, S.; Brameshuber, M.; Balogh, G.; Péter, M.; et al. Plasma Membranes as Heat Stress Sensors: From Lipid-controlled Molecular Switches to Therapeutic Applications. *Biochim. Biophys. Acta* **2014**, *1838*, 1594–1618.

Ulrich, A. S.; Sami, M.; Watts, A. Hydration of DOPC Bilayers by Differential Scanning Calorimetry. *Biochim. Biophys. Acta* **1994**, *1191 (1)*, 225–230.

Umakoshi, H.; Morimoto, K.; Ohama, Y.; Nagami, H.; Shimanouchi, T.; Kuboi, R. Liposome Modified with Mn-Porphyrin Complex Can Simultaneously Induce Antioxidative Enzymes-like Activity of Both Superoxide Dismutase and Peroxidase. *Langmuir* **2008**, *24*, 4451–4455.

Umeyama, H.; Morokuma, K.; The Origin of Hydrogen Bonding. An Energy Decomposition Study. *J. Am. Chem. Soc.* **1977**, *99 (5)*, 1316-1332.

Urbach, A. R.; Ramalingam, V. Molecular Recognition of Amino Acids, Peptides, and Proteins by Cucurbit[n]uril Receptors. *Isr. J. Chem.* **2011**, *51*, 664-678.

Valeur, B. *Molecular Fluorescence: Principles and Applications.*; Wiley-VCH Verlag GmbH: Weinheim, **2001**.

Veatch, S. L.; Keller, S. L. Miscibility Phase Diagrams of Giant Vesicles Containing Sphingomyelin. *Phys. Rev. Lett.* **2005**, *94 (14)*, 148108.

Venable, R. M.; Sodt, A. J.; Rogaski, B.; Rui, H.; Hatcher, E.; MacKerell Jr., A. D.; Pastor, R. W.; Klauda, J. B. CHARMM All-Atom Additive Force Field for Sphingomyelin: Elucidation of Hydrogen Bonding and of Positive Curvature. *Biophys. J.* **2014**, *107*, 134–145.

Viard, M.; Gallay, J.; Vincent, M.; Meyer, O.; Robert, B.; Paternostre, M. Laurdan Solvatochromism: Solvent Dielectric Relaxation and Intramolecular Excited-State Reaction. *Biophys. J.* **1997**, *73 (4)*, 2221–2234.

Villar, V. A. M.; Cuevas, S.; Zheng, X.; Jose, P. A. Localization and Signaling of GPCRs in Lipid Rafts. In Methods in Cell Biology; *Elsevier*, **2016**; *Vol. 132*, pp 3–23.

Vogel, V.; Möbius, D. Hydrated Polar Groups in Lipid Monolayers: Effective Local Dipole Moments and Dielectric Properties. *Thin Solid Films* **1988**, *159*, 73.

Vogel, V.; Möbius, D. Local Surface Potentials and Electric Dipole Moments of Lipid Monolayers: Contributions of the Water/Lipid and the Lipid/Air Interfaces. *J. Colloid Interface Sci.* **1988**, *126*, 408–420.

Volke, F.; Eisenblätter, S.; Galle, J.; Klose, G. Dynamic Properties of Water at Phosphatidylcholine Lipid-Bilayer Surfaces as Seen by Deuterium and Pulsed Field Gradient Proton NMR. *Chem. Phys. Lipids* **1994**, *70 (2)*, 121–131.

Wagner, E. Strategies to Improve DNA Polyplexes for in Vivo Gene Transfer: Will "Artificial Viruses" Be the Answer? *Pharm. Res.* **2004**, *21*, 8–14.

Walde, P. Phospholipid Membranes as Regulators of Localized Activity. *Chem. Biol.* **2010**, *17*, 922–923.

Walde, P.; Umakoshi, H.; Stano, P.; Mavelli, F. Emergent Properties Arising from the Assembly of Amphiphiles. Artificial Vesicle Membranes as Reaction Promoters and Regulators. *Chem. Comm.* **2014**, *50*, 10177–10197.

Wang, D. S.; Shaw, G. The Association of the C-Terminal Region of β1ΣII Spectrin to Brain Membranes Is Mediated by a pH Domain, Does Not Require Membrane Proteins, and Coincides with a Inositol-1,4,5 Triphosphate Binding Site. *Biochem. Biophys. Res. Commun.* **1995**, *217*, 608-615.

Weast, R. C. *CRC Handbook of Chemistry and Physics, 64th Ed.*; CRC Press Florida, **1983**; *169*.

Wiseman, T.; Williston, S.; Brandts, J. F.; Lin, L. N. Rapid Measurement of Binding Constants and Heats of Binding Using a New Titration Calorimeter. *Anal. Biochem.* **1989**, *179*, 131-137.

Yang, S.-T.; Kiessling, V.; Tamm, L. K. Line Tension at Lipid Phase Boundaries as Driving Force for HIV Fusion Peptide-Mediated Fusion. *Nature Commun.* **2016**, *7*, 11401.

Yarus, M. A Specific Amino Acid Binding Site Composed of RNA. *Science* **1988**, *240*, 1751–1758.

Yasuda, T.; Al Sazzad, M. A.; Jäntti, N. Z.; Pentikäinen, O. T.; Slotte, J. P. The Influence of Hydrogen Bonding on Sphingomyelin/Colipid Interactions in Bilayer Membranes. *Biophys. J.* **2016**, *110 (2)*, 431–440.

Yeagle, P. L. *The membranes of Cells*, Academic Press, New York, **2016**.

Yoshimoto, M.; Kozono, R.; Tsubomura, N. Liposomes as Chaperone Mimics with Controllable Affinity toward Heat-Denatured Formate Dehydrogenase from Candida Boidinii. *Langmuir* **2015**, *31*, 762–770.

Yoshimoto, M.; Miyazaki, Y.; Umemoto, A.; Walde, P.; Kuboi, R.; Nakao, K. Phosphatidylcholine Vesicle-Mediated Decomposition of Hydrogen Peroxide. *Langmuir* **2007**, *23*, 9416–9942.

Zwang, T. J.; Fletcher, W. R.; Lane, T. J.; Johal, M. S. Quantification of the Layer of Hydration of a Supported Lipid Bilayer. *Langmuir* **2010**, *26 (7)*, 4598–4601.

van Dun, S.; Ottmann, C.; Milroy, L. G.; Brunsveld, L. Supramolecular Chemistry Targeting Proteins. *J. Am. Chem. Soc.* **2017**, *139*, 13960-13968.

List of Publications

[Papers]

1. Keishi Suga, Nozomi Watanabe, Hiroshi Umakoshi, Effect of Stearylguanidinium-Modified POPC Vesicles on the Melting Behavior of tRNA Molecules. *J. Phys. Chem. B*, **2016**, *120*, 5662−5669.

2. Nozomi Watanabe, Keishi Suga, Hiroshi Umakoshi, Comparison of Physicochemical Membrane Properties of Vesicles Modified with Guanidinium Derivatives. *J. Phys. Chem. B*, **2017**, *121 (39)*, 9213–9222.

3. Nozomi Watanabe, Keishi Suga, Hiroshi Umakoshi, Functional Hydration Behavior: Interrelation Between Hydration and Molecular Properties at Lipid Membrane. *J. Chemistry*, **2019**, article ID 4867327 (15 pages).

4. Nozomi Watanabe, Yuka Goto, Keishi Suga, Thomas K. M. Nyholm, J. Peter Slotte, Hiroshi Umakoshi, Solvatochromic Modeling of Laurdan for Multiple Polarity Analysis of the Dihydro-sphingomyelin Bilayer. *Biophys. J.*, **2019**, *116*, 1-10.

[Related Papers]

1. Nozomi Watanabe, Keishi Suga, J. Peter Slotte, Thomas K. M. Nyholm, Hiroshi Umakoshi, Lipid-Surrounding Water Molecules Probed by Time-Resolved Emission Spectra of Laurdan. *Langmuir, submitted.*

2. Nozomi Watanabe, Keishi Suga, J. Peter Slotte, Thomas K. M. Nyholm, Hiroshi Umakoshi, Heterogenic Hydration Behavior on Raft Domain Probed by Time-Resolved Emission Spectra of Laurdan. *Langmuir, in preparation*.

3. Nozomi Watanabe, Ryosuke Ueno, Keishi Suga, Hiroshi Umakoshi, Characterization of Interaction of Nucleotides with Lipid Membrane by Using Isothermal Titration Calorimeteric Analysis, *J. Phys. Chem. B, in preparation.*

[International Conference / Symposium]

1. Nozomi Watanabe, Keishi Suga, Yukihiro Okamoto, Hiroshi Umakoshi, Effect of Stearylguanidinium-Modified POPC Vesicles on the Melting Behavior of tRNA Molecules. RNA2016, Kyoto, Japan, July (2016).

2. Nozomi Watanabe, Keishi Suga, Yukihiro Okamoto, Hiroshi Umakoshi, Effect of Stearylguanidinium-Modified POPC Vesicles on the Melting Behavior of tRNA Molecules. The 10th Conference of Aseanian Membrane Society (AMS10), Nara, Japan, July (2016).

3. Nozomi Watanabe, Keishi Suga, Yukihiro Okamoto, Hiroshi Umakoshi, Design and Characterization of Liposome Membrane as Platform for RNA Recognition. 11th International Conference on Separation Science and Technology (ICSST17), Busan, Korea, November (2017).

4. Nozomi Watanabe, Thomas K.M. Nyholm, J. Peter Slotte, Keishi Suga, Hiroshi Umakoshi, Solvatochromic Property in Lipid Bilayer Interphases Evaluated from the Deconvolution of Time Resolved Emission Spectrum of Laurdan. 62nd Annual Meeting of Biophysical Society, San Francisco, USA, February (2018).

5. Nozomi Watanabe, Keishi Suga, Thomas K. M. Nyholm, J. Peter Slotte, Hiroshi Umakoshi, Solvatochromic Property in Lipid Bilayer Interphases Analyzed Based on Time-Resolved Emission Spectrum of Laurdan. 2018 AIChE Annual Meeting, Pittsburgh, USA, November (2018).

[Article / Review]

1. Nozomi Watanabe, Evaluation of the Interfacial Property of Cationic-Ligand Modified Lipid Membrane and its Application for the Adsorption of Nucleic Acid (in Japanese), *Bunri Gijutsu*, **2016**, *46*, 44-45.

Acknowledgements

The author is deeply grateful to Prof. Dr. Hiroshi Umakoshi (Division of Chemical Engineering, Graduate School of Engineering Science, Osaka University), for his insightful comments, suggestions, and warm encouragement throughout this work. The author is thankful to Prof. Dr. Masahiro Taya, Prof. Dr. Nobuyuki Matsubayashi, Prof. Dr. Norikazu Nishiyama (Division of Chemical Engineering, Graduate School of Engineering Science, Osaka University) for a number of valuable comments and suggestions during the completion of this thesis. The author would like to express my gratitude to Assist. Prof. Dr. Keishi Suga (Division of Chemical Engineering, Graduate School of Engineering Science, Osaka University) for his enormous encouragements on my research. The author also would like to express the greatest appreciation to Assoc. Prof. Dr. Yukihiro Okamoto (Division of Chemical Engineering, Graduate School of Engineering Science, Osaka University) for his valuable comments and helpful advises. The author would like to offer one's special thanks to Ms. Keiko Fukumoto for her kind support during this work.

The author would like to show her greatest appreciation to Prof. Dr. R. Kuboi, Prof. Dr. K. Ohgaki, (Honored Professor of Osaka University). The author is thankful to Prof. Dr. K. Jitsukawa, Prof. Dr. Y. Okano, Prof. Dr. M. Nakano, Prof. Dr. T. Hirai, Prof. Dr. S. Sakai, and all the staff of Division of Chemical Engineering, Graduate School of Engineering Science, Osaka University for their kind cooperation during my research.

The author expresses her sincere appreciations to Prof. Dr. J. P. Slotte and Dr. T. K. M. Nyholm (Faculty of Science and Engineering, Åbo Akademi University, Finland) for enormous supports in the collaborative works. The author wishes to thank Prof. Dr. P. Walde (Institute for Polymer, ETH, Zurich), Prof. Dr. B. Higgins (Department of Chemical Engineering and Materials Science, University of California, Davis), Prof. Dr. P. Alexandridis (Department of Chemical Engineering, University at Buffalo), Prof. Dr. Ho-Sup Jung (Department of Mechanical and Aerospace Engineering, Seoul National University), Prof. Dr. M. Murata (Graduate School of Sciences, University of Osaka), Prof. Dr. K. Shiomori (Department of Applied Chemistry, University of Miyazaki), Prof. Dr. H. Nakamura (Department of Chemical Engineering, National Institute of Technology, Nara College), Prof. Dr. D. Nagao (Department of Applied Chemistry, Tohoku University), and Prof. Dr. M. Konno (Department of Applied Chemistry, Tohoku University) for their comments and suggestions during this work. The author is grateful for the advice given by Assoc. Prof. Dr. H. Ishii (Graduate school of Sciences and Technology for Innovation, Yamaguchi University), Assoc. Prof. Dr. T. Shimanouchi (Graduate School of Environmental and Life Science, Okayama University), Assoc. Prof. Dr. K. Hayashi (National Institute of Technology), Dr. Y. Todokoro (Graduate School of Science, Osaka University), Dr. H. Sugaya (Toray Industries, inc.), and Dr. Y. Yamada (Kao corporation).

The author is particularly grateful for the assistance given by Y. Goto and R. Ueno. Special thanks are given to following colleagues for their experimental collaboration: T. Ishigami, K. Sugita, J. Chinzaka, T. Hinoyama, F. Iwasaki, Y. Kaneko, M. Kiriishi, D. Kondo, Y. Takaya, M. Hirose, M. Kota, K. Goshima, S. Taguchi, Y. Tsujimoto, A. Hamasaki, T. Yoshida, B. T. Tham, K. Akizaki, T. Ikeda,Y. Kishi, Y. Higashie, R. Matsuba, Y. Mine, Y. Otsuka, Y. Shinozuka, S. Sugisaki, A. Tauchi, D. Wada, J. Han, K. Midogochi, R. Ito, Y. Ooe, R. Kawakami, R. Kawakami, R. Nishino, K. Yoshida, T. Wakita, K. Tanimura, Y. Iimure, K. Kitagawa, Y. Murata, M. Faried, M. Amau, N. Ikushima, K. Kojima, Y. Seno, Y. Hasunuma, D. Matsui, S. Matsushita, R. Murazawa, M. S. Chern, C. Lishi, C. Tran, A. Ajaikumar, R. Wakerlin, Y.-C. Lai, H. J. Kim, D. Etwaru, B. S. Kan and all the member in Bio-Inspired Chemical Engineering Laboratory. The author also would like to show appreciation to M. Lönnfors, J. Isaksson, H. Cooper, M. A. Al Sazzad, O. Engberg, A. Möuts, V. Hautala, H. Nurmi and all the members in the laboratory of lipid and membrane biochemistry, faculty of Science and Engineering, Åbo Akademi University for kind helps and warm acceptance as a member of the group during research stay.

The author would like to express deepest appreciation to her parents Hirobumi Watanabe and Fumiko Watanabe and her siblings Shiori Watanabe, Satomi Iida, and Robin Watanabe for their continuous encouragements and great support throughout this work.

The author gratefully acknowledges the financial support of this work by the fellowship of the Japan Society for the Promotion of Science (JSPS) and Tobitate! (Leap for Tomorrow) Young Ambassador Program.